2021-12-21

Temperature Relaxation and Magnetically Suppressed Expansion in Strongly Coupled Ultracold Neutral Plasmas

Robert Tucker Sprenkle
Brigham Young University

Temperature Relaxation and Magnetically Suppressed Expansion in Strongly Coupled Ultracold Neutral Plasmas

Robert Tucker Sprenkle

A dissertation submitted to the faculty of
Brigham Young University
in partial fulfillment of the requirements for the degree of

Doctor of Philosophy

Scott D. Bergeson, Chair
Michael Ware
Ross Spencer
Grant Hart
Steve Turley

Department of Physics and Astronomy

Brigham Young University

ABSTRACT

Temperature Relaxation and Magnetically Suppressed Expansion in Strongly Coupled Ultracold Neutral Plasmas

Robert Tucker Sprenkle
Department of Physics and Astronomy, BYU
Doctor of Philosophy

Ultracold neutral plasmas provide a platform for studying transport properties in an idealized environment. In this dissertation, transport properties in a Ca^+/Yb^+ dual species ultracold neutral plasma and a Ca^+ magnetized ultracold neutral plasma are studied. In dual species plasmas, we study ion-ion temperature relaxation. We compare measured relaxation rates with atomistic simulations and a range of popular theories. Our work validates the assumptions and capabilities of molecular dynamic simulations and invalidates theoretical models in this regime. This work illustrates an approach for precision determinations of detailed material properties in Coulomb mixtures across a wide range of conditions. We also study plasma expansion in single species plasma in the presence of a strong uniform magnetic field. We find that the asymptotic expansion velocity falls exponentially with magnetic field strength, which disagrees with a previously published ambipolar diffusion model. In the parallel direction, plasma expansion is driven by electron pressure. However, in the perpendicular direction, no plasma expansion is observed at large magnetic field strengths.

Keywords: energy transport, ultracold neutral plasma, magnetized plasma, strong coupling, energy relaxation, self-similar expansion, ambipolar diffusion

ACKNOWLEDGMENTS

Tiffani Sprenkle: I am deeply grateful to my wife for all of her support though my schooling. I thank her for her time, support and sacrifices that made it possible for me to accomplish my goals.

Parents: I am thankful to my parents, Rob and Shannon, for their continual support and teaching me to work hard and dream big.

Dr. Bergeson: I feel extremely blessed to have had Dr. Bergeson as my advisor. I am greatly appreciative of his time and his willingness to help me learn and grow as a physicist. I feel ready and prepared to be a successful contributor to industry and the scientific community.

Committee: I thank my committee, Dr. Bergeson, Dr. Ware, Dr. Spencer and Dr. Turley for their time and support in guiding me in this work.

BYU: I am blessed for the opportunity to attend such a great university. I cherish my education and hope to stand as an example of the standards and quality of the university. I am grateful to Brigham Young University for providing the space and support for Dr. Bergeson's Lab where I performed this work.

Funding agencies: I am grateful for the support of our funding agencies who made this project financially possible; U.S. Air Force Office of Scientific Research Grant No. FA9550-17-1-0302 and the National Science Foundation Grant No. PHY-2009999.

Contents

Table of Contents **iv**

List of Figures **vi**

1 Introduction **1**

2 Temperature Relaxation in Strongly Coupled Binary Ionic Mixtures **6**
2.1 Introduction 6
2.2 Results 9
2.2.1 Dual-Species Ultracold Neutral Plasma 9
2.2.2 Two-Temperature Plasmas 12
2.2.3 Molecular Dynamic Simulations 13
2.2.4 Theoretical Considerations 16
2.2.5 Comparison of Experiment, Simulation, and Theory 19
2.3 Discussion 24
2.4 Methods 25

3 Ultracold Neutral Plasma Expansion in a Strong Uniform Magnetic Field **34**
3.1 Introduction 34
3.2 Methods 38
3.3 Analysis 41
3.4 Ambipolar Diffusion Model 45
3.5 Self Similar Plasma Expansion Model 49
3.6 Discussion 51
3.7 Acknowledgments 52

4 Methods **53**
4.1 Introduction 53
4.2 Laser Induced Fluorescence 53
4.3 Magneto Optical Trap 57
4.4 Slower Beam and Atomic Beam 60
4.5 Absorption Imaging and Plasma Size 62

4.6 Photo-Ionization and Electron Temperature 65
4.7 Dark States 67
4.8 Zeeman Splitting 68
4.9 Probe Laser Characteristics 69
4.10 Imaging Optics 73
4.11 Probe Laser Intensity 75
4.12 Magnetic Field Coils 76
4.13 Switch Circuit for Turning on/off B-Field 80
4.14 General Data Analysis 83
4.15 Self Similar Expansion Model 86
4.16 Ambipolar Diffusion 90

5 Conclusion **92**

Appendix A Ambipolar Diffusion Code **94**

Bibliography **98**

List of Figures

1.1 Plasma classes compared in temperature and density 2

1.2 Comparison between HEDP and UNP 3

2.1 Expansion dynamics for a dual-species Ca^+/Yb^+ UNP 11

2.2 Temperature evolution of Ca^+/Yb^+ mixture from MD simulation 15

2.3 Time evolution of Hermite coefficients 16

2.4 Experimental data showing temperature relaxation 21

2.5 Temperature difference comparison of MD and three theoretical models 22

2.6 Energy level diagrams for Ca and Yb neutral atoms 26

2.7 Experimental timing diagram 27

2.8 Experimental details for fluorescence detection from Ca^+ and Yb^+ ions 29

3.1 Energy level diagrams for Ca and Ca^+, timing diagram 36

3.2 Magnetic field construction and techniques used for data collection 39

3.3 Data analysis with no magnetic field 42

3.4 Data analysis with $B = 0.0203$ T 43

3.5 Comparing self similar expansion to experimental data 46

3.6 Comparing models to experimental data 47

4.1 Allowed atomic transitions in Ca^+, driving $^2S_{1/2}$ to $^2P_{3/2}$ 54

4.2 Allowed atomic transitions in Ca^+, driving $^2S_{1/2}$ to $^2P_{1/2}$ 55
4.3 Energy level diagram for the relevant energy levels in Ca^+ 56
4.4 Magnetic field from anti-Helmholtz coils 58
4.5 MOT radiation pressure diagram 59
4.6 Laser cooling diagram 61
4.7 Measuring absorption in a neutral atom cloud 63
4.8 Finding the angle of incidence of laser light with the ions 71
4.9 Ray trace diagram for a 1:1 telescope 73
4.10 CAD drawing of the assembled coils, coil housing and optical system 78
4.11 CAD drawing of the mounted coils and coil housing. 79
4.12 Theoretical magnetic field strength along the z axis 80
4.13 Magnetic field shut off circuit 81
4.14 Magnetic field shut off circuit timing 83
4.15 Plasma fluorescence at different laser detunings 84
4.16 Fitting a Voigt profile to experimental data 85

Chapter 1

Introduction

Ultracold neutral plasmas (UNPs) are useful tools in understanding transport properties of strongly coupled systems in an ideal environment. It has been shown that UNPs and high energy-density plasma (HEDP) share dynamic properties [1] when the one component Yukawa potential [2, 3] is appropriate. Accurately modeling HEDPs requires detailed and reliable models of collective phenomena such as continuum depression heating [4], turbulence and mixing [5–7], diffusion [8, 9], viscosity [10], thermal decoupling [11] and many other physical processes [1, 12]. In this work, we study ion-ion thermal relaxation of a Ca^+/Yb^+ dual-species UNP and expansion of a magnetized Ca^+ UNP.

Plasmas can be characterized using two dimensionless parameters. The first is the ratio of the nearest-neighbor electric potential energy to the average kinetic energy of the plasma. This is called the coupling parameter,

$$\Gamma = \frac{e^2}{4\pi\varepsilon_0 a_{ws}} \frac{1}{k_B T_i}, \tag{1.1}$$

where $a_{ws} = (3/4\pi n)^{1/3}$ is the Wigner-Seitz radius, n is the density of the plasma, k_B is Boltzmann's constant, ε_0 is the vacuum permittivity constant and T_i is the ion temperature of the plasma. For the

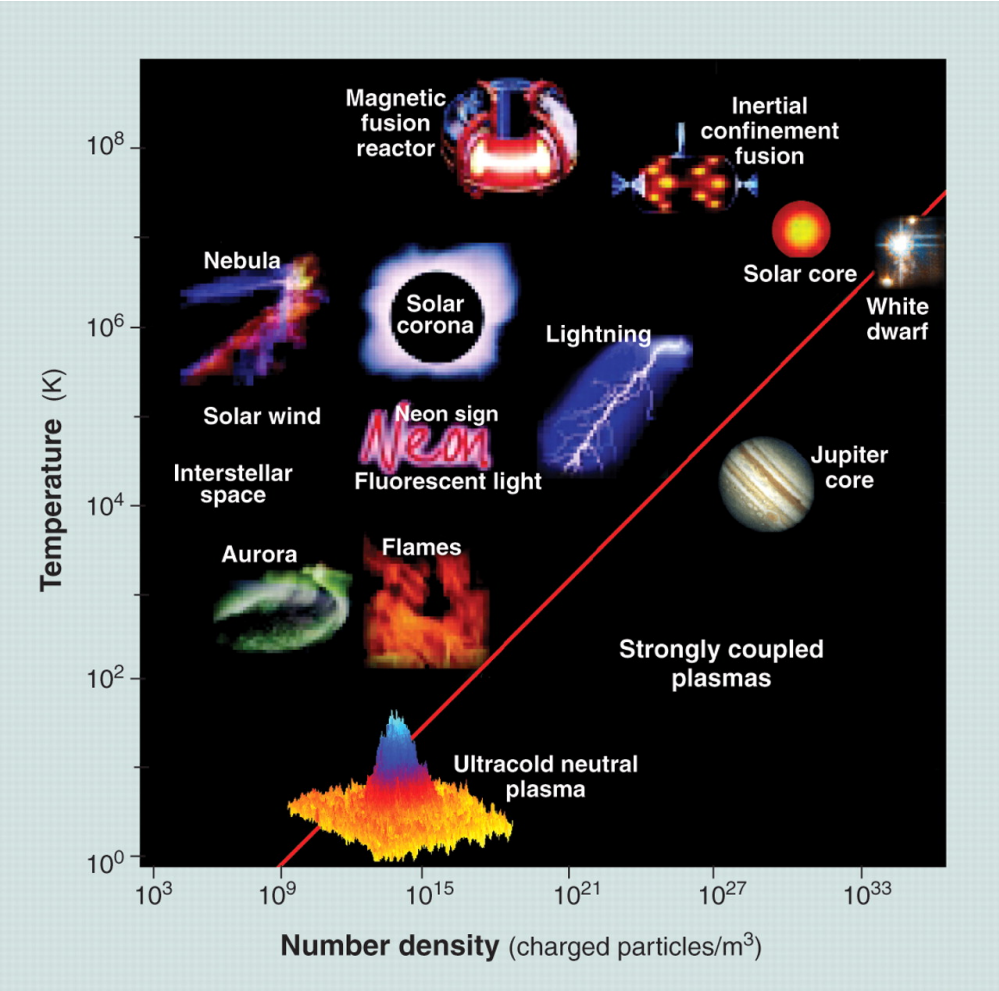

Figure 1.1 This figure shows the many plasmas that exist and how they compare in density and temperature to other plasma. The red line indicates when the coupling parameter $\Gamma = 1$. [Figure credit to Contemporary Physics Education Project - www.CPEPphysics.org]

experiments discussed in this dissertation $\Gamma \approx 2$. The red line in Fig. 1.1 [13] shows the dividing line for strongly and weakly coupled plasmas, where $\Gamma = 1$.

The second dimensionless parameter is the inverse scaled screening length, κ,

$$\kappa = \frac{a_{ws}}{\lambda_D}. \tag{1.2}$$

From this equation we find that $\kappa \propto n^{1/6}/T_e^{1/2}$. Larger values of κ correspond to larger screening strengths, effectively reducing the influence of nearest neighbor collisions.

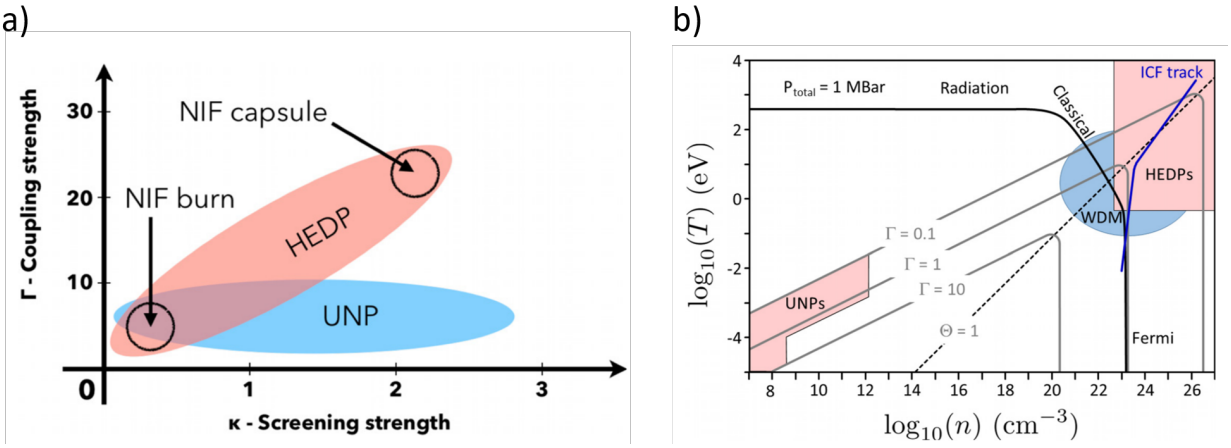

Figure 1.2 a) Shows the overlap between HEDPs and UNPs in coupling strength and screening strength parameter space. b) Demonstrates the temperature and density scaling of between HEDPs and UNPs at similar coupling strength. [Figure from [1] under creative commons license attribution 4.0 international (CC BY 4.0). No changes to the figures have been made]

The inverse scaled screening length, κ and the coupling parameter, Γ, are used to characterize collective phenomena that occur in plasma's. HEDPs and UNPs exist under vastly different temperature and density conditions. Typical densities for HEDPs exist at densities in excess of 10^{23} cm^{-3} and temperature on the order of 10^4 K. UNPs exist in the opposite extreme where densities are typically 10^9 cm^{-3} with temperatures around 1 K. These two seemingly different types of plasmas both overlap in a Γ and κ parameter space, as seen in Fig. 1.2. When both overlap in the same Γ-κ space, the underlying dynamics that drive transport are modeled using the same one-component Yukawa Potential [1].

The high optical opacity and short dynamic time scales in HEDPs pose challenges to experimentally measuring transport properties with high fidelity. For this reason, HEDP heavily rely on molecular dynamics (MD) simulations [14] and plasma models [15, 16] to understand transport in these complex systems. UNPs have the advantage of being 12 orders of magnitude below solid density with a temperature on the order of a Kelvin, resulting in accessible real-time plasma dynamic

measurements [1]. Transport properties in this environment are measured directly and can be used to verify current models and MD simulations [17–19].

In an ideal environment, where no external fields or forces exist, we have measured energy relaxation in a dual species UNP [17] as seen in Chapter 2. Transport properties are sensitive to external electric and magnetic fields, UNP provide an advantage for precise control over the electric and magnetic fields present in the plasma. In HEDP, large current densities are formed due to very high plasma densities. These current densities create strong internal magnetic fields that can significantly change transport properties. These large intrinsic magnetic fields make it difficult to measuring magnetized transport properties in high density plasma. In the case of UNP, the low plasma density cannot supply enough current density to create a large internal magnetic field. Again, making UNP ideal for studying transport properties in a magnetized UNP where the magnetic field is precisely known and controlled.

Magnetized transport properties is a growing field of research [20–29]. In HEDPs, magnetized transport property studies include anisotropic thermal conductivity [30] and reverse shock formation [31]. Similar experiments are performed using UNPs, these include thermal conductivity [32], diffusion [33], strong coupling enhancement [34], and various others [35–37].

In an UNP the electrons are much more easily magnetized than the ions. The magnetization is characterized by the magnetization parameter,

$$\alpha_s = \frac{\Omega_{cs}}{\nu_{ss}}, \tag{1.3}$$

where Ω_{cs} is the cyclotron frequency of a species, s,

$$\Omega_{cs} = \frac{eB}{m_s} \tag{1.4}$$

and ν_{ss} is the collision frequency as given by the plasma formulary [38].

When the magnetization parameter from Eq. refmagparam is $\alpha_s > 1$ then the respective plasma species in magnetized. In the case of our plasma, the electrons become magnetized when

$B > 0.0028$ T. The Ca^+ ions are magnetized when $B > 0.82$ T. UNP expansion is driven by the electron pressure [39, 40], by magnetizing the electrons the ion expansion is suppressed. In this work, we study plasma expansion in the limit that the electrons are magnetized, but the ions are not.

In Chapter 2 we report the first measurements of the ion-ion temperature relaxation rate using a strongly-coupled dual-species UNP [19]. This system allows precise control of the ion mass ratio and plasma stoichiometry. We show that within the experimental uncertainties, the measured temperature relaxation rates match the results of classical MD simulations.

In Chapter 3 we study expansion of a Ca^+ UNP in the presence of a strong uniform magnetic field. We explore a magnetic field strength regime of $B = 0 \rightarrow 0.123$ T, spanning a magnetization parameter for the electron and ions of $\alpha_i = 0 \rightarrow 0.15$ and $\alpha_e = 0 \rightarrow 45$ respectively. We measure the transverse and parallel expansion of an UNP and compare the experimental data to an ambipolar diffusion model developed by Zhang et al [33]. In the non-magnetized case, we compare our data to a self similar expansion model [39, 40].

Chapter 2

Temperature Relaxation in Strongly Coupled Binary Ionic Mixtures

2.1 Introduction

Advancing the frontier of dense plasma science requires a deep understanding of plasma processes in extreme and transient conditions. Accurately modeling high energy-density plasmas (HEDP) requires detailed and reliable models of collective phenomena such as continuum depression heating [4], turbulence and mixing [5–7], diffusion [8, 9], viscosity [10], and many other physical processes [1, 12]. These transport processes are critical components of modeling codes for laser-driven plasmas [41] and stellar atmospheres [42, 43].

Predicting transport coefficients in plasmas dominated by strong dynamical collision processes remains an unresolved issue [18]. Plasmas are considered strongly coupled when the ion coupling parameter Γ, defined as the ratio of the nearest-neighbor electrical potential energy to the average kinetic energy, is larger than 1. For plasma mixtures, the coupling parameter of species α is defined

as,

$$\Gamma_\alpha = \frac{(Z_\alpha e)^2}{4\pi\varepsilon_0 a_{\rm ws}} \frac{1}{k_B T_\alpha}, \tag{2.1}$$

where Z_α is the ion charge number, T_α is the temperature, and $a_{\rm ws} = (3/(4\pi n_{\rm tot}))^{1/3}$ is the average distance between ions, $n_{\rm tot} = \sum_\alpha n_\alpha$ is the total ion density. Strongly coupled plasmas are characterized by large-angle scattering with tight particle correlations and dynamical screening. The characteristic time scales for collisions and collective mode periods overlap, clouding the otherwise clear separation that typically simplifies theoretical models.

The challenge in plasma theory is that when $\Gamma \geq 1$, standard kinetic and hydrodynamic approximations are not entirely appropriate. For example, cross-sections in the Boltzmann equation accurately describe transport in plasmas characterized by binary ionic collisions [44]. In strongly-coupled plasmas, binary collisions are important, but they do not exclusively describe all the ion-ion interactions. Conversely, dielectric functions in the Lenard-Balescu equation appropriately describe transport when collisions are characterized by weak many-body scattering events [45, 46]. When neither of these two limits is realized, hybrid models are required [47]. One approach is to build the many-body screening into an effective potential and to use it when computing cross-sections, thereby capturing the strengths of both limits [44, 48, 49]. Carefully designed and accurately diagnosed laboratory experiments are required to test the reliability of these hybrid approaches [19]. One such experiment is presented in this paper.

Because most plasmas are created out of equilibrium, understanding temperature relaxation is critical for modeling the evolution of multi-temperature HEDPs [50–55]. Temperature relaxation has been studied extensively for electron-ion systems [45, 46, 56–63]. However, most plasma theories are tailored for the case of widely disparate mass (electrons and a single ion species). These theories have been compared to molecular dynamics (MD) simulations with varying degrees of success [58, 63]. However, explicit electron-ion MD simulations often rely on quantum statistical potentials [64, 65] which may only be valid in thermodynamic equilibrium [57]. This complicates

comparisons of MD simulations with theory, because disagreements can be attributed to uncertainties in the interaction potentials instead of theoretical models.

At a fundamental level, it is appropriate to ask when and if a two-temperature system can form. Simply mixing hot and cold particles together may result in a non-Maxwellian velocity distribution function, in which no true "temperature" is defined. In mixtures of particles with different masses, it is possible for each mass species to have an independently defined Maxwellian velocity distribution and, therefore, temperature. When the species' temperatures evolve slowly enough that the Maxwellian distributions are maintained, temperature relaxation becomes a meaningful concept. Electron-ion plasmas [50, 59, 66, 67] and electron-hole plasmas [68–70] are binary systems in which two temperatures are well established. However, understanding the basic physics of temperature relaxation therefore requires the ability to vary the mass ratio and to cleanly measure the time-evolving temperatures.

Ultracold neutral plasmas (UNPs) provide an idealized platform for measuring plasma transport properties [1, 71–74]. Recent laboratory experiments have shown UNPs to be effective HEDP simulators over a limited range of parameters [1, 19, 75–81]. Both UNPs and HEDPs can be described using dimensionless parameters. One of them is Γ, which involves ratios of temperature, charge, and density. Another is the Knudsen number, which involves a ratio of the ion mean free path divided by the characteristic length scale. The values of these dimensionless parameters are similar in both HEDPs and UNPs [82]. Therefore, UNP experiments can probe some interaction physics relevant to HEDP systems.

UNPs are strongly-coupled, non-degenerate, quasi-homogeneous, quasi-steady-state plasmas in which the charge state is well-known. The initial electron temperature is independent of the ion temperature, and it is chosen with sub-percent accuracy. The time-evolving temperatures and densities of each ion species are readily and simultaneously determined using identical techniques for each species. Furthermore, the equation of state for the electrons is well known, dramatically reducing

the complexity of interpreting experimental data and applying plasma models [83]. As HEDP simulators, UNPs test collision physics without the complications of high density, inaccessibly short time scales, high transient pressures, quantum potentials, and extreme optical opacity.

In this paper, we report the first measurements of the ion-ion temperature relaxation rate using a strongly-coupled dual-species UNP [19]. This system allows precise control of the ion mass ratio and plasma stoichiometry. We show that within the experimental uncertainties, the measured temperature relaxation rates match the results of classical MD simulations. The same sign of charge removes ambiguities in the choice of the ion-ion interaction potential. We compare rates extracted from these simulations with theoretical predictions in the few cases where the mass ratio dependence can be readily identified. We find reasonably good agreement with a recent model based on an effective Boltzmann equation [44]. Deviations are likely attributable to coupled modes [18].

2.2 Results

2.2.1 Dual-Species Ultracold Neutral Plasma

The central region of the dual-species UNP can be modeled as a homogeneous plasma mixture. Our dual-species UNP is formed by photo-ionizing laser-cooled Ca and Yb atoms in a magneto-optical trap (MOT) [1, 19]. The spatial density profile of the trapped neutral atoms is approximately spherically symmetric and Gaussian. To a good approximation, the spatial density profile is described by the function $n = n_0 \exp\left[-r^2/(2\sigma_0^2)\right]$. In our experiments, the initial rms sizes of the Ca and Yb atomic clouds σ_0 ranges from 300 to 1000 μm. The peak density n_0 of Ca and Yb ranges from 0.1 to 3.0×10^{10} cm^{-3}, depending on the MOT parameters. The temperature of the neutral atoms in the trap is around 0.002 K.

The ionization process uses ns-duration laser pulses to ionize Ca and Yb atoms at threshold, as described in the Methods section. This produces a very cold, metastable, out-of-equilibrium plasma

with separate temperatures for the electrons and each ion species. The electron temperature is determined by the photoionization laser wavelengths. However, the ion temperatures are determined by their mutual interaction after ionization. Typical values are T_e ranging from 10 to 1000 K and T_i in the range of 1 to 2 K, depending on the initial plasma density.

The density evolution in our dual-species UNP is shown in Fig. 2.1. For this measurement, the initial rms size of the neutral Ca atomic cloud ($\sigma_0 = 0.76$ mm) was chosen to be larger than the Yb atomic cloud ($\sigma_0 = 0.44$ mm). The peak plasma densities are $n_0^{\mathrm{Ca}} = 1.4 \times 10^{10}$ cm^{-3} and $n_0^{\mathrm{Yb}} = 2.7 \times 10^{10}$ cm^{-3}. The ions are singly-ionized ($Z = 1$) and the electron temperature is 96 K. As the plasma evolves, the larger mass and higher density of the Yb^+ ions ($m_{\mathrm{Yb}} = 174$ a.m.u.) prevents the central portion of the Ca^+ ion density distribution ($m_{\mathrm{Ca}} = 40$ a.m.u) from expanding. This "frictional" confinement of the Ca^+ ions occurs because the two species are strongly coupled together where the Yb^+ density is high.

As the plasma expands, the consequences of this confinement become apparent. Where the Yb^+ density gradient is high, the lighter Ca^+ ions are accelerated radially outward. In the cold plasma approximation, the momentum equation for a mixture of ions can be written as,

$$\frac{\partial \mathbf{u}_\alpha}{\partial t} = -\frac{k_{\mathrm{B}} T_e}{m_\alpha} \frac{\nabla n_e}{n_e} - \sum_{\beta \neq \alpha} \nu_{\alpha\beta}^{\mathrm{m}} \left(\mathbf{u}_\alpha - \mathbf{u}_\beta \right), \tag{2.2}$$

where $\nu_{\alpha\beta}^{\mathrm{m}}$ is the momentum relaxation collision frequency and $\mathbf{u}_\alpha$ is the hydrodynamic velocity of ion species $\alpha = \{\mathrm{Ca}, \mathrm{Yb}\}$. Details for these equations are given in the Methods section. Some of the Ca^+ ions find themselves between distant, hotter electrons and the heavier Yb^+ ions. The $\nu_{\alpha\beta}^{\mathrm{m}}$ collision frequency is lower in this region because the Yb $^+$ density is lower, decreasing the friction on the Ca^+ relative to the center of the plasma. These Ca^+ ions are accelerated outwards more quickly than the ones that are frictionally confined in the center of the Yb^+ distribution. Over time, the Ca^+ distribution becomes spatially bi-modal as shown in the top row of Fig. 2.1.

The bottom row of Fig. 2.1 plots u_z, the z-component of $\mathbf{u}_\alpha$, for both Ca^+ and Yb^+ near the center of the plasma at $y = 0$. From very early times in the plasma evolution, the hydrodynamic

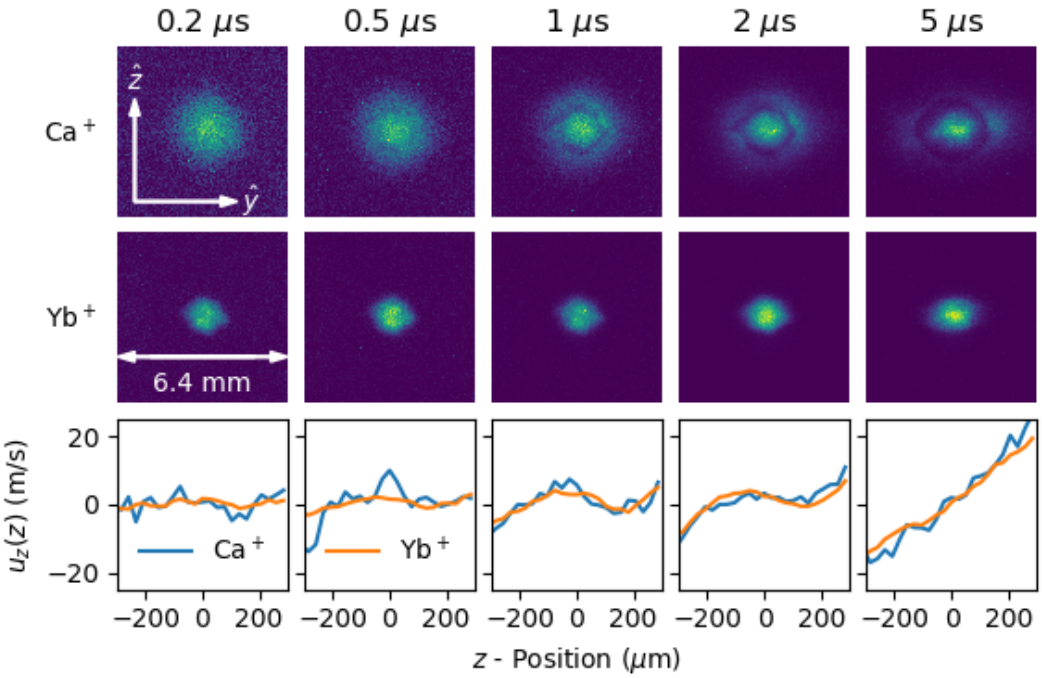

Figure 2.1 Expansion dynamics for a dual-species Ca^+/Yb^+ UNP. The top two rows show a vertical cut through the spatial density profile in the center of the plasma. The top row shows the Ca^+ density profile and the middle row shows the Yb^+ density profile. The bottom row shows $u_z(z)$, the z-component of the hydrodynamic velocity $\mathbf{u}_\alpha$ at the time labeled in the figure. The frictional confinement of the Ca^+ ions and also the demonstrated hydrodynamic flow locking justify a uniform-density MD simulation as described in the text.

velocity fields match. Frictional confinement of Ca^+ by the heavy Yb^+ ions flattens the velocity gradient in the center of the plasma for the first few microseconds. In the center of the plasma, collisions cause $\mathbf{u}_\alpha - \mathbf{u}_\beta \approx \mathbf{0}$.

This observed flow-locking suggests that it is appropriate to model the central region of the plasma as a homogeneous system with zero expansion velocity [84]. Note that this is no longer true at 5 μs. The density variations in our plasmas are not greater than $\pm 10\%$ when considering spatial regions $r < \sigma_0/2$ and for times $t < 0.3(\sigma_0/v_{\text{exp}})$ where v_{exp} is a characteristic expansion velocity [84]. For the plasmas considered in this paper, v_{exp} is dominated by the heavy Yb^+ ions and is typically $v_{\text{exp}} = (k_B T_e/m_{\text{Yb}})^{1/2} = 67$ m/s. For initial rms Yb^+ plasma sizes of $\sigma_0 = 0.72$ and 0.38 mm, for example, evolution times up to 3.2 and 1.7 μs, respectively, are appropriate for the homogeneous plasma model.

In the present work, we will focus on the temperature evolution in the center of the dual-species UNP. Because of the Ca^+ and Yb^+ mass difference, the initial temperatures of the two ion species are not equal. The heating process which occurs immediately after the plasma is generated asymmetrically deposits kinetic energy into the low-mass Ca^+ ions.

2.2.2 Two-Temperature Plasmas

The two-temperature nature of the plasma arises naturally because of the mass difference between the ion species. Although the ions initially retain the mK temperatures of the neutral atom cloud, the ion velocity distributions rapidly broaden as individual ions respond to the sudden appearance of neighboring ions [85]. One way to understand the ion response is to consider the time-evolving pair distribution function, $g(r,t)$. The pair distribution function indicates the probability density of finding a neighboring ion at some distance r at the time t. In the neutral atom cloud with essentially no interparticle interactions, $g(r,t)$ is constant everywhere and equal to 1. After ionization, as ions push neighboring ions away, the pair distribution function goes to zero near $r = 0$. Excess

electrical potential energy is converted to kinetic energy in this process, dramatically increasing the ion temperature [86, 87]. This process is called disorder-induced heating (DIH).

In a dual-species DIH process, the lower mass ions reach a higher temperature. The average kinetic energy of each species of ions in the plasma can be written as

$$k_B T_\alpha(t) = \frac{m_\alpha}{3N_\alpha} \sum_{i=1}^{N_\alpha} v_i^2(t), \tag{2.3}$$

where the index i indicates the particle of ion species α. We propagate the velocity in time using an Euler step, $v_i^2(t) = [\vec{v}_i(0) + \vec{a}_i(0)t]^2 = v_i^2(0) + 2\vec{v}_i(0) \cdot \vec{a}_i(0)t + a_i(0)^2 t^2$. In a uniform plasma with no spatial order and no bulk flow, the dot product $\vec{v}_i(0) \cdot \vec{a}_i(0)$ averages to zero and Eq. (2.3) simplifies to

$$\begin{aligned} k_B T_\alpha(t) &= \frac{m_\alpha}{3N_\alpha} \sum_{i=1}^{N_\alpha} \left[v_i^2(0) + a_i(0)^2 t^2 \right] \\ &= k_B T_\alpha(0) + \frac{t^2}{3N_\alpha m_\alpha} \sum_{i=1}^{N_\alpha} F_i^2(0), \end{aligned} \tag{2.4}$$

where we have used Newton's second law for the force magnitude F_i. This force is due to the electrostatic interaction and is mass independent. As Eq. (2.4) shows, the smaller mass will reach a higher temperature in the DIH process when the DIH timescale is faster than the thermal relaxation rate.

2.2.3 Molecular Dynamic Simulations

To gain greater insight into plasma dynamics, we perform molecular dynamics (MD) simulations. These are carried out using the Sarkas package, a pure python open-source molecular dynamics code for non-ideal plasma simulations [88]. UNPs are modeled as a collection of ions interacting via the screened Coulomb (Yukawa) potential,

$$U(r_{ij}) = \frac{Z_i Z_j e^2}{4\pi\varepsilon_0} \frac{1}{r_{ij}} e^{-r_{ij}/\lambda_{\mathrm{TF}}}. \tag{2.5}$$

where i, j label the ions in the simulation and r_{ij} their distance. The electrons are not explicitly simulated, but their effect is incorporated in the screening length, λ_{TF}, which is calculated from the electron density and temperature.

Typical MD simulation results are shown in Fig. 2.2. The temperature of each species is calculated using Eq. (2.3). The plot clearly shows DIH as the temperature rises during the first few hundred ns. The Ca^+ temperature is higher than the Yb^+ temperature as predicted in Eq. (2.4). After the first few μs, the two temperatures approach equilibrium.

Because UNPs are created out of equilibrium [85], we need to establish that the temperature is well-defined according to statistical mechanics. We do this by comparing the ion velocity distributions to a Maxwellian distribution, $\mathscr{M}(v)$, for each species. We use an analysis based on the Hermite expansion of distributions to quantify the deviations from a Maxwellian [89, 90]. The expansion reads as,

$$f(v,t) = \mathscr{M}(v) \sum_{n=0} \frac{1}{n!} a_n(t) \mathscr{H}_n(v), \tag{2.6}$$

where $\mathscr{H}_n(v)$ are the probabilistic Hermite polynomials of order n. In the case of a Maxwellian distribution the Hermite coefficients, a_n will all vanish except for $a_0 = 1$.

The result of this Hermite analysis is shown in Fig. 2.3. The top panels show time evolution plots of the Hermite expansion coefficients, $|a_2/2|$ and $a_4/4!$. The bottom panels quantify the deviations from a Maxwellian distribution. Panel (c) shows the percentage deviations of the Maxwellian rms width obtained from Eq. (2.6) and MD rms velocity. Panel (d) show the percentage of ions that lie outside a Maxwellian distribution. After ~ 1 μs, the two temperature system is well established. The fraction of ions that lie outside a Maxwellian distribution, calculated by fitting the MD velocity distribution to a normalized Gaussian and then integrating the absolute value of the difference, is only 2% after 1 μs.

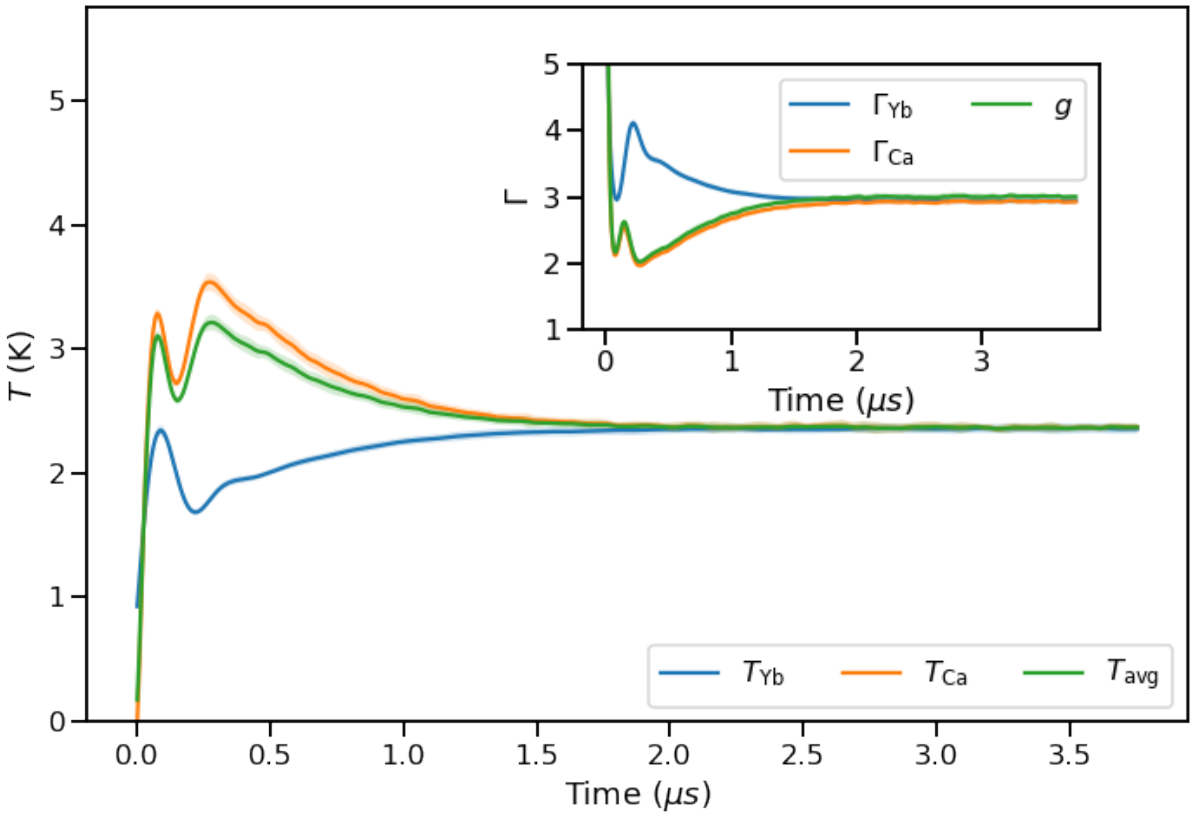

Figure 2.2 Temperature evolution of Ca^+/Yb^+ mixture from MD simulation with Ca^+ and Yb^+ densities of 4.3×10^9 cm^{-3} and 1.3×10^{10} cm^{-3}, respectively. For this simulation $\kappa = 0.395$, $T_e = 100$ K, $n_e = 1.73 \times 10^{10}$ cm^{-3}. T_{avg} is calculated from Eq. (2.10), $\Gamma_{\text{Yb,Ca}}$ from Eq. (2.1) and g from Eq. (2.19). The oscillations in the temperature during the first 0.5 μs are kinetic energy oscillations initiated during the DIH process [see Refs. [84] and [86]].

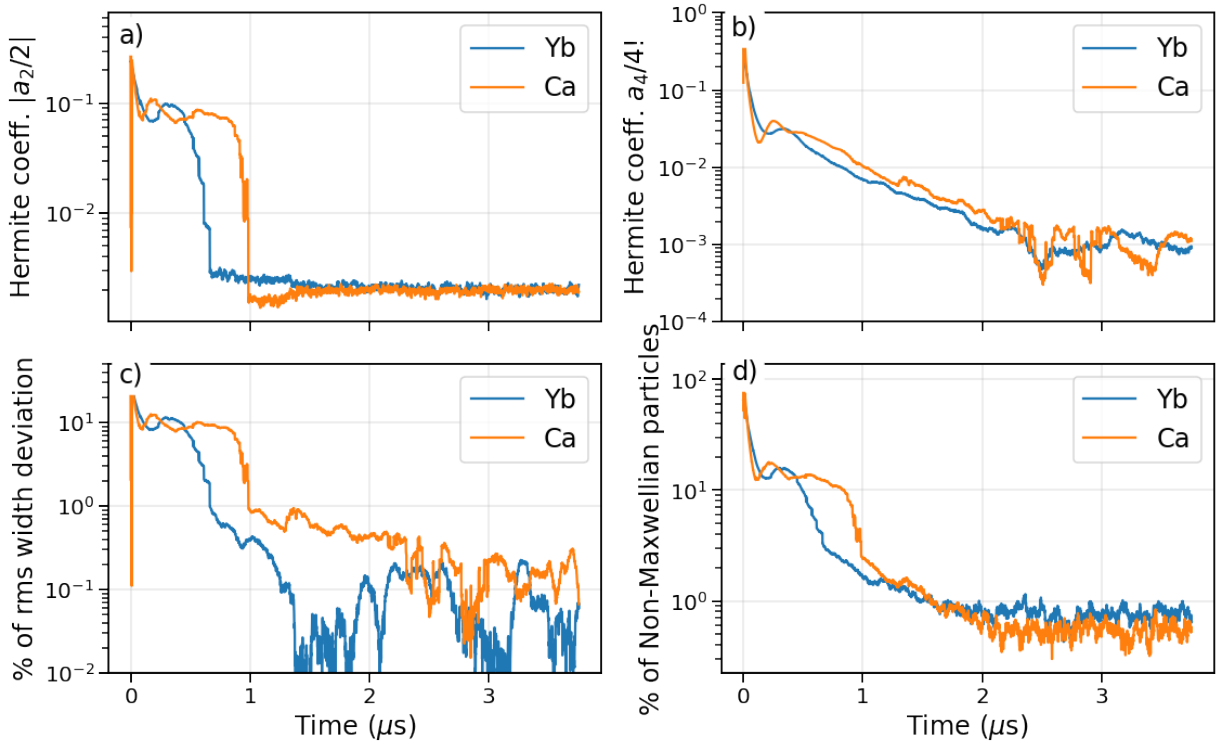

Figure 2.3 Time evolution of a) $|a_2/2|$ Hermite coefficient, b) $a_4/4!$ Hermite coefficient, c) percentage deviations of the Maxwellian rms width obtained from Eq. (2.6) and MD rms velocity, d) percentage of non-Maxwellian ions. Simulation parameters $n_0^{Yb} = 1.9 \times 10^9$ cm^{-3}, $n_0^{Ca} = 3.4 \times 10^9$ cm^{-3}, $T_e = 100$ K, $\kappa = 0.38$.

2.2.4 Theoretical Considerations

For the purpose of generalizing these experimental and simulation findings, we consider temperature thermalization using three different plasma theories. For high temperature, low density plasmas, these theories all agree. However, as the plasmas become colder and/or denser, theoretical predictions diverge. The divergence is entirely due to the treatment of collisions when the plasmas become strongly coupled.

In a spatially homogeneous plasma with two ion species, collisional temperature relaxation [91] is described as

$$\frac{dT_\alpha}{dt} = -\nu_{\alpha\beta}(T_\alpha - T_\beta), \tag{2.7}$$

where α, β refer to different ion species. The collision frequency $\nu_{\alpha\beta}$ depends critically on temperature, density, and charge. In general, the collision frequencies can be represented as

$$\nu_{\alpha\beta} = n_\beta \Phi \mathscr{S}, \tag{2.8}$$

where

$$\Phi = \left(\frac{Z_\alpha Z_\beta e^2}{4\pi\varepsilon_0}\right)^2 \frac{\sqrt{m_\alpha m_\beta}}{(m_\alpha + m_\beta)^{3/2}} \left(\frac{1}{k_B T_{\text{avg}}}\right)^{3/2}, \tag{2.9}$$

and

$$T_{\text{avg}} = \frac{m_\alpha T_\beta + m_\beta T_\alpha}{m_\alpha + m_\beta}, \tag{2.10}$$

and $\mathscr{S}$ is a model-dependent collisional integral.

We have formulated three theoretical models with increasing fidelity to reveal their physics sensitivities in the plasma regime of our experimental and simulation results. In particular, our plasmas are strongly coupled and have mass ratios much closer to unity than the electron-ion mass ratio.

Model 1

Our first model for $\mathscr{S}$ in Eq. (2.8) is based on the well known NRL Plasma Formulary result [see pp. 33-34 of Ref. [38]]. The NRL model is obtained from the Fokker-Planck equation that contains the well known Coulomb Logarithm (CL). In our plasmas, the NRL formulation for $\mathscr{S}$ is negative and cannot be used directly, indicating that strong scattering and screening is present, obviating the use of straight-line trajectories and standard Debye-Hückel screening models. To account for stronger scattering events, we extend the NRL straight-line-trajectory approximation to hyperbolic trajectories [56], here using cutoffs as in NRL,

$$\mathscr{S}^{(1)} = \frac{1}{2} \ln\left[1 + \left(\frac{b_{\max}}{b_{\min}}\right)^2\right], \tag{2.11}$$

where

$$b_{\max} = \left(\frac{1}{\lambda_1^2} + \frac{1}{\lambda_2^2}\right)^{-1/2}, \tag{2.12}$$

$$b_{\min} = \left(\frac{Z_1 Z_2 e^2}{4\pi\varepsilon_0}\right)\frac{1}{k_B T_{\text{avg}}}. \tag{2.13}$$

Equation (2.11) always yields a positive definite result and gives the NRL result in the limit of large values.

Model 2

Our second model addresses strong correlations by modifying the screening length to be consistent with the effective screening length of an ionic transport model [44]. In contrast to the screening length in Eq.(2.12), we consider an alternate screening length that includes electron screening and a correction for strong ion coupling. Choosing $b_{\max}$ to have the form

$$\lambda_{\text{eff}} = \left[\frac{1}{\lambda_{\text{TF}}^2} + \sum_{\alpha=1}^{2}\frac{1}{\lambda_\alpha^2 + a_{\text{ws}}^2/x_\alpha}\right]^{-1/2}, \tag{2.14}$$

guarantees that the screening length does not vanish at low temperature, but rather approaches the (species dependent) interparticle spacing through the factor a_{ws}^2/x_α (see Methods). The choice of this functional form that includes a_{ws} guarantees that the implied functional form of the binary interaction is consistent with numerical results in the strongly coupled regime [44]. The parameter λ_{TF} is the Thomas-Fermi length calculated from the electron temperature, T_e, and density, n_e, see Eq. (23) in Ref. [44] and represents electron screening. Note that Eq. (2.14) gives a positive definite value even at zero temperature. Our second model is then

$$\nu_{ij}^{(2)} = n_j \Phi_c \mathscr{S}^{(2)}, \tag{2.15}$$

$$\mathscr{S}^{(2)} = \frac{1}{2}\ln\left[1 + \left(\frac{2\lambda_{\text{eff}}}{b_{\min}}\right)^2\right]. \tag{2.16}$$

This model, when compared with the first, reveals the importance of strong interparticle correlations through Eq. (2.14).

Model 3

Our third model arises from the Chapman-Enskog expansion of the Boltzmann equation, using an effective screened interaction to numerically obtain a cross-section [44]. As such, consistent trajectories are included. There is no limit on the strength of scattering, and cutoffs are not needed.

Through a Bhatnagar-Gross-Krook approach [91], the relevant collisional frequency can be identified to be

$$\nu_{ij}^{(3)} = n_j \Phi \mathscr{S}^{(3)}, \tag{2.17}$$

$$\mathscr{S}^{(3)} = \frac{128}{3}\frac{\sqrt{\pi}}{2^{3/2}}\mathscr{K}_{11}(g), \tag{2.18}$$

where g is the thermally-averaged ion-ion Coulomb coupling factor,

$$g = \left(\frac{Z_1 Z_2 e^2}{4\pi\varepsilon_0}\right)\frac{1}{k_B T_{\text{avg}}}\frac{1}{\lambda_{\text{eff}}}. \tag{2.19}$$

Typical values in our experiments and MD simulations are $g > 1$ (see Fig. 2.2). The collision integral $\mathscr{K}_{11}(g)$ is calculated from

$$\mathscr{K}_{11}(g) = \begin{cases} -\frac{1}{4}\ln\left(\sum_k^5 a_k g^k\right) & g < 1 \\ \frac{b_0 + b_1 \ln g + b_2 \ln^2 g}{1 + b_3 g + b_4 g} & g > 1 \end{cases} \tag{2.20}$$

where $a_1 = 1.4660$, $a_2 = -1.7836$, $a_3 = 1.4313$, $a_4 = -0.55833$, $a_5 = 0.061162$, $b_0 = 0.081033$, $b_1 = -0.091336$, $b_2 = 0.051760$, $b_3 = -0.50026$, $b_4 = 0.17044$.

2.2.5 Comparison of Experiment, Simulation, and Theory

In Fig. 2.4 we plot the Ca^+ and Yb^+ ion temperatures and temperature differences from both the experiment and the MD simulations. For lower density plasmas in Fig. 2.4a, the laboratory temperature measurements and MD simulations agree well. For the higher density plasmas in Fig. 2.4b, the temperatures exhibit a systematic departure from the MD simulations. However,

the temperature difference plotted in Fig. 2.4d shows excellent agreement between the laboratory measurements and MD simulations. Given the velocity flow locking shown in Fig. 2.1 and also the dramatic flattening of the velocity gradient, we conclude that the hydrodynamic expansion has a negligible effect on the temperature measurements and the temperature difference, especially for $t < 1.5\ \mu$s. The disagreement in Fig. 2.4b may also be attributable to ion acoustic wave heating [75]. The small, dense neutral atom cloud from which the plasmas in Fig. 2.4b are derived expands for a short period of time before ionization, which likely allows density imperfections to persist.

In Fig. 2.5 we compare MD results with the theoretical predictions presented above. The three models can be compared with MD results only after each species has reached a Maxwellian velocity distribution. As presented above, the two species can be considered to be Maxwellian after $t \sim 1\mu$s. As stated previously, the progression of models begins with standard plasma theory that incorporates physically motivated ion trajectories, Eqs. (2.8)-(2.13) [56]. This is plotted as a dotted blue line, and it indicates a serious deficiency of standard plasma theory. This is expected since this model, Eq. (2.11), uses the ion Debye length as the maximum length scale.

The next level of improvement, Model 2, provides a correction for strong coupling when the Debye length becomes unphysically small, Eqs. (2.15)-(2.16). This is plotted as a dash-dot orange line. This strong coupling correction brings the theory closer to the simulations, but still underpredicts the relaxation rates.

Our best model, Model 3, is based on an effective potential in a Boltzmann description, Eqs. (2.17)-(2.19), which includes velocity dependent strong scattering. This is plotted as a dashed green line in Fig. 2.5. This incorporates strong scattering in a self-consistent way, reducing the ambiguity in choosing *ad hoc* cut off parameters inherent in a Coulomb logarithm approach. Nonetheless, this model predicts temperature relaxation rates somewhat faster than the MD result. This is surprising given the previously demonstrated accuracy of this model in reproducing experi-

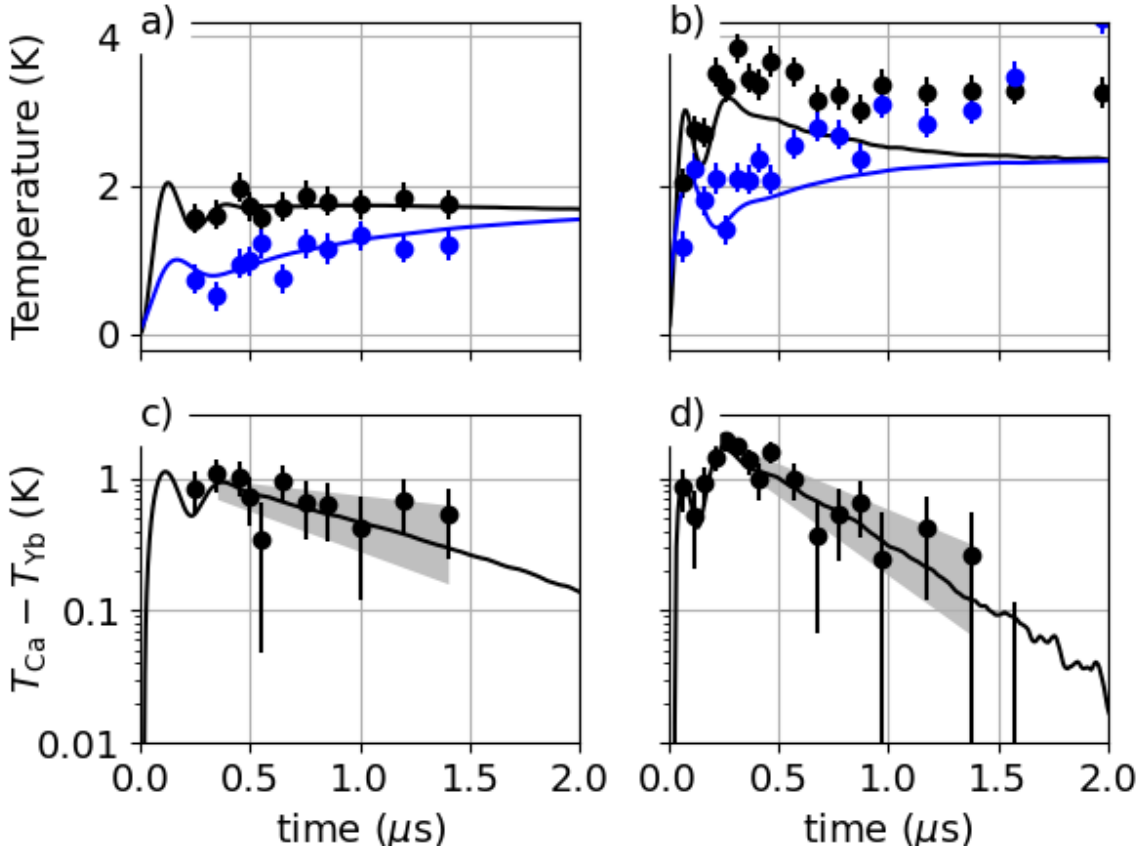

Figure 2.4 Temperature vs. time for two UNP configurations. a) T_{Ca} (black), and T_{Yb} (blue). For this plot, the initial peak densities and rms sizes are $n_0^{Ca} = 3.4 \times 10^9$ cm^{-3}, $\sigma_0^{Ca} = 0.57$ mm, $n_0^{Yb} = 1.9 \times 10^9$ cm^{-3}, $\sigma_0^{Yb} = 0.72$ mm. Circles show temperatures extracted from laboratory data. Solid lines show MD data. c) and d) Temperature difference, T_{Ca} - T_{Yb}. Circles show laboratory data with their 1σ estimated uncertainty. Solid lines show MD data. The gray shaded area represents the estimated 1σ uncertainties in the decay rate extracted from the laboratory data. Panels b) and d) show the same analysis for a higher density plasma with $n_0^{Ca} = 4.3 \times 10^9$ cm^{-3}, $\sigma_0^{Ca} = 0.53$ mm, and $n_0^{Yb} = 1.3 \times 10^{10}$ cm^{-3}, $\sigma_0^{Yb} = 0.38$ mm. For all of this data, the electron temperature is 96 K.

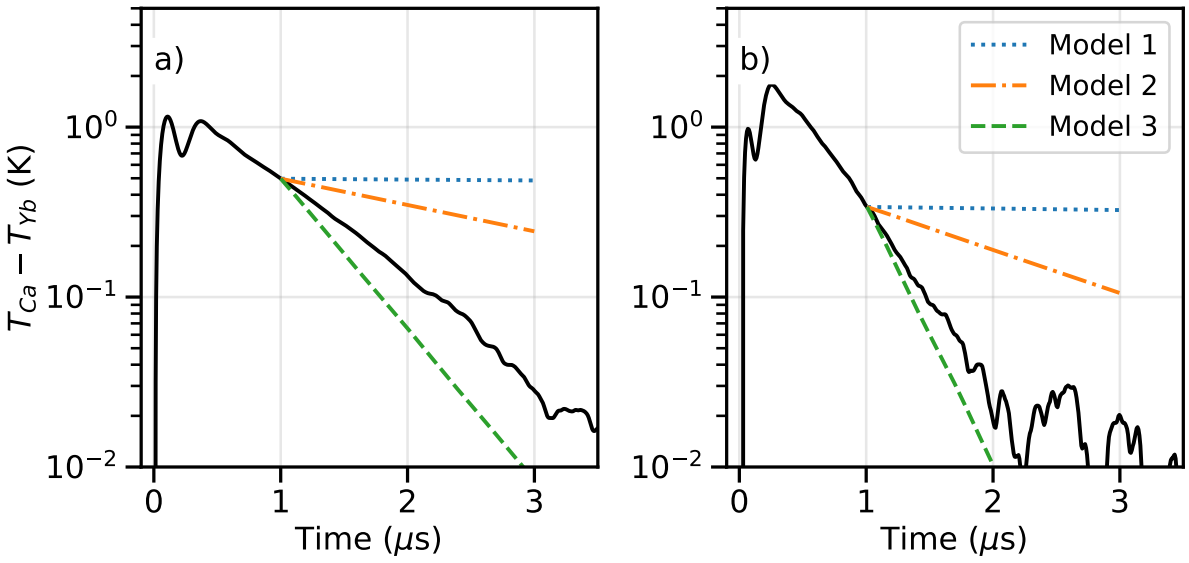

Figure 2.5 Semilog plot of the temperature difference $T_{\mathrm{Ca}} - T_{\mathrm{Yb}}$ compared with temperature relaxation models. Model 1 dotted blue line, Eqs. (2.8) - (2.13), Model 2 dash-dot orange line, Eqs. (2.15) - (2.16), Model 3 dashed green line, Eqs. (2.17) - (2.18) for the same systems as in Fig. 2.4. Simulation parameters $T_e = 100$ K, a) $\kappa = 0.38$, $n_0^{Yb} = 1.9 \times 10^9$ cm^{-3}, $n_0^{Ca} = 3.4 \times 10^9$ cm^{-3}, b) $\kappa = 0.46$, $n_0^{Yb} = 1.3 \times 10^{10}$ cm^{-3}, $n_0^{Ca} = 4.3 \times 10^9$ cm^{-3}. The systematic improvement of the models compared to the MD simulation is clearly shown.

mental data and MD simulations of momentum transfer, joule heating, diffusion, viscosity, thermal conductivity, etc. [1, 19, 44].

This overprediction may be due to errors in the effective potential, non-binary collisions, or coupled modes [61, 62, 92, 93]. The influence of the coupled mode can be identified when examining the dielectric response function $\varepsilon(\mathbf{k},\omega)$ of a binary plasma mixture. In the case of a binary ionic mixture, the temperature relaxation equation for species 1 is [18]

$$\begin{aligned}\frac{\mathrm{d}T_1}{\mathrm{d}t} &= \iint \frac{dk\,d\omega}{3n_1\pi^3}\,k^2\left(\frac{U_{12}(\mathbf{k},\omega)}{|\varepsilon(\mathbf{k},\omega)|}\right)^2\Big\{T_1\,\mathrm{Im}\left[\Pi_{21}A_{22}^*\right]\mathrm{Im}\,\hat{\chi}_{11}^{(0)} \\ &\quad -T_2\,\mathrm{Im}\left[\Pi_{12}^*A_{11}\right]\mathrm{Im}\,\hat{\chi}_{22}^{(0)}\Big\}. \end{aligned} \tag{2.21}$$

With the exchange $1 \rightarrow 2$ we obtain the equation for species 2. In the above equation $U_{12}(\mathbf{k},\omega)$ is the Fourier transform of the Yukawa interaction between the two ion species, $\hat{\chi}_\alpha^0(\mathbf{k},\omega)$ is the external response function of species α, $A_{\alpha\beta} = \delta_{\alpha\beta} - \tilde{U}_{\alpha\beta}\Pi_{\alpha\beta}(\mathbf{k}\omega)$, and the elements of the matrix $\Pi(\mathbf{k}\omega)$ are defined by,

$$\Pi_{\sigma\sigma'}(\mathbf{k},\omega) = \chi_\sigma^{(0)}(\mathbf{k},\omega)[1 - G_{\sigma\sigma'}(\mathbf{k},\omega)], \tag{2.22}$$

where $\chi_\sigma^{(0)}(\mathbf{k},\omega)$ is the free particle polarizability and $G_{\sigma\sigma'}(\mathbf{k}\omega)$ is the local field correction. The three models described above neglect the frequency dependence of $\varepsilon(\mathbf{k},\omega)$ and consider only the static version $U_{12}(k)/\varepsilon(\mathbf{k},0)$. This effective interaction is then used to inform the Coulomb logarithm in a Fokker-Planck approach (Model 1 and Model 2) or the cross-section in a Boltzmann equation (Model 3). It is worth noting that Eq. (2.21), which describes the interaction of classical ions, has wide applicability to most non-ideal plasmas, with transferability guaranteed through the choice of the most appropriate pair interaction [94].

In general, the effective interaction is time and frequency dependent. The electron-ion and ion-ion dynamics need to be considered when extending plasma models to include coupled modes. Some of these processes harden the ion-ion potential, while others soften it. Future work is needed in this direction.

2.3 Discussion

We demonstrate that dual-species UNPs provide a new platform for studying ion transport properties in a two-temperature system. We characterized the approach to equilibrium using a Hermite expansion, which reveals when a relaxing system can be safely treated as a “two-temperature" system. This powerful approach facilitates comparison of data with quasi-equilibrium theories.

We present the first measurement of ion-ion temperature relaxation rates in a strongly coupled binary ionic mixture. Using a single diagnostic method, we directly measure the ion temperatures without inference through, for example, an equation of state. This shows the remarkable capability for UNPs to investigate component physics across coupling regimes, simulating some aspects of, *e.g.* HEDP, plasma mixtures, and liquid metal alloys.

We show that our MD simulations of temperature relaxation agree with experimental measurements. This reinforces the fact that the Yukawa potential, Eq. (2.5), accurately describes ion-ion interaction in dual-species UNP mixtures. This further confirms the ability of our MD simulations to capture a very complex relaxation process. This confidence, in turn, allows us to employ the MD as a surrogate for information that the experiment cannot provide, as the Hermite coefficients. These observations reinforce the importance of having MD as an integral part of experimental workflows.

We compare the simulated relaxation rates with three popular temperature relaxation theories of varying fidelity. The closest theory is based on solving the Boltzmann equation using an effective potential. The variance between this theory and the MD simulations is likely caused by coupled modes, an effect that is omitted from the theory by design. Future work could explore the influence of coupled modes on ion transport. Incorporating coupled modes into the Boltzmann solutions could also prove fruitful for ion transport in the regime of relatively small mass ratios.

2.4 Methods

Experimental details

We use resonant two stage photo-ionization to ionize 100% of Ca atoms and up to 60% of Yb atoms. The wavelengths are shown in Fig. 2.6. The ionization pulses are offset by 40 ns to prevent the Ca ionization pulses from ionizing the Yb atoms. Otherwise, cross-ionization between the two plasmas would confound the electron temperature, as shown in Fig. 2.7. The electron temperature is determined by the photon energy of the ionizing pulse above the ionization threshold, and $T_e = 96$ K in these experiments. The initial plasma densities are controlled by expanding the neutral atom cloud prior to ionization, also illustrated in Fig. 2.7. The Ca and Yb atom clouds expand for different lengths of time up to 2 ms, allowing independent control of the relative densities of each species. The process of loading the neutral atom trap, expanding the neutral atom clouds, and generating the plasma takes several ms and the process is repeated at a rate of 10 Hz.

The Ca^+ and Yb^+ velocity distributions are measured using laser-induced-fluorescence. Probe laser beams at 393 (Ca^+) and 369 nm (Yb^+) are overlapped using a dichroic mirror and then coupled into a single mode polarization maintaining optical fiber. The fiber output is collimated with a Gaussian waist of 3.9 mm and then cylindrically focused ($f_{\mathrm{cyl}} = 350$ mm) to a rms thickness of 0.15 mm to illuminate a sheet of ions in the center of the plasma [84] (see Fig. 2.8. The probe laser beam intensities are typically 10 to 20% of the saturation intensity.

For long interrogation times, $t > 1$ μs, optical pumping is potentially problematic. For the 393 nm transition in Ca^+, lasers at 854 and 850 nm could be used to prevent optical pumping into the metastable ^2D states [95]. Throughout these experiments, we use a laser at 854 nm to prevent optical decay into the $3d\ ^2D_{5/2}$ level. We initially also used a laser at 850 nm to prevent decay into the $3d\ ^2D_{3/2}$ level. However, we found that including this laser did not change the measurement results. In later experiments, the 850 nm laser was not used.

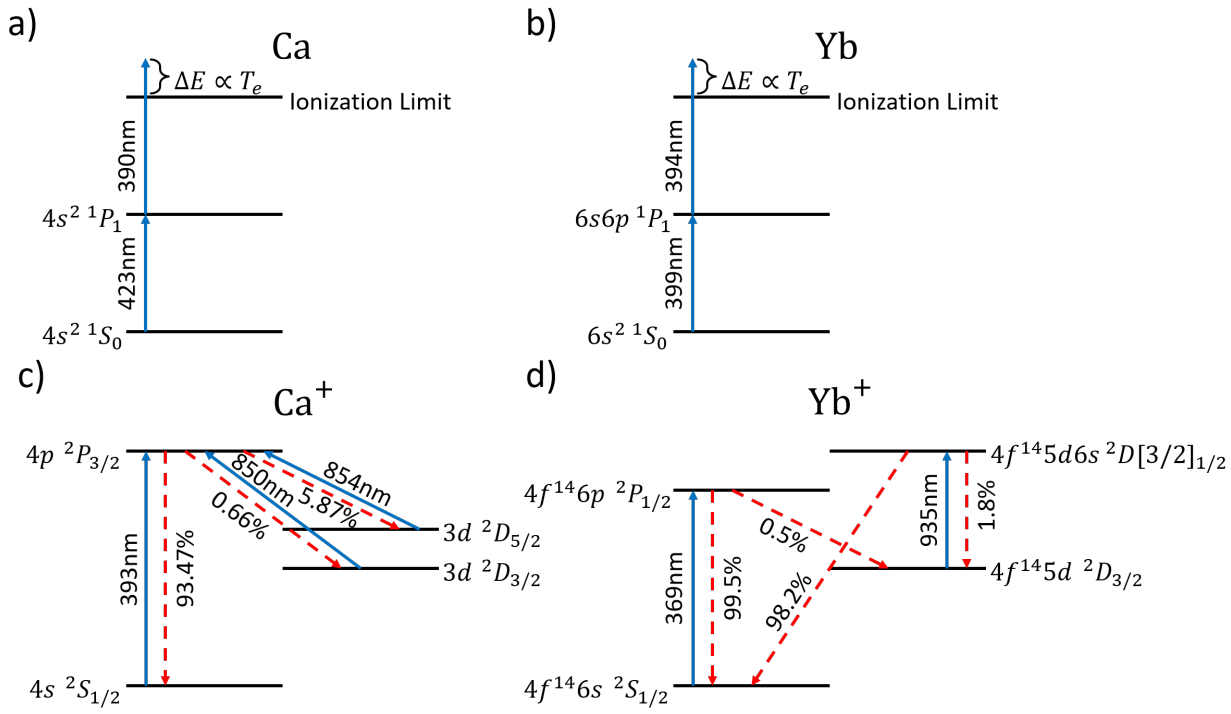

Figure 2.6 Atomic energy levels and laser wavelengths used in this experiment. Blue arrows in a) and b) indicate the lasers used for ionizing Ca and Yb, respectively. The electron energy is given by the difference between the ionization limit and the laser photon energy. c) and d) show levels used in Ca^+ and Yb^+ spectroscopy, respectively. The blue arrows indicate the laser driven transitions, while the red dashed arrows indicate the spontaneous emission with the associated branching fractions. In this experiment, we use a Ti:sapphire laser to repump the 854 nm transition in Ca^+. Repumping the transition at 850 nm does not change the measured results. We do not repump the 935 nm transition in Yb^+.

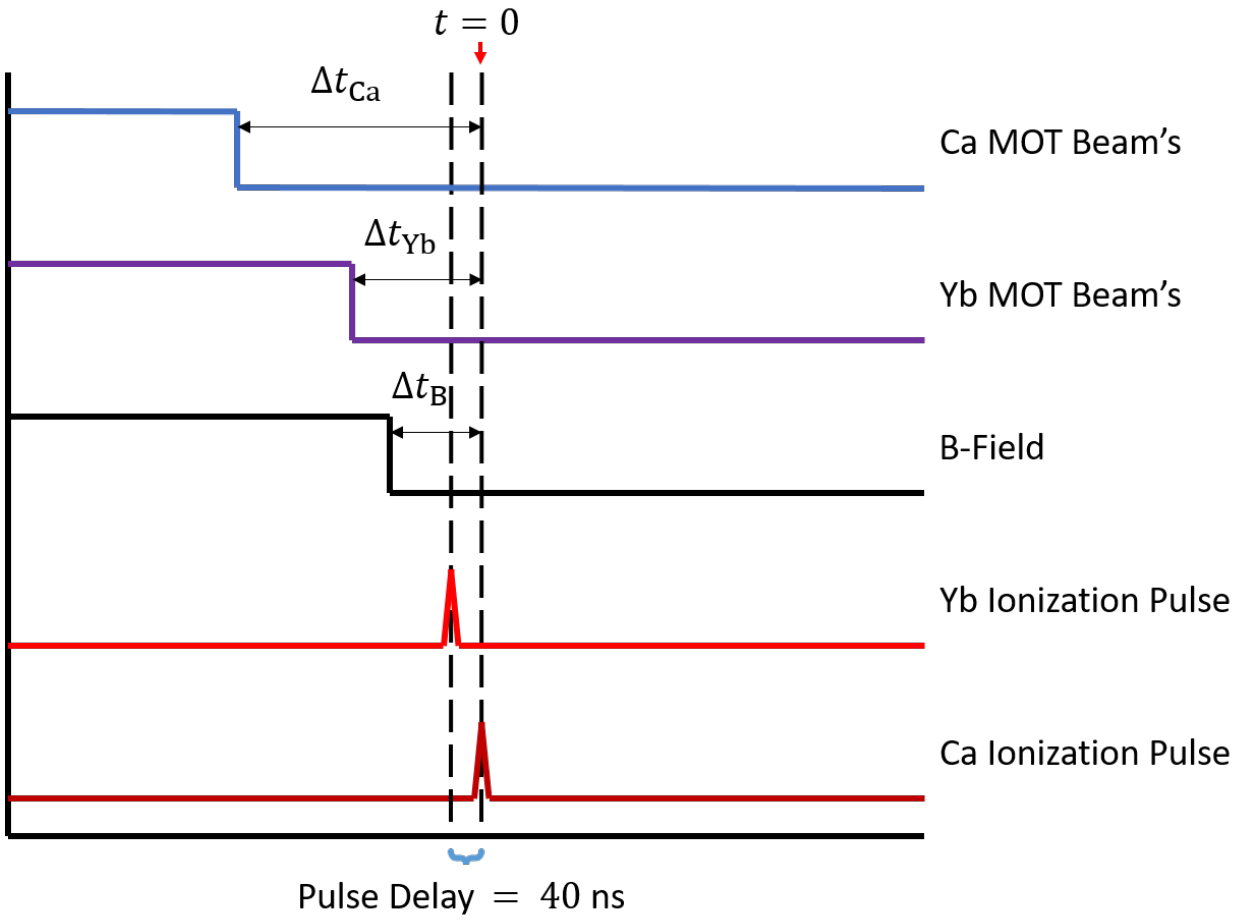

Figure 2.7 Timing diagram for density selection and plasma creation, where a step-up indicates turning on and a step-down indicates turning off the indicated quantity. The Ca and Yb neutral atom clouds are expanded for Δt_{Ca} and Δt_{Yb} to obtain the desired densities, typical expansion times range between 0.5 ms and 2 ms. The pulse delay for the ionization pulses is 40 ns to eliminate cross ionization to preserve the known electron temperature of the plasma. Otherwise, the Ca^+ ionization pulses would also ionize the Yb atoms and produce a very high electron temperature. Due to the large ion mass, the Yb^+ plasma does not expand on this 40 ns timescale. Data plotted in previous figures also have this 40 ns delay. Its influence is imperceptible in the data. The MOT magnetic field is turned off $\Delta t_{\mathrm{B}} = 500\ \mu$s prior to ionization.

We further verify that optical pumping is a negligible source of error in both Ca^+ and Yb^+ by turning the probe laser beams on for short periods of time and delaying the turn-on time for up to 10 μs. We find that for our probe laser intensities, there is no difference between these measurements and those derived from leaving the probe lasers on all of the time.

Details of the laser-induced fluorescence measurement process are given in Fig. 2.8. With the probe laser frequencies at a particular offset from resonance, we collect fluorescence as a function of time after the plasma is created. Fluorescence measurements from up to 100 identical plasmas are averaged at a given frequency of the probe lasers. The probe laser frequency is changed, and the measurement process is repeated. Using 11 different probe laser frequency offsets, we sample the ion velocity distributions, using the Doppler shift to convert frequency offset to ion velocity. The data is post-processed so that at a given time after ionization, the fluorescence signal as a function of *frequency* is fit to a Voigt profile, and the rms Gaussian width, $v_{\alpha,\mathrm{th}}$, is used as a fit parameter. This is used to determine the ion temperature, T_α. Using the ICCD camera allows us to collect fluorescence averaged over a particular time. Typical averaging times are 50 to 500 ns, usually 10% of the delay time, depending on the ion dynamics under consideration.

Derivation of the fluid expansion model

We model the UNP as a three-species plasma composed of electrons and two ionic species. The species momentum equations are obtained from the velocity moments of the underlying kinetic description and are given by

$$n_\alpha \frac{\partial \mathbf{u}_\alpha}{\partial t} + n_\alpha \mathbf{u}_\alpha \cdot \nabla \mathbf{u}_\alpha + \frac{1}{m_\alpha} \nabla p_\alpha - \frac{\mathbf{F}_\alpha}{m_\alpha} n_\alpha = \mathscr{C}_\alpha, \tag{2.23}$$

where $\alpha = \{e, \mathrm{Ca}, \mathrm{Yb}\}$. Apart from the time derivative, this model describes advection, pressure forces, external and internal forces, and collisions. Approximations relevant to our ultracold plasma experimental conditions can be made, and include steady state electrons ($\partial \mathbf{u}_e / \partial t \approx 0$ on the ion

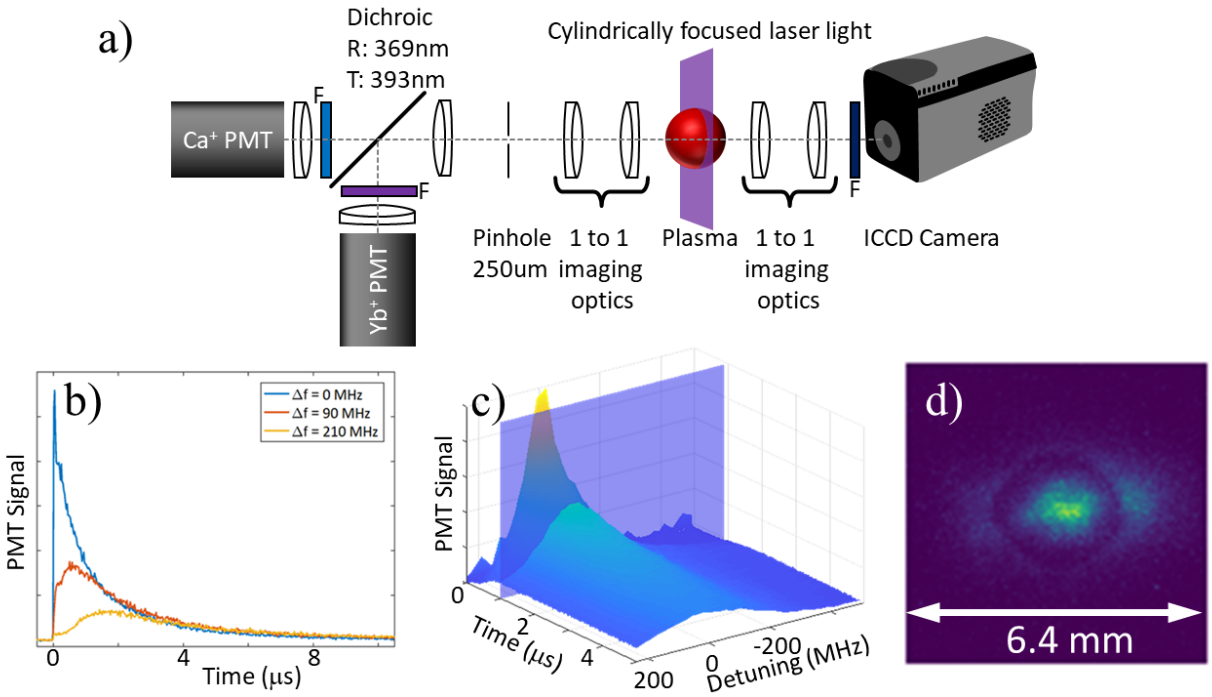

Figure 2.8 Experimental details for fluorescence detection from Ca^+ and Yb^+ ions. a) Schematic diagram of the optical system used for fluorescence detection. The plasma is illuminated by cylindrically focused laser light. Laser-induced fluorescence is collected using an $f/2$ 1:1 imaging system. For PMT measurements, the plasma is imaged onto a $\phi = 250$ μm aperture, enabling measurements of the central portion of the plasma. Spectral filters in front of the PMTs allow simultaneous measurements of fluorescence from both Ca^+ and Yb^+ ions. A spectral filter is also used before the ICCD camera. b) Typical laser-induced fluorescence PMT signals for Ca^+. c) A representation of Ca^+ laser-induced fluorescence measurements vs. time as a function of probe laser frequency detuning. The blue plane cutting through the data at 1 μs is used to extract the fluorescence vs. probe laser frequency detuning at a particular time. d) Typical Ca^+ fluorescence ICCD camera image when Yb^+ ions are present after a time-evolution of 5 μs. Camera measurements give spatial information at a particular time after ionization.

time scales of interest here), small velocities among all species ($\mathbf{u}_\alpha \cdot \nabla \mathbf{u}_\alpha \approx 0$), vanishing pressure for the (ultracold) ions ($p_{\mathrm{Ca}}, p_{\mathrm{Yb}} \approx 0$), internal electrostatic forces and a friction term between ionic species. With these approximations, Eqs. (2.23) become,

$$\nabla P_e = n_e \mathbf{F}_e, \tag{2.24}$$

$$\frac{\partial \mathbf{u}_1}{\partial t} = \frac{\mathbf{F}_1}{m_1} - \nu_{12}^{\mathrm{m}}(\mathbf{u}_1 - \mathbf{u}_2), \tag{2.25}$$

$$\frac{\partial \mathbf{u}_2}{\partial t} = \frac{\mathbf{F}_2}{m_2} - \nu_{21}^{\mathrm{m}}(\mathbf{u}_2 - \mathbf{u}_1), \tag{2.26}$$

where the subscripts 1 = Ca and 2 = Yb. These equations are coupled to the species continuity equations and a Poisson equation for the electric fields. Assuming the electrons are isothermal and $Z = 1$, we obtain,

$$\frac{\partial \mathbf{u}_1}{\partial t} = -\frac{k_{\mathrm{B}} T_e}{m_1} \frac{\nabla n_e}{n_e} - \nu_{12}^{\mathrm{m}}(\mathbf{u}_1 - \mathbf{u}_2), \tag{2.27}$$

$$\frac{\partial \mathbf{u}_2}{\partial t} = -\frac{k_{\mathrm{B}} T_e}{m_2} \frac{\nabla n_e}{n_e} - \nu_{21}^{\mathrm{m}}(\mathbf{u}_2 - \mathbf{u}_1). \tag{2.28}$$

Simulation details

MD simulations are performed for a binary ionic mixture of Yb^+ and Ca^+ ions with a uniform spatial density. The two ion species interact via the screened Coulomb (Yukawa) potential

$$U(r_{ij}) = \frac{Z_i Z_j e^2}{4\pi\varepsilon_0} \frac{1}{r_{ij}} e^{-r_{ij}/\lambda_{\mathrm{TF}}},$$

where i, j label the ions in the simulation, r_{ij} their distance, and λ_{TF} is the Thomas-Fermi length obtained from the surrounding electrons [44, 96]. The electrons are not explicitly simulated, but their effect is incorporated in the screening length λ_{TF} which is calculated from the electron density, $n_e = n_{\mathrm{Ca}^+} + n_{\mathrm{Yb}^+}$, and temperature T_e. For temperature and densities considered here, the electrons are non-degenerate and λ_{TF} is equal to the Debye length of the electrons.

The simulations use periodic boundary conditions. While the experiments necessarily have open boundary conditions, the MD simulations are an appropriate representation of the middle of the plasma, as mentioned previously.

MD simulations are performed using Sarkas, a pure python open-source molecular dynamics code for non-ideal plasmas [88]. We use $N = 50\,000$ total ions, with Ca/Yb number ratios matching those of the experiments and $Z_{\mathrm{Ca}^+} = Z_{\mathrm{Yb}^+} = 1$. The initial positions of the ions are randomly distributed along the three axes of the simulation box. The initial velocities are chosen from a normal distribution centered at zero with an initial width $v^{(0)}_{\alpha,\mathrm{rms}} = \sqrt{k_B T_0/m_\alpha}$ with $T_0 = 0.002$ K. Particle positions and velocities are integrated using the standard velocity Verlet algorithm. The timestep, Δt, was chosen such that $\omega_p \Delta t \sim 0.002$, where $\omega_p^2 = \omega_{\mathrm{Ca}}^2 + \omega_{\mathrm{Yb}}^2$ is the sum of the plasma frequencies of each ion species (see the Theoretical details' section for definitions). The timestep and total number of particles were varied and chosen to give converged results.

The potential energy and forces are calculated using a highly efficient Particle-Particle Particle-Mesh algorithm [97]. This algorithm is more reliable than the minimum image convention when the screening parameter $\kappa = a_{\mathrm{ws}}/\lambda_{\mathrm{TF}} < 1$.

For each experimental condition, five non-equilibrium simulations with different initial conditions were performed on an Intel Core i7-8700K and 48 GB of RAM. Typical runtime for a single simulation run was ~ 20 hours.

Following the experiments, in the first 40 ns of the simulation Ca atoms are neutral, *i.e.* their charge number, $Z_{\mathrm{Ca}} = 0$, while Yb^+ ions carry a charge $Z_{\mathrm{Yb}^+} = 1$. In this way, only the Yb^+ ions interact with each other and do not interact with Ca atoms. For $t \geq 40$ ns the charge number of Ca atoms is changed to 1 and the screening length λ_{TF} is updated. This leads to a larger screening parameter κ due to the increased electron density. In this work, the electron temperature is $T_e = 96$ K and the densities range from $n_e = 1.9 \times 10^9$ cm^{-3} to 1.3×10^{10} cm^{-3}, leading to final values of the screening parameter $\kappa \sim 0.37 - 0.46$. In this range, three-body recombination is negligible [98].

We performed more simulations without the initial time delay of 40 ns and found no difference in the results. A back-of-the-envelope calculation shows that the averaged displacement of the Yb^+ ions in the first 40 ns is ~ 100 nm, hence, not a significant change over the length scales of the system.

Comparison of experiment and simulations

To enforce compatibility in comparing the MD data to the experiment, the MD velocity distribution is convolved with a Lorentzian distribution and then fit to a Voigt profile with the Gaussian width as a fit parameter. This slightly underestimates the average ion kinetic energy during the DIH phase because of slight departures from a Maxwellian velocity distribution (see Fig. 2.3). Experimentally, we have access to the ion velocity distribution through the fluorescence signal. This signal is necessarily a convolution of the velocity distribution with the natural lineshape of the atomic transition. The half-width at half-maximum of the (Lorentzian) Ca^+ 393 nm transition is 11.5 MHz [99]. This corresponds to a velocity of 4.5 m/s. This is small compared to the post-DIH (Gaussian) rms velocity of 20 m/s for Ca^+ ions at a temperature of 2 K. Convolving the MD velocity distribution and fitting to a Voigt profile reduces the ion temperature by a few percent during the DIH phase, as illustrated in Fig. 5 of Ref. [84].

Theoretical details

The models consider a spatially homogeneous plasma composed of two ion species with different masses, m_α, different number densities, n_α, and charge numbers, Z_α. The surrounding negative electronic background is at temperature T_e and density $n_e = Z_1 n_1 + Z_2 n_2$. The Wigner-Seitz radius is defined from the total ion number density, $a_{\rm ws}^3 = 3/(4\pi n_{\rm tot})$, $n_{\rm tot} = n_1 + n_2$. The concentration of each ion species is $x_\alpha = n_\alpha / n_{\rm tot}$. The electron density $n_e = n_{\rm tot}$ when $Z_1 = Z_2 = 1$, as is true for our UNPs. The ion Debye length of species α is $\lambda_\alpha^2 = \varepsilon_0 k_B T_\alpha / (n_\alpha (Z_\alpha e)^2)$. The ion plasma

frequency of species α is $\omega_\alpha^2 = (Z_\alpha e)^2 n_\alpha/(\varepsilon_0 m_\alpha)$. The total ion plasma frequency is $\omega_p^2 = \sum_\alpha \omega_\alpha^2$. The ion thermal speed of species α is given by $v_{\alpha,\mathrm{th}} = \sqrt{k_B T_\alpha/m_\alpha}$. Typical equilibrium values in our experiments are $\Gamma_\alpha = 3$, as shown in Fig. 2.2.

Acknowledgements

We thank Dr. Jeffrey Haack of Los Alamos National Laboratory for useful conversations. M.S.M. and L.G.S. were supported by the U.S. Air Force Office of Scientific Research Grant No. FA9550-17-1-0394. R.T.S and S.D.B. acknowledge support from the U.S. Air Force Office of Scientific Research Grant No. FA9550-17-1-0302 and the National Science Foundation Grant No. PHY-2009999.

Chapter 3

Ultracold Neutral Plasma Expansion in a Strong Uniform Magnetic Field

3.1 Introduction

Ultracold neutral plasmas (UNPs) are useful tools in understanding transport properties of strongly coupled systems in an ideal environment. It has been shown that UNPs and high energy-density plasma (HEDP) share dynamic properties [1] when the one component Yukawa potential [2, 3] is appropriate. Accurately modeling HEDPs requires detailed and reliable models of collective phenomena such as continuum depression heating [4], turbulence and mixing [5–7], diffusion [8, 9], viscosity [10], thermal decoupling [11] and many other physical processes [1, 12]. The high optical opacity and short dynamic time scales in HEDPs pose challenges to experimentally measuring transport properties with high fidelity. For this reason, HEDP heavily rely on molecular dynamics (MD) simulations [14] and plasma models [15, 16] to understand transport in these complex systems. UNPs have the advantage of being 12 orders of magnitude below solid density with a temperature on the order of a Kelvin, resulting in accessible real-time plasma dynamic measurements [1]. Transport

properties in this environment are measured directly and can be used to verify current models and MD simulations [17–19].

There is a growing interest in magnetized transport properties in the plasma physics community [20–29]. In HEDPs such interests include anisotropic thermal conductivity [30] and reverse shock formation [31]. Similar experiments are performed using UNPs, these include thermal conductivity [32], diffusion [33], strong coupling enhancement [34], and various other studies [35–37]. It has been demonstrated by Gorman *et al.* [100] that the presence of a static quadruple magnetic field along with traditional magneto-optical trap (MOT) fields can be used to confine a strongly coupled Strontium plasma. The development of experimental UNPs provides a platform for studying magnetized plasma transport properties in these strongly coupled systems.

In this work, we present a new method for measuring plasma expansion in a uniform magnetic field using circularly polarized state-selective laser induced fluorescence. The presence of the magnetic field opens pathways to numerous Zeeman split dark states, including an aggressive optically dark ground state that complicates the time resolved spectroscopy considerably. Laser induced fluorescence has the advantage of obtaining real time temperature measurements at a localized point within the plasma [17] as well as precision size measurements through optically filtered imaging. This work allows for the capability of measuring magnetized transport properties of single and dual species plasma in a strong uniform magnetic field up to 0.2 T. Possible magnetized plasma experiments include diffusion, viscosity, thermal conductivity, ion-ion energy relaxation and disorder induced heating suppression.

A recent publication by Zhang *et al.* [33], showed that the transverse plasma expansion is suppressed in a magnetic field. In their work, they measured the plasma expansion by accelerating the ions towards a position-sensitive detector using an electric field. The element Xe was used, and they measured the expansion of the plasma at magnetic field strength up to 70 Gauss. They claimed that the expansion velocity scales as $B^{-1/2}$ and can be accurately modeled using ambipolar diffusion.

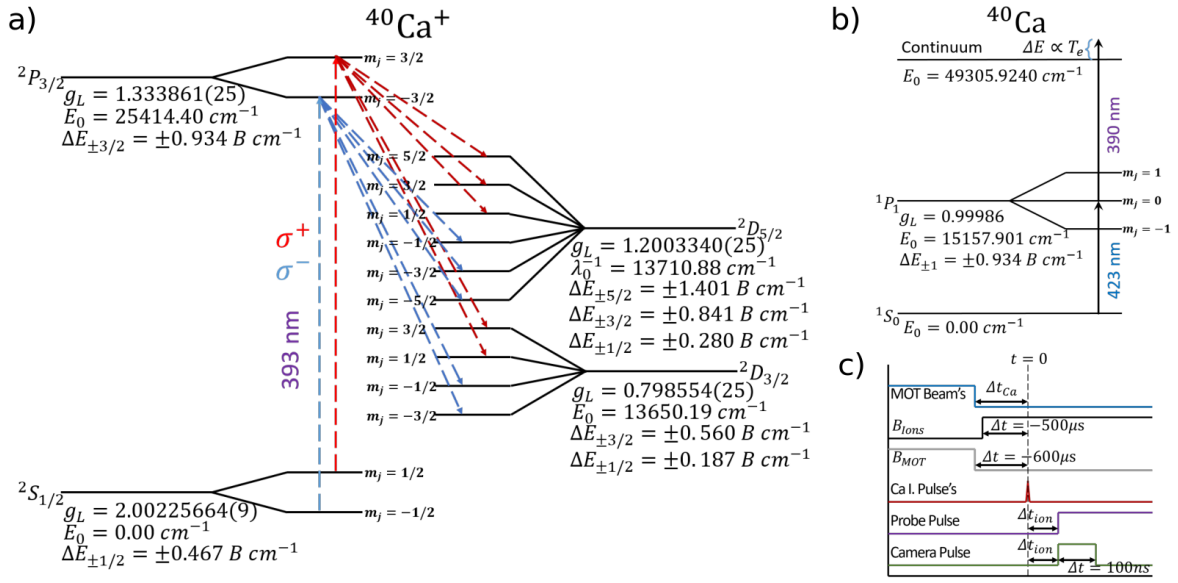

Figure 3.1 Relevant Energy level and timing diagrams. a) Energy leave diagram of the optimal fluorescent transition and the available dark states depending upon laser beam polarity. Other excitation states allow for an aggressive dark ground state due to the Zeeman splitting of the ground state. b) Energy level diagram for two stage photoionization. In this work, we drive the $^1S_0 \rightarrow {}^1P_1(m_j = 0) \rightarrow$ continuum transitions using a 423 nm and 390 nm pulses. The energy of the 390 nm pulse laser over the continuum sets the plasma electron temperature. c) Timing diagram for the experimental process. The MOT laser beams are turned off $\Delta t_{Ca} = 600\ \mu$s prior to ionization. The MOT magnetic field is turned off 600 μs prior to ionization. A short time later, the magnetic field for the plasma is turned on 500 μs prior to ionization. this gives time for the field to ramp up to a constant magnetic field strength. At time $t = 0$ the plasma is ionized and a short time, Δt_{ion}, later the probe laser is turned on, and the camera is pulsed on for 100-200 ns. Values of the Landé g-factor come from Refs. [101, 102] and [103].

We perform a similar experiment using laser induced fluorescence to observe the transverse and parallel expansion of the plasma in the presence of a strong uniform magnetic field up to 0.12 T or 1200 Gauss. Contrary to the finding by Zhang *et al.*, we find that ambipolar diffusion fails to model magnetized and non-magnetized UNP expansion. We find that the expansion velocity scales as the exponential of the magnetic field. Mathematically, at low magnetic fields, $B < 100G$, the exponential and power law models are indistinguishable. At large magnetic fields, the exponential relation is in better agreement with experimental data.

Unfortunately, at this time, no analytic solution has been derived for describing diffusion in a UNP in the presence of a magnetic field. In our plasma, the electrons are strongly magnetized, but the ions are not. The magnetization is characterized by the magnetization parameter,

$$\alpha_s = \frac{\Omega_{cs}}{\nu_{ss}} \tag{3.1}$$

where Ω_{cs} is the cyclotron frequency of species s and ν_{ss} is the intra-species collision frequency, as given by the plasma formulary [38]. For electrons, $\nu_{ee} \simeq \nu_{ei}$. The Larmor radius, r_L, defines the orbit of the species in a magnetic field,

$$r_L = \frac{m_s v_\perp}{eB}, \tag{3.2}$$

where m_s is the species mass, B is the magnitude of the magnetic field, e is the fundamental unit of charge and $v_\perp$ is the perpendicular thermal velocity,

$$v_\perp^2 = \frac{2}{3}\frac{k_B T_{s0}}{m_s}, \tag{3.3}$$

where k_B is Boltzmann's constant and T_{s0} is the species initial temperature. When the electron Larmor radius is equal to the electron Debye length,

$$\lambda_D = \sqrt{\frac{\varepsilon_0 k_B T_{e0}}{n_0 e^2}}, \tag{3.4}$$

we find the characteristic magnetic field strength,

$$B_0 = \sqrt{\frac{2}{3}\frac{m_e n_0}{\varepsilon_0}}, \tag{3.5}$$

where ε_0 is the vacuum permittivity and n_0 is the initial peak density. When $B = B_0$ The magnetization parameters are $\alpha_e = 5.14$ and $\alpha_i = 0.017$.

In this work, we explore a magnetic field strength regime of $B = 0 \rightarrow 0.123$ T, spanning a magnetization parameter for the electron and ions of $\alpha_i = 0 \rightarrow 0.15$ and $\alpha_e = 0 \rightarrow 45$ respectively. We measure the transverse and parallel expansion of an UNP and compare the experimental data to an ambipolar diffusion model developed by Zhang *et al.* [33]. In the non-magnetized case, we compare our data to a self similar expansion model [39, 40].

3.2 Methods

Approximately 3 million neutral Ca atoms are trapped in a MOT using 423 nm laser beams [17, 19]. The Ca^+ plasma is formed by ionizing 80% of the Ca atoms via two color resonant photoionization using 5 ns laser pulses at 423 nm and 390 nm, as shown in Fig. 3.1b. The photon energy of the 390 nm laser above the ionization limit controls the electron temperature, T_e. In this work, $T_e = 96$ K. This ensures there is no significant three-body recombination. The density and size of the plasma is obtained using resonant absorption imaging of the neutral atom cloud, scaled using the ionization fraction and the ratio of the neutral atom cloud size and the initial plasma size. In this work, the initial plasma size and density is $\sigma_0 = 400 \pm 20$ μm and $n_0 = 3.4 \pm 0.2 \times 10^{15}$ m^{-3} respectively.

A constant, uniform magnetic field is made using Helmholtz coils separated by 11 mm within the vacuum chamber. The coils are wrapped onto a stainless steel spool that is mounted to an internal imaging optical system, as shown in Fig. 3.2a. The spool is cut to eliminate eddy currents when the magnetic field changes. The stainless steel housing is grounded to suppress any electric fields arising from the potential difference between the coils. Currents ranging up to 150 A are supplied to the coils to produce magnetic field strengths up to 0.2 T. The current turns on 500 μs prior to ionization to allow the magnetic field to approach a steady state value. During this time, the

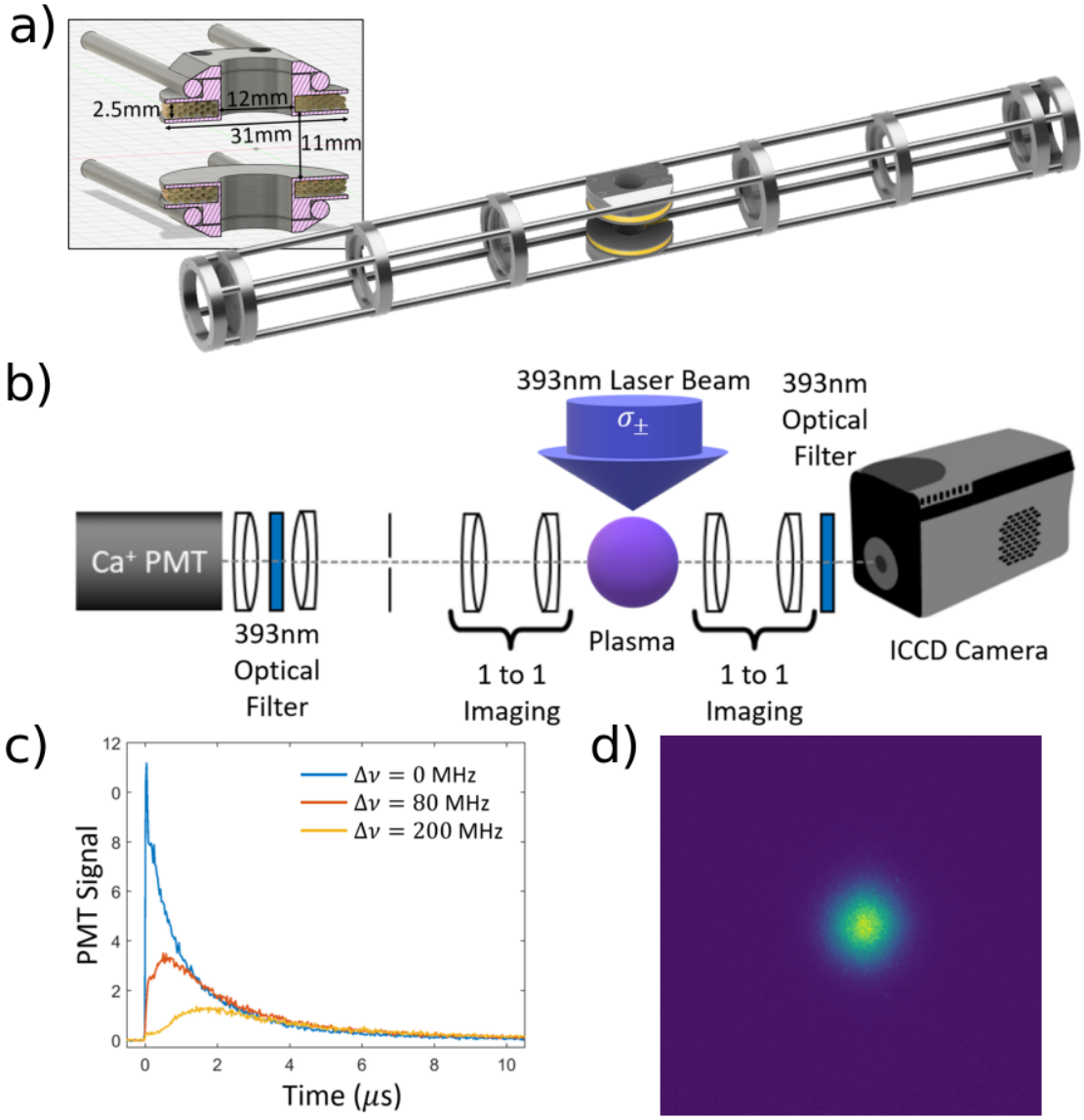

Figure 3.2 Magnetic field construction and techniques used for data collection. a) Shows the dimension of the magnetic field coil housing and how it is implemented into our optical system inside the vacuum chamber. 19 turns are achieved in the top and bottom coils. The coils are centered with the trapping center. b) The fluorescence from the plasma is detected using an optically filtered PMT and ICCD camera. c) Typical signal received from PMT, used to extract the magnetic field strength. d) Typical signal from ICCD camera, provides spatial resolution of the plasma at a specific time.

MOT laser beams and MOT magnetic field are turned off and the neutral atom cloud freely expands. The neutral atom cloud expansion is not influenced by the applied magnetic field. This expansion gives time for density variations in the atomic cloud to dissipate, providing a smooth Gaussian profile at the time of photoionization. Once the atoms are ionized, the magnetic field remains on for ≈ 50 μs before turning off. This is repeated at a rate of 10 Hz as shown in Fig. 3.1c.

The Ca^+ plasma is observed using laser-induced fluorescence. The entire plasma is illuminated by a 393 nm circularly-polarized probe laser beam. The probe laser beam propagates parallel to the magnetic field direction. The RMS width of the probe laser beam is 1620 ± 90 μm. Circularly polarized light state selectively drives the Zeeman split $^2S_{1/2} \rightarrow {}^2P_{3/2}$ transitions. The fluorescence from the plasma is imaged onto a 393 nm optically filtered ICCD Camera and PMT using a 1:1 imaging system, as shown in Fig. 3.2b. The plasma fluorescence is measured at 11 different probe laser frequency detunings relative to the atomic transition, ranging from $\pm$200 MHz from resonance in 40 MHz steps.

The Zeeman splitting of the energy levels in this work are well within the linear regime for the applied magnetic fields. The energy splitting can be calculated as,

$$\Delta E = \mu_B g_L m_j B \tag{3.6}$$

where μ_B is the Bohr magneton, g is the Landé-g_L factor [101–103] and m_j is the magnetic angular momentum quantum number.

The introduction of a magnetic field complicates the atomic spectroscopy and requires additional considerations when measuring the plasma size and expansion rates. The Zeeman splitting of the excited and ground states of Ca^+ opens a pathway to an aggressive optically dark ground-state. To eliminate the dark ground state, circularly polarized light is used to drive the nearly closed $^2S_{1/2}(m_j = \pm 1/2) \rightarrow {}^2P_{3/2}(m_j = \pm 3/2)$ transitions. In our measurements we use either σ^+ or σ^- light, depending on convenience for locking to the frequency comb. Even with this optical cycling, there is a small probability that ions in the $^2P_{3/2}(m_j = \pm 3/2)$ will fall into optically dark D

states. In previous work, these dark states where optically pumped back into the excited states to allow for long measurement times [1, 19]. With a magnetic field this no longer becomes feasible because the two previously available dark states, $^2D_{5/2}$ and $^2D_{3/2}$, split into 5, after selection rule considerations, as shown in Fig. 3.1a. To avoid this, the probe laser is turned on at some time Δt after plasma formation and observed by the ICCD camera for 100-200 ns, as shown in Fig. 3.1c.

3.3 Analysis

In this work, the plasma fluorescence is collected using both an ICCD camera and a PMT. The PMT collects spatially averaged resolved fluorescence as a function of time, while the ICCD camera collects spatially resolved measurements at a specific time. The magnitude of the magnetic field is determined using spectroscopy. We measure the frequency of $^2S_{1/2}(m_j = 1/2) \rightarrow ^2P_{3/2}(m_j = 3/2)$ transition with and without the magnetic field. The difference is directly proportional to the field strength B. Referring to Fig. 3.1a, the frequency difference can be written as $\Delta E(B) = \pm 14.00$ GHz/T $\times B$.

Camera images are taken at 11 laser frequency as described above at times $t = 0.1$, 1, 2, 5, 10, 20 μs for each magnetic field strength. These images are used to extract expansion of the plasma transverse and parallel to the magnetic field, as shown in Fig. 3.3 and 3.4. From this data the expansion velocity and expansion rate are also determined, as shown in Fig. 3.5 and 3.6 respectively. The expansion rate in previous work has proved to be a useful parameter for quantifying flow locking of binary ionic mixtures [17]. In this work, it is used to further validate the self similar expansion model and provide insight into possible heating of the electrons parallel to the magnetic field, as shown in Fig. 3.5c.

The size of the plasma in the y-direction is determined by integrating the fluorescence images over all laser detunings [see panels a) and d) in Figs. 3.3 and 3.4] and then integrating along the

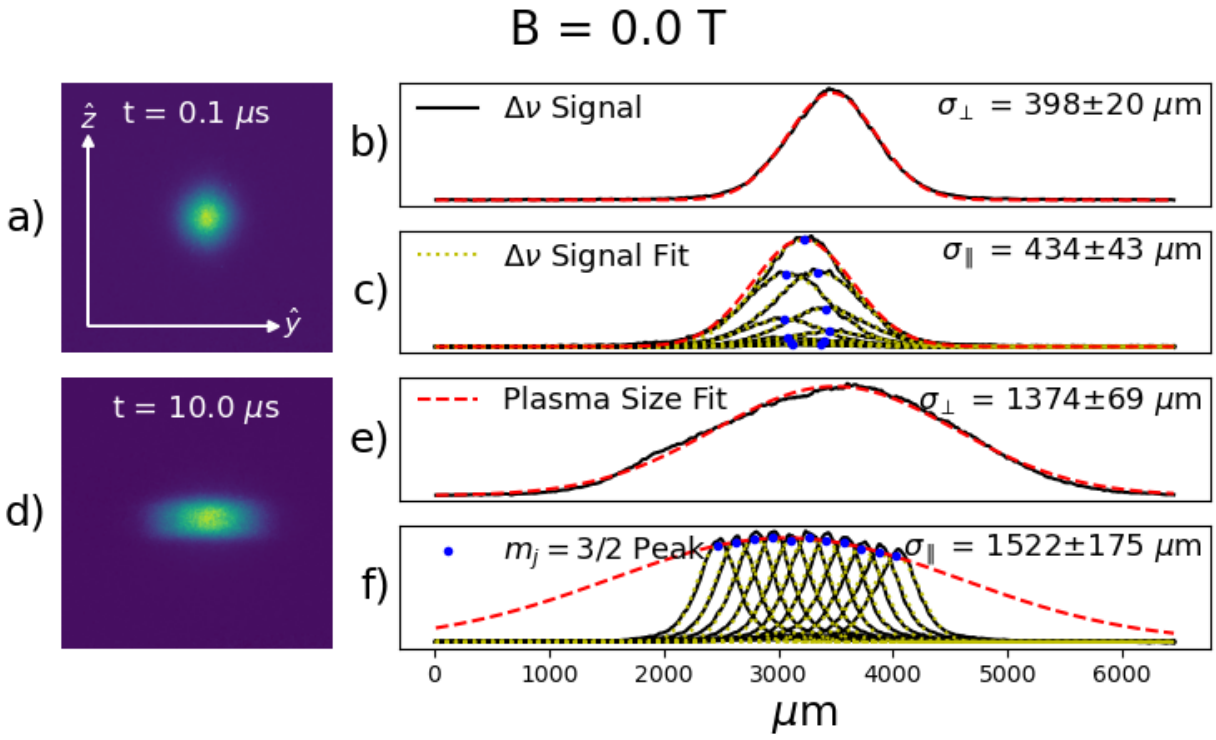

Figure 3.3 Data analysis with no magnetic field. a),d) Sum of camera images at all laser frequency detunings at times $t = 0.1$ μs and $t = 10$ μs after ionization. b),e) Horizontal projection of figure a) and d) fit to a Gaussian to extract plasma size. c),f) Vertical projection of each laser detuning image. At early times the signal is summed up and fit to a Gaussian while at later times the peak is extracted at each laser detuning and then the peaks are fit to a Gaussian to extract plasma size parallel to the magnetic field.

z-direction. The resulting density profile is shown in panel b) of Figs. 3.3 and 3.4. Fitting these profiles to a Gaussian function gives $\sigma_\perp(t)$. The probe laser propagates parallel to the magnetic field axis, the z-axis. The fluorescence from transitions between all allowed Zeeman levels results in the same plasma width. The widths are corrected slightly by taking into account the fluorescing laser beam profile.

The analysis for plasma expansion parallel to the magnetic field is more involved. For moderate values of the magnetic field, the Zeeman splitting is comparable to or less than the Doppler width of the atomic transition. For higher values of the magnetic field, the Zeeman splitting exceeds

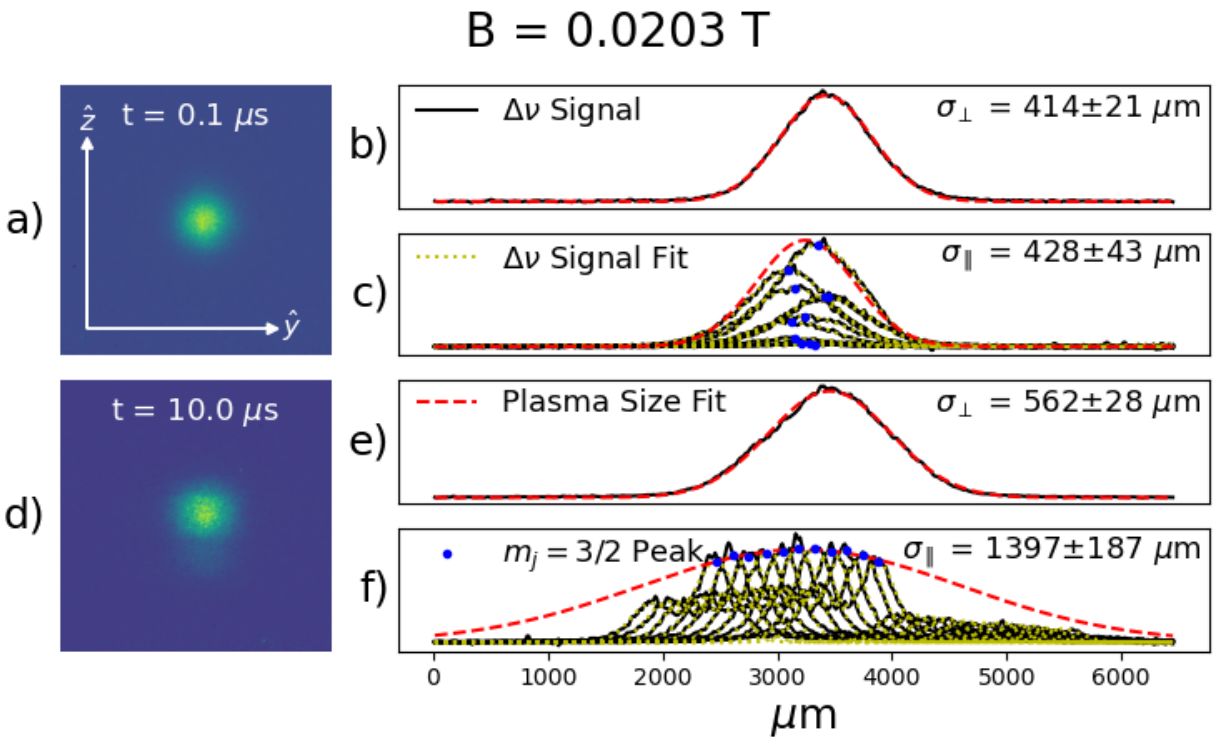

Figure 3.4 Data analysis with $B = 0.0203$ T. a),d) Sum of camera images at all laser frequency detunings at times $t = 0.1$ μs and $t = 10$ μs after ionization. b),e) Horizontal projection of figure a) and d) fit to a Gaussian to extract plasma size. Clear suppression is observed when comparing against Fig. 3.3. c),f) Vertical projection of each laser detuning image. At early times the signal is summed up and fit to a Gaussian while at later times the peak is extracted by fitting to a 3 Gaussian profile to account for other transitions at each laser detuning and then the $m_j = \pm 3/2$ peaks are fit to a Gaussian to extract plasma size. No observed change in parallel expansion when comparing against Fig. 3.3

our laser scanning range. This is why the plasma fluorescence signals in Figs. 3.3d) and 3.4d) are somewhat rectangular. Ions located above and below the observed fluorescence region have a projected velocity, v_z, outside the scanning range of the probe laser beam and therefore are invisible.

To obtain $\sigma_{\|}$, each fluorescence image is summed in the y-direction and fit to a line profile consisting of a sum of three Gaussian functions. This accounts for fluorescence from ${}^2S_{1/2}(m_j = \pm 1/2) \rightarrow {}^2P_{3/2}(m_j = \pm 3/2)$, ${}^2S_{1/2}(m_j = \mp 1/2) \rightarrow {}^2P_{3/2}(m_j = \pm 1/2)$ and ${}^2S_{1/2}(m_j = \mp 1/2) \rightarrow {}^2P_{3/2}(m_j = \mp 3/2)$ transitions. The last transition is visible because the laser beam polarization is not purely circular. Other Zeeman transitions may be present in the signal, but their contributions are negligible.

From the three Gaussian fit, the ${}^2S_{1/2}(m_j = \pm 1/2) \rightarrow {}^2P_{3/2}(m_j = \pm 3/2)$ peak location and amplitude is extracted, as shown in Figs. 3.3f) and 3.4f). The peaks location and fitted peak amplitude at each laser detuning are then fit to a single Gaussian envelope to extract the plasma size parallel to the magnetic field, $\sigma_{\|}$, as shown in Figs. 3.3f) and 3.4f).

The spatial location of the $m_j = 3/2$ peaks, as shown in Fig. 3.4f), are then used to calculate the expansion rate parallel to the magnetic field. For a given value of the magnetic field, Doppler shift maps the spatial location of the transition frequency, as measured using the camera, onto an ion velocity. Multiplying the laser frequency detuning from resonance by the wavelength of light, 393 nm, gives the velocity of the ions parallel to the laser propagation. When comparing fluorescence images from two different probe laser frequencies, the product of the laser wavelength and the frequency difference divided by the spatial shift between images gives

$$du_z/dz = \lambda \Delta \nu / \Delta z \tag{3.7}$$

where u_z is the hydrodynamic flow velocity. This can be compared to the self similar expansion model for the expansion rate, as seen in Fig. 3.5. The expansion rate with no magnetic field is given

by the spatial derivative of the flow velocity,

$$\frac{d}{dz}u_z(z,t) = \frac{t}{\tau}(1+t^2/\tau^2), \tag{3.8}$$

where flow velocity is given by the convective derivative of the plasma size evolution from the self similar expansion model [39, 40],

$$\sigma^2(t) = \sigma_0^2(1+t^2/\tau^2), \tag{3.9}$$

where τ is the characteristic expansion time [40].

$$\tau^2 = \frac{m_i\sigma_0^2}{k_B(T_{e0}+T_{i0})}, \tag{3.10}$$

and T_{i0} is the initial ion temperature. It is shown in Fig. 3.5a and 3.5b, that with no magnetic field our Ca^+ UNP follows the self similar expansion model in both the transverse and parallel direction. Once a magnetic field is applied to the system, the symmetry assumed in deriving the above solutions is no longer valid. A new treatment is required. We compare our results with an ambipolar diffusion model and the self similar expansion model, as given in sections 3.4 and 3.5 respectively.

3.4 Ambipolar Diffusion Model

In the work by Zhang *et al.* [33] an ambipolar diffusion model is used to model transverse plasma expansion in the presence of a weak magnetic field, up to 70 Gauss (0.007 T). The diffusion equation in the presence of a uniform magnetic field in 1D-cylindrical coordinates is given by

$$\frac{\partial n}{\partial t} = \frac{1}{r}\frac{\partial}{\partial r}rD_\perp\frac{\partial n}{\partial r} - F_{\text{loss}}(n,t), \tag{3.11}$$

where n is the density profile of the plasma. In this work, a similar model is used with an improved diffusion coefficient and compared with transverse plasma expansion in the presence of a strong

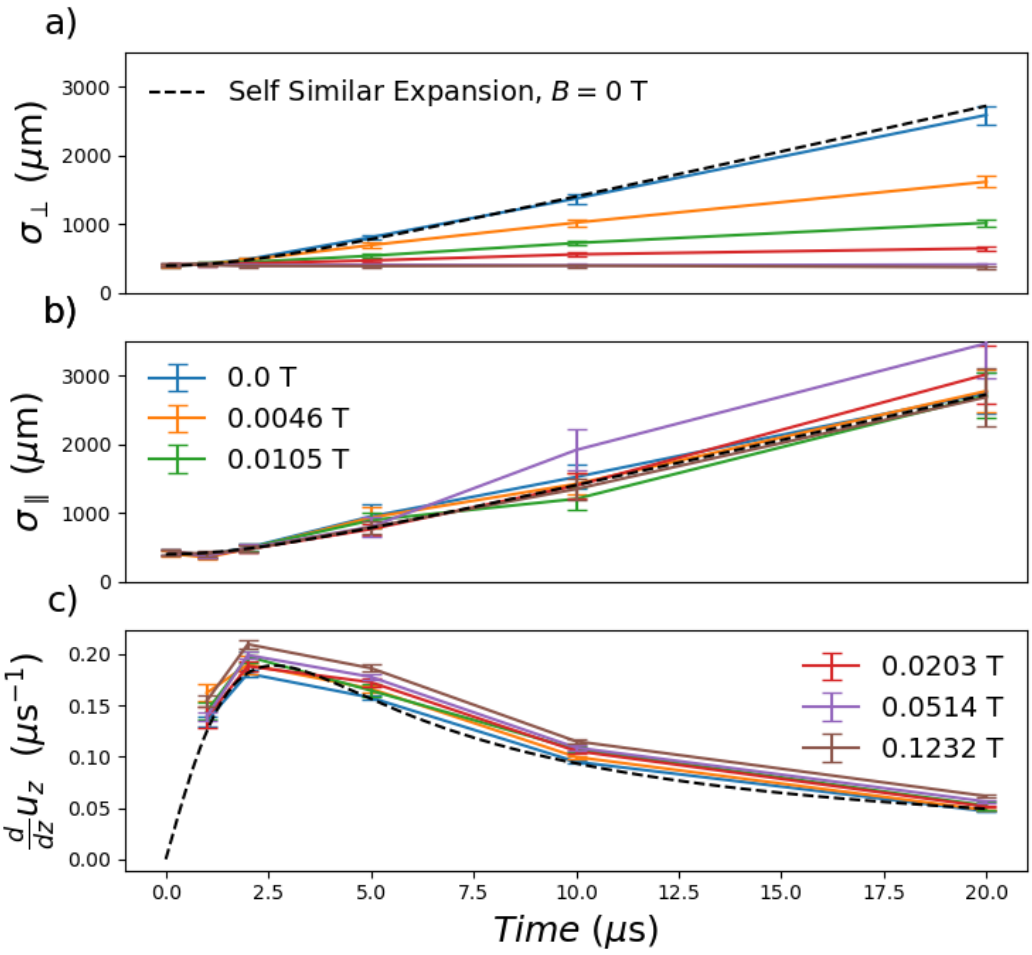

Figure 3.5 Comparing self similar expansion to experimental data. a),b) Transverse and parallel RMS size of the plasma as a function of time at various magnetic field strengths respectively. The dashed black line is comparing the known self similar expansion model to the $B = 0$ magnetic field plasma expansion (blue). c) The parallel flow velocity expansion rate as a function of time at various magnetic field strengths. The data is compared to the self similar expansion model prediction for $B = 0$.

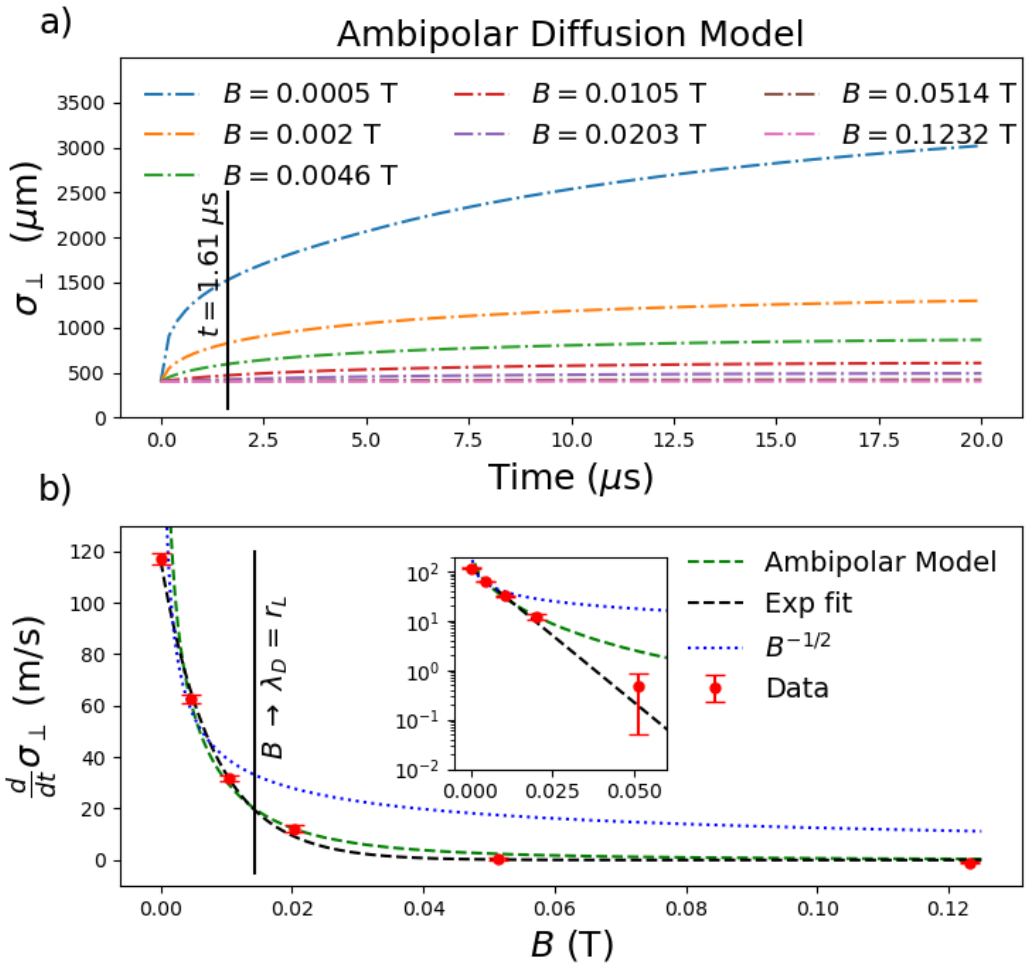

Figure 3.6 Comparing models to experimental data. a) Ambipolar diffusion model prediction for transverse RMS size of the plasma as a function of time at various magnetic field strengths. The derivative as a function of magnetic field strength is highly dependent upon the time at which you apply the derivative. The solid vertical line illustrate the time at which the derivative is the best fit to the experimental data. b) The asymptotic expansion velocity as a function of magnetic field strength. The vertical line is the value of the magnetic field when the Debye length is equal to the Larmor radius. The result are compared to ambipolar diffusion (dashed green) evaluated at $t = 1.61$ μs, $B^{-1/2}$ fit (blue dotted) and an exponential fit (black dashed) where we find that the fit parameters are equivalent to $\frac{d\sigma_\perp}{dt} = \frac{\sigma_0}{\tau} e^{-2B/B_0}$. The agreement between the ambipolar diffusion model and the experimental data is purely coincidental.

uniform magnetic field, up to 0.123 T. The diffusion coefficient perpendicular to the magnetic field is given by [104]

$$D_{\perp} = D_0 \frac{\nu_{ei}^2}{\nu_{ei}^2 + \Omega_{ce}^2}, \tag{3.12}$$

where $D_0 = k_B T_e / m_e \nu_{ei}$ is the diffusion coefficient with no magnetic field and ν_{ei} is the electron-ion collision frequency [38]. Notice that in the limit $\Omega_{ce} \gg \nu_{ei}$ then we get exactly the diffusion coefficient of Zhang *et al*.

The loss term $F_{\text{loss}}(n,t)$, in Eq. (3.11) accounts for density losses due to expansion parallel to the magnetic field. As shown in Fig. 3.5b, the expansion parallel to the magnetic field is unaffected and follows the known self similar expansion model [39, 40]. The loss term is then appropriately chosen to follow the self similar expansion model for no magnetic field,

$$F_{\text{loss}}(n,t) = n \frac{t}{\tau^2 (1 + t^2/\tau^2)}. \tag{3.13}$$

We solve Eq. (3.11). numerically. The equation is discretized in space using a second order centered finite difference method, which is numerically integrated using the method of lines [105] with the implicit Runge-Kutta (Radau) method.

The numerical solutions of $n(r,t)$ are fit to a Gaussian profile to yield the rms plasma width as a function of time, $\sigma_{\perp}(t)$, as shown in Fig. 3.6a. It is clear that the ambipolar diffusion model predicts functions $\sigma_{\perp}(t)$ that are inconsistent with the experimental data for all values of the magnetic field [Fig. 3.5a)].

The time derivative of predicted value $\sigma_{\perp}(t)$ from the ambipolar diffusion model is compared to experimental results in Fig. 3.6b), where we use the experimental data of Fig. 3.5a). Because the predicted value of $\sigma_{\perp}(t)$ depends on time, the derivative must be evaluated at a specific time. We note that there is no *apriori* "best choice" for such a time. The best fit to the data was found by evaluating the derivative at $t = 1.61$ μs. Choosing a different time would result in a model prediction that deviates significantly from the experimental results. The match of $d\sigma_{\perp}(t)/dt$ to the experimental data at $t = 1.61$ μs therefore appears to be accidental and not physical.

3.5 Self Similar Plasma Expansion Model

Mora developed a self similar model for plasma expansion into a vacuum [39, 106]. In this model he assumes self similar expansion, quasinuetrality and spatial temperature invariance. Here we apply his work to our UNP.

Starting with the equation of motion for species, s we get

$$\frac{\partial \mathbf{u}_s(\mathbf{r},t)}{\partial t} = -\mathbf{u}_s(\mathbf{r},t)\cdot\nabla\mathbf{u}_s(\mathbf{r},t) - \frac{k_B T_s}{m_s}\frac{1}{n_s}\nabla n_s(\mathbf{r},t) + \frac{q_s}{m_s}\left[\mathbf{E}(\mathbf{r},t)+\mathbf{u}_s(\mathbf{r},t)\times\mathbf{B}\right] \tag{3.14}$$

where $\mathbf{u}_s$ is the flow velocity and $\mathbf{E}$ is the electric field.

Considering the case of no magnetic field, we neglect the ion pressure term, as it is much smaller than the electric field term. The equations of motion for the electrons and ions then become

$$\frac{\partial u_i}{\partial t} + u_i\frac{\partial u_i}{\partial r} = -\frac{e}{m_i}\frac{\partial \Phi}{\partial r} \tag{3.15}$$

$$\frac{\partial u_e}{\partial t} + u_e\frac{\partial u_e}{\partial r} = \frac{e}{m_e}\frac{\partial \Phi}{\partial r} - \frac{k_B}{m_e n_e}\frac{\partial}{\partial r}(n_e T_e) \tag{3.16}$$

where we have rewritten $\mathbf{E} = -\nabla\Phi$ in terms of the potential Φ.

In the self similar plasma expansion model we assume quasineutrality, $n_e = n_i$, $u_e = u_i$ and a self similar expansion,

$$n(x,t) = n_0\frac{\sigma_0}{\sigma(t)}e^{\frac{-r^2}{2\sigma(t)^2}}, \tag{3.17}$$

applying the above assumption, the adiabatic equation of state and plugging Eq. (3.17) into Eq. 3.15 and 3.16 one recovers Eq. (3.9) and 3.10, with the exception that $T_{i0} = 0$. This is compared to our experimental data in both the parallel and transverse direction, as seen in Fig. 3.5a and 3.5b. We see that the self similar expansion model is an exact solution to UNP expansion in the case of no magnetic field, while the diffusion model fails.

Note that the governing dynamics in the diffusion model is governed by collisions, while the self similar expansion model has no collisions. suggesting that the expansion is a collisionless expansion.

In the case of large magnetic field the equations of motion, in cylindrical coordinates, for the electrons become

$$\frac{\partial u_{r,e}}{\partial t}+u_{r,e}\frac{\partial u_{r,e}}{\partial r}-\frac{u_{\theta,e}^2}{r} = -\frac{k_B T_e}{m_e}\frac{1}{n_e}\frac{\partial n_e}{\partial r}+\frac{e}{m_e}\frac{\partial \Phi}{\partial r}-\omega_{ce}u_{\theta,e}+n_e\nu_{ei}\left(u_{r,i}-u_{r,e}\right), \quad (3.18)$$

$$\frac{\partial u_{\theta,e}}{\partial t}+u_{r,e}\frac{\partial u_{\theta,e}}{\partial r}+\frac{u_{\theta,e}u_{r,e}}{r} = \omega_{ce}u_{r,e}+n_e\nu_{ei}\left(u_{\theta,i}-u_{\theta,e}\right), \quad (3.19)$$

$$\frac{\partial u_{z,e}}{\partial t}+u_{z,e}\frac{\partial u_{z,e}}{\partial z} = -\frac{k_B T_e}{m_e}\frac{1}{n_e}\frac{\partial n_e}{\partial z}+\frac{e}{m_e}\frac{\partial \Phi}{\partial z}, \quad (3.20)$$

and for the ions

$$\frac{\partial u_{r,i}}{\partial t}+u_{r,i}\frac{\partial u_{r,i}}{\partial r}-\frac{u_{\theta,i}^2}{r} = -\frac{k_B T_i}{m_i}\frac{1}{n_i}\frac{\partial n_i}{\partial r}-\frac{e}{m_i}\frac{\partial \Phi}{\partial r}+n_i\nu_{ie}\left(u_{r,e}-u_{r,i}\right), \quad (3.21)$$

$$\frac{\partial u_{\theta,i}}{\partial t}+u_{r,i}\frac{\partial u_{\theta,i}}{\partial r}+\frac{u_{\theta,i}u_{r,i}}{r} = n_i\nu_{ie}\left(u_{\theta,e}-u_{\theta,i}\right), \quad (3.22)$$

$$\frac{\partial u_{z,i}}{\partial t}+u_{z,i}\frac{\partial u_{z,i}}{\partial z} = -\frac{e}{m_i}\frac{\partial \Phi}{\partial z}. \quad (3.23)$$

These equations are augmented by continuity equations for each species and the Poisson equation.

In the above equations we have assumed that there is no angular dependence in each component of the flow velocities, *i.e.* $u_{\alpha,s}(r,\theta,z,t)=u_{\alpha,s}(r,z,t)$ where $\alpha=r,\theta,z$, and no z dependence for the perpendicular components, *i.e.* $u_{\theta,s}(r,z,t)=u_{\theta,s}(r,t)$, $u_{r,s}(r,z,t)=u_{r,s}(r,t)$, as indicated by the cylindrical symmetry of the problem. Furthermore, we assume the absence of collisions in the $\hat{z}$ direction and no radial dependence of the $\hat{z}$ velocity component, *i.e.* $u_{z,s}(r,z,t)=u_{z,s}(z,t)$. This leads to a collisionless model in the $\hat{z}$ direction.

However, we note that in the presence of a magnetic field, the ion pressure term and e-i collisions in the plane perpendicular to **B** cannot be ignored due to the small Larmor radius of the electrons. This electron radial confinement reduces the strength of the electric field in the radial direction, thus the ion pressure term is no longer negligible compared to the electric field.

3.6 Discussion

We have developed a new method for measuring UNP expansion in a strong, uniform magnetic field. High precision laser spectroscopy and optically filtered fluorescent imaging allow for direct measurements of UNP size, temperature and magnetic field strength.

The plasma expansion parallel to the magnetic field is found to be unaffected by the strong uniform magnetic field and follows the self similar plasma expansion model exactly. Perpendicular to the magnetic field, we can control the expansion velocity by varying the magnetic field strength.

In the classical diffusion problem, the known solution for radial expansion goes as $\sqrt{t}$. This relationship can be softened by including non-linear effect, as we have done above, but it can not be corrected to the extent of predicting ballistic expansion. In the known self similar expansion model [39, 40] the plasma expansion becomes ballistic in nature. This can be seen explicitly in Fig. 3.5a and Eq. (3.9). This ballistic expansion is observed experimentally for both the magnetized and non-magnetized cases.

In the case of zero magnetic field, the self similar expansion model [39, 40] is in perfect agreement to our experimental data. We also find that in the presence of a magnetic field, the expansion parallel to the field follows the self similar expansion model. Unfortunately, there is no extension of this model to account for magnetic fields. Possible extensions of this model could be applied to provide a more accurate representation of perpendicular plasma expansion in a uniform magnetic field.

We compare our data with an ambipolar diffusion model [33] and find that it fails to describe the expansion evolution of the plasma even when an exact solution is known. We therefore considered an alternate model that predicts an exponential relation between expansion velocity and magnetic field strength. The inset of Fig. 3.6, which is log-linear, reveals the superior performance of the exponential model. We note that the exponential decay scale is very closely given by B_0, defined in

Eq. (3.5); thus, we find that

$$\frac{d\sigma_{\perp}}{dt} = \frac{\sigma_0}{\tau} e^{-2\frac{B}{B_0}}. \tag{3.24}$$

Because of the limitations of our dataset, this relationship could be a coincidence: future experiments should verify the result for different plasma densities.

The experimental methods used in this work allow for measuring magnetized transport properties within an UNP, such as thermal conductivity, diffusion, disorder induced heating suppression and temperature relaxation.

3.7 Acknowledgments

We would like to thank Dr. Ross Spencer for useful conversation. R.T.S. and S.D.B. acknowledge support from the U.S. Air Force Office of Scientific Research Grant No. FA9550-17-1-0302 and the National Science Foundation Grant No. PHY-2009999. M.S.M. and L.G.S. were supported by the U.S. Air Force Office of Scientific Research Grant No. FA9550-17-1-0394.

Chapter 4

Methods

4.1 Introduction

The purpose of this chapter is to provide more information on techniques, process's and general information used in this work.

4.2 Laser Induced Fluorescence

Ca and Yb are both alkali-earth elements, which means that both have two valence electrons. When the atom is ionized, one electron is ejected from the atom, leaving an ion with a single valence electron. The remaining valence electron in the ions makes them particularly interesting for studying transport properties. The remaining valence electron can be excited for observing the ions using laser induced fluorescence, providing the possibility to get both spatial and time resolved measurements.

Fluorescence comes from the spontaneous emission of a photon from the decay of an electron to a lower energy level. When the electron is excited into the excited state using a resonant laser beam, then it is called laser induced fluorescence. The energy required to excite the electron into an

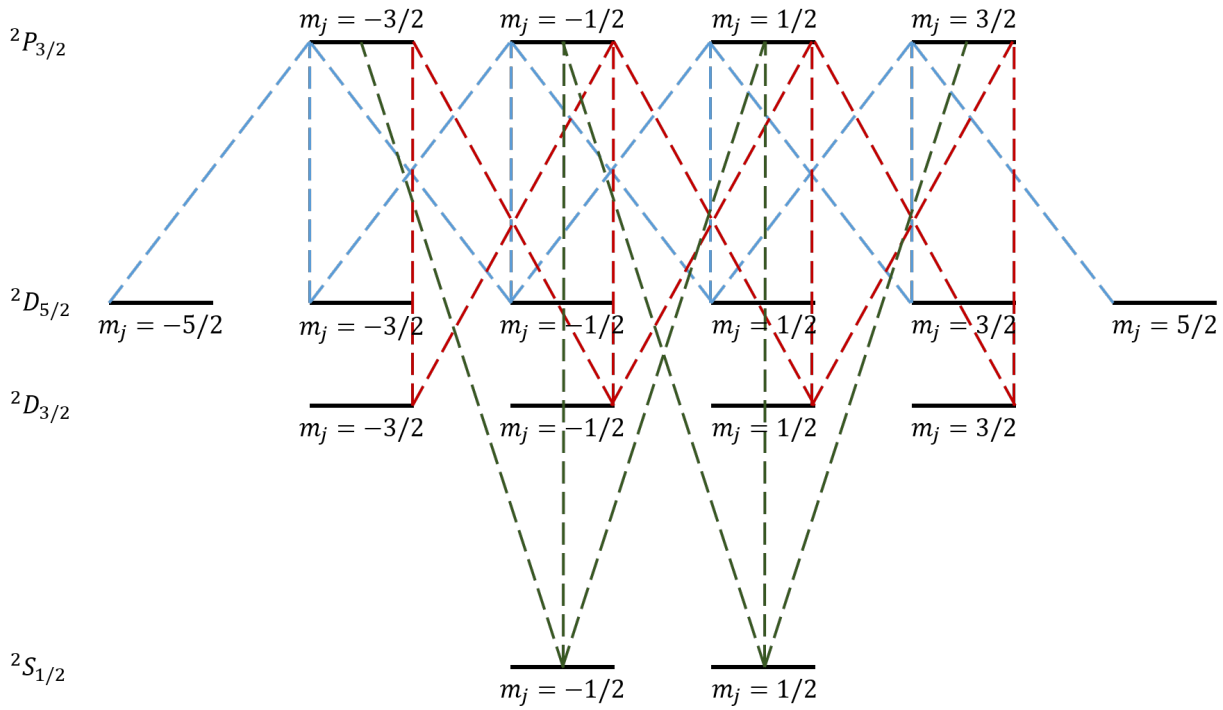

Figure 4.1 This diagram illustrates the allowed transitions. The green dashed lines show the allowed excitation and decay between the $^2S_{1/2}$ and $^2P_{3/2}$ states. The red dashed lines show the allowed decay from the $^2P_{3/2}$ state to the $^2D_{3/2}$ state. The blue dashed lines show the allowed decay from the $^2P_{3/2}$ state to the $^2D_{5/2}$ state.

excited state is equal to the energy difference between the initial state (usually the ground state) and the excited state. When the energy of the photons in the laser beam equals the excitation energy of the electron, then the laser frequency is in resonance with the atomic transition.

The electron absorbs a resonant photon from the laser beam and is excited into an excited state. When the laser beam is applied to an atomic cloud, then each atom will absorb a photon and the electron will then spontaneously decay back into the ground state. The photons that are emitted radiate in a dipole radiation pattern.

The fluorescence from neutral atoms is created by driving the $^1S_0 \rightarrow {}^1P_1$ transition using a laser at 423 nm for Ca and 399 nm for Yb. The Ca^+ ions are fluoresced by driving the $^2S_{1/2} \rightarrow {}^2P_{3/2}$

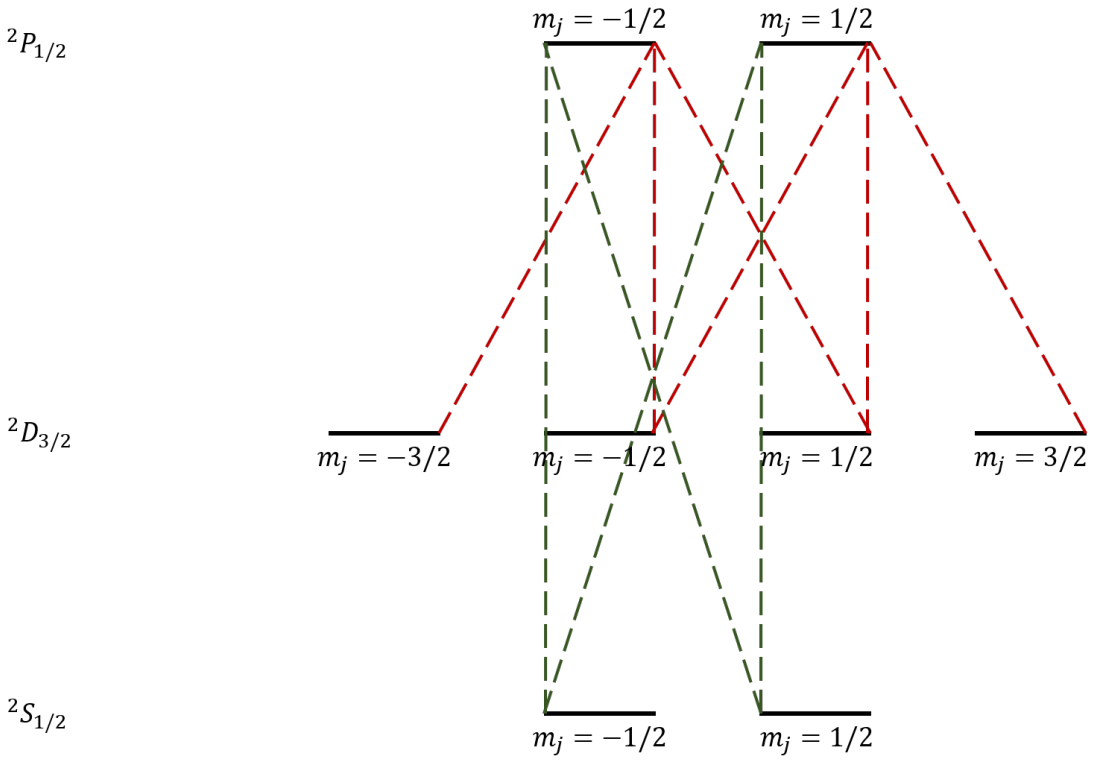

Figure 4.2 This diagram illustrates the allowed transitions. The green dashed lines show the allowed excitation and decay between the $^2S_{1/2}$ and $^2P_{1/2}$ states. The red dashed lines show the allowed decay from the $^2P_{1/2}$ state to the $^2D_{3/2}$ state. In this case, the $^2D_{5/2}$ state is not an allowed transition because of the $\Delta l = \pm 1$ selection rule.

transition using a laser at 393 nm. Likewise, for Yb^+ ions, a 369 nm laser is used to drive the $^2S_{1/2} \rightarrow {}^2P_{1/2}$ transition, as seen in Fig. 2.6 and Fig. 3.1b.

In the presented work, only the fluorescence from the Ca^+ plasma is influenced by external magnetic fields, Chapter 3. When a magnetic field is applied, the energy levels become Zeeman shifted, as described in Section 4.8. The splitting is linearly dependent on the magnitude of the magnetic field. For the desired Zeeman split $^2S_{1/2}(m_j = \pm 1/2) \rightarrow {}^2P_{3/2}(m_j = \pm 3/2)$ transition, we find that the required change in laser frequency is $\Delta\nu = \pm 1.4 \times 10^4 B$ MHz/T. This transition was chosen because the Zeeman split energy level structure allows for a recycling transition.

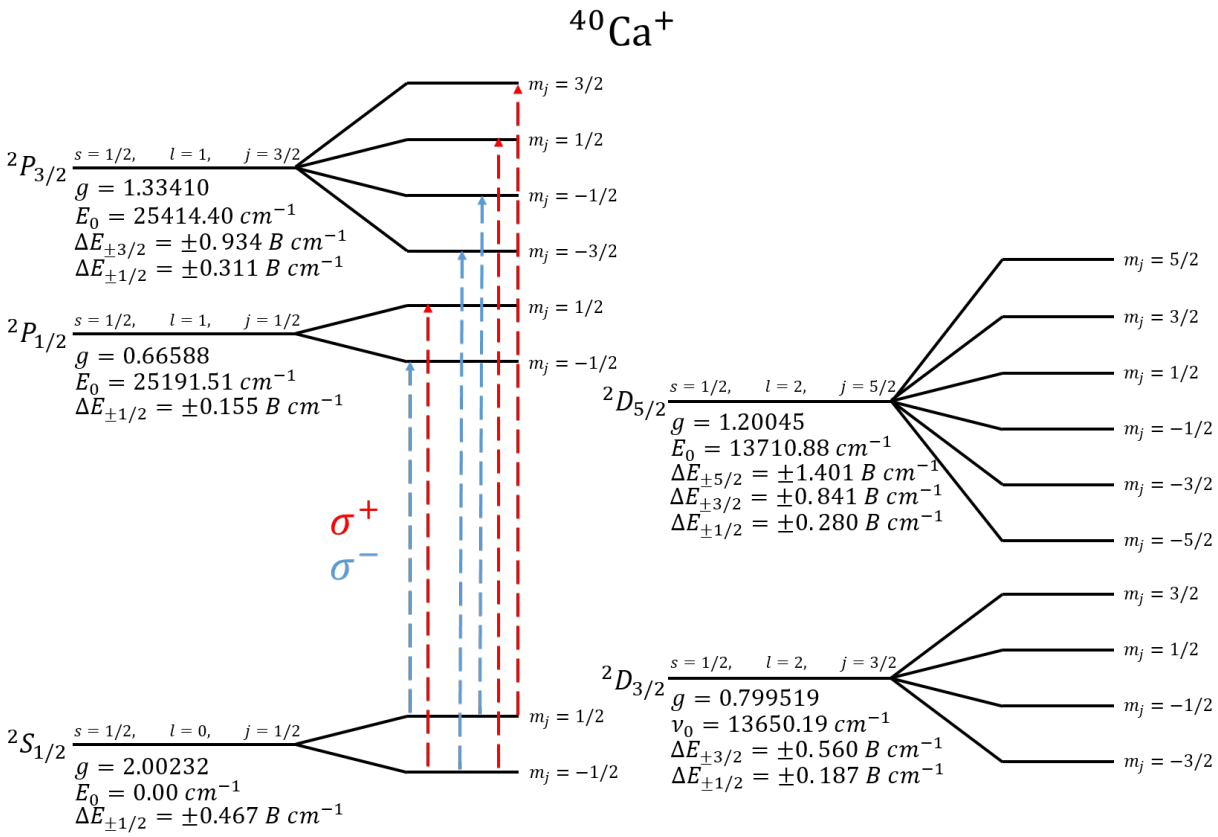

Figure 4.3 Energy level diagram for the relevant energy levels in Ca^+. The red dashed lines the allowed excitations using right-handed circular polarization. The blue dashed lines are the allowed excitations using left-handed circular polarization. The relevant allowed decay paths are illustrated in Fig. 3.1a

The allowed transitions for both the Zeeman split $^2S_{1/2} \rightarrow {}^2P_{1/2}$ and $^2S_{1/2} \rightarrow {}^2P_{3/2}$ transition are shown in Fig. 4.2 and Fig. 4.1 respectively. The allowed transitions are determined using the following selection rules

$$\Delta l = \pm 1 \tag{4.1}$$

$$\Delta m_j = 0, \pm 1 \tag{4.2}$$

$$\tag{4.3}$$

The excitation transition is restricted by introducing either right or left-handed circularly polarized light $\sigma_{\pm}$, as shown in Fig. 4.3. The selection rules associated with circular polarization become,

$$\sigma_+ \rightarrow \Delta m_j = +1 \tag{4.4}$$

$$\sigma_- \rightarrow \Delta m_j = -1 \tag{4.5}$$

It can be seen from Fig. 4.3 that by choosing the $^2S_{1/2} \rightarrow {}^2P_{1/2}$ transition, there is no way to eliminate the aggressive dark ground state. For this reason, $^2S_{1/2} \rightarrow {}^2P_{3/2}$ transition is chosen. Using circularly polarized light, we can excite the $^2S_{1/2}(m_j = \pm 1/2) \rightarrow {}^2P_{3/2}(m_j = \pm 3/2)$ transition and ensure that the excited electron falls back into the birth ground state or one of the weaker dark states. The allowed dark states transitions are shown in Fig. 3.1a. More information on dark states can be found in Section 4.7.

4.3 Magneto Optical Trap

The 1997 Nobel Prize in physics was awarded to William Phillips, Steven Chu and Claude Cohen-Tannoudji "for development of methods to cool and trap atoms with laser light" [107]. Today, this is known as a Magneto Optical Trap (MOT) [107]. Since then, MOT's have been adopted by many areas of research. A few examples include atomic physics [108], plasma physics [17] and ultracold chemistry [109]. A MOT takes advantage of state selective radiation from the Zeeman split energy

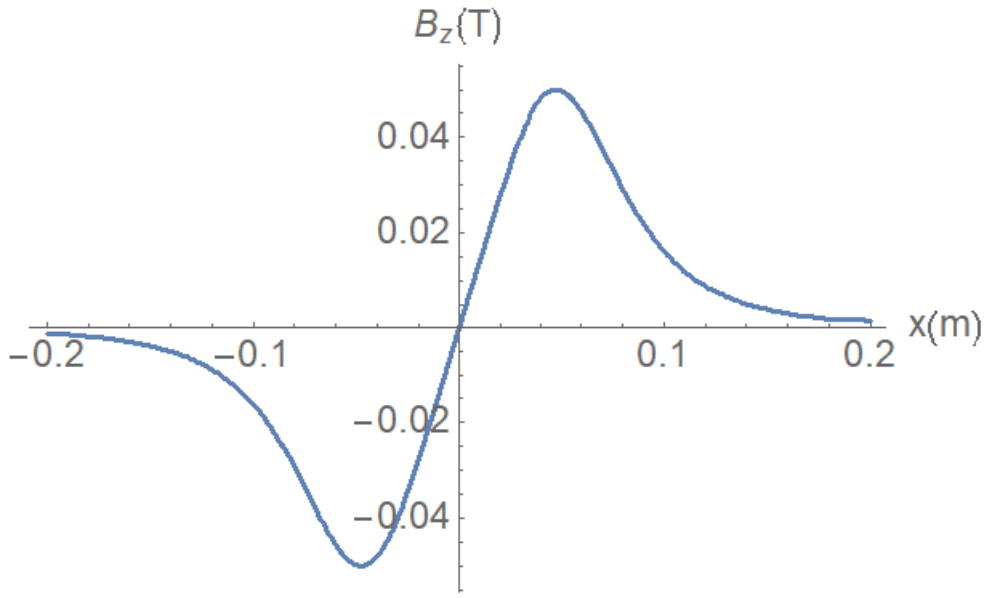

Figure 4.4 Shows the magnetic field strength, B_z, along the z axis due to the quadrupole magnetic field produced by anti-Helmholtz coils.

levels of an atom in the presence of a quadrupole magnetic field. In this work, we are able to simultaneously trap upwards of 10 million Ca and Yb neutral atoms using this technique.

A quadrupole magnetic field is realized using anti-Helmholtz coils. Anti-Helmholtz coils are a set of two counter propagating current carrying coils displaced by a distance equal to the coil radius. Using Biot-Savart's law, Eq. 4.29, the magnitude of the magnetic field along the z-axis is determined, as shown in Fig. 4.4. At the origin the magnitude of the magnetic field is zero, $B = 0$ T, and increases in both the $\hat{z}$ and $-\hat{z}$ direction.

In the limit that the displacement from the origin is small compared to the radius of the coils, the magnetic field increases linearly in the radial direction $\hat{r}$ from the trap center. In our case, the magnetic field coils are displaced by approximately 6.7 cm from center to center. A typical trapped neutral atom cloud has a rms width of 300 μm. The relatively small plasma size in comparison to the coil displacement ensures we are well within the linear regime for the radial magnetic field strength.

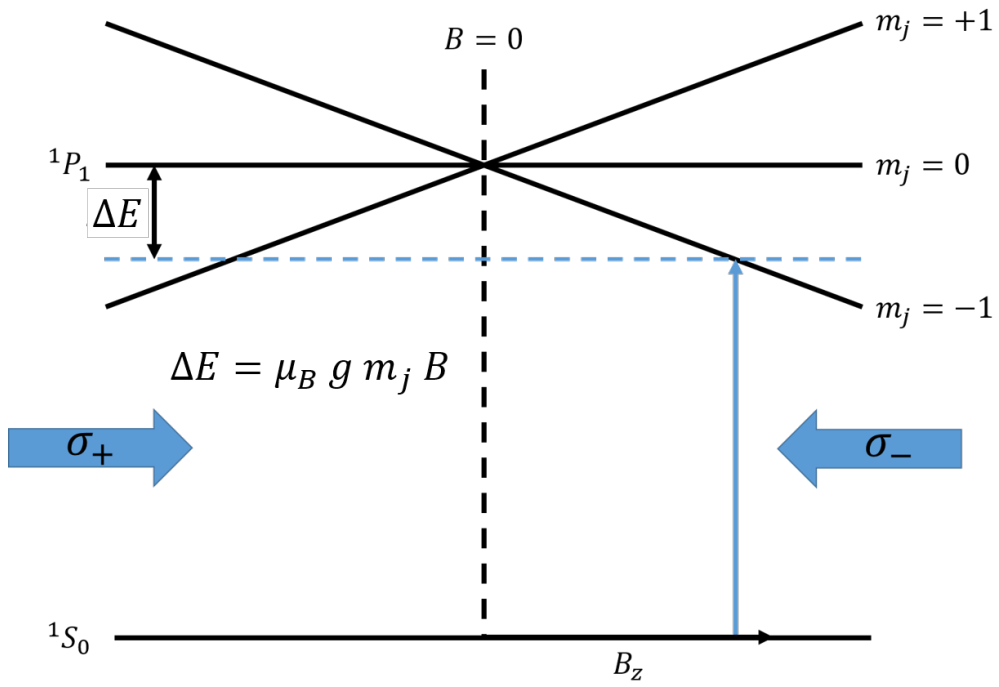

Figure 4.5 Illustrates Zeeman energy level splitting of the neutral atoms in the presence of an anti-Helmholtz magnetic field. $\Delta\nu = 54$ MHz is the laser detuning from resonance used in order to obtain state selective radiation pressure on the atoms

The anti-Helmholtz coils provide a magnetic gradient of $\Delta B = 100$ Gauss/cm in the center of our MOT. This gradient creates a Zeeman splitting in the atoms that is proportional to the displacement from the center of the trap, similar to equation 4.17,

$$\Delta E = \mu_B m_j g \Delta B r \hat{r}, \tag{4.6}$$

where ΔE is the energy splitting, m_j is the total angular momentum quantum number and g is the Lande g-factor given by equation 4.18. The Bohr magneton, $\mu_B = e\hbar/2m_e$, is given in terms of physical constants, Where e and m_e are the electron charge and mass respectively and $\hbar$ is Planck's constant. The energy splitting as a function of displacement is illustrated in Fig. 4.5.

In the case of both Ca and Yb, the transition used to trap the atoms is the ${}^1S_0 \rightarrow {}^1P_1$ transition, as shown in Fig. 2.6. The symmetry between the Ca and Yb energy levels ensure that the energy splitting is identical. The splitting of the energy levels introduces a m_j state selection rule, $\Delta m = \pm 1$.

Applying circularly polarized light in either the positive or negative sense forces the selection rule to $\sigma_+ \rightarrow \Delta m_j = +1$. The MOT using this principle in order to provide state selective radiation pressure on the atoms.

Six counter propagating laser beams with opposing circular polarization are used along the three Cartesian axes through the trap center. The laser beams are detuned from resonance by 54 MHz, allowing only the atoms at a certain distance from trap center to be in resonance with the laser beam, illustrated in Fig. 4.5. This geometric configuration of the detuned laser beams along with the quadrupole magnetic field provide state selective radiation pressure on the atoms in the -$\hat{r}$ direction.

Atoms are supplied to the MOT through an atomic beam. In order to trap the neutral atoms in the MOT, the optical forces must overcome the kinetic energy of the atoms in the atomic beam. We can think about this in terms of the recoil velocity from the photon and the thermal velocity of the atoms. Recoil velocity, which is the change in velocity of the atom due to the absorption and emission of a photon, can be found from conservation of momentum, at best $v_{recoil} = 2h/m\lambda \approx 0.05$ m/s. The atoms thermal velocity is given by $v_{th} = \sqrt{k_B T/m_i} \approx 300$ m/s. In order to rectify this discrepancy, a slowing laser beam is used to reduce the kinetic energy of the atoms prior to the atoms reaching the MOT. For more information on the atomic beam and slowing laser beam, see section 4.4.

4.4 Slower Beam and Atomic Beam

An atomic beam is used to supply atoms to the MOT. The optical forces of the MOT are not sufficient to trap the vast majority of atoms from the atomic beam. Only the slow moving atoms have a kinetic energy low enough to be trapped. The number of atoms trapped is increased by introducing a laser beam to slow down the atoms in the atomic beam prior to entering the trapping fields of the MOT. The atomic beam is supplied by heating up pure Ca and Yb ingots to 500 C and 430 C respectively [110], as shown in Fig. 4.6A). A honeycomb structure of micro tubes are

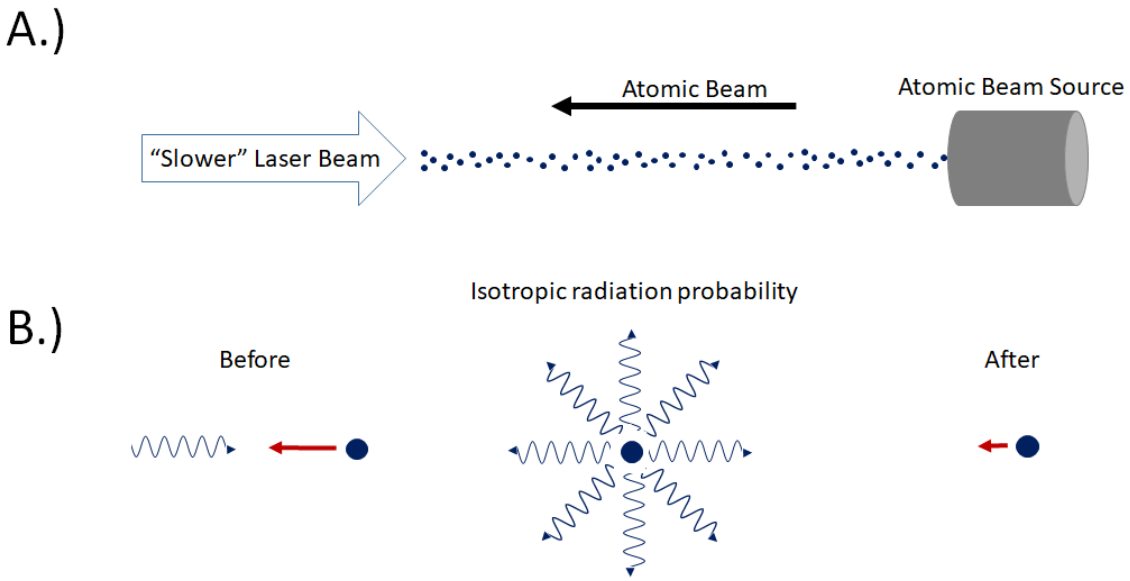

Figure 4.6 A) The atomic beam is created through collimation of the atoms so that only a directional velocity is selected. These atoms are then slowed by means of Doppler cooling. B) Illustrates the process of Doppler cooling. The atoms that are Doppler shifted above resonance will absorb photons from the slower beam. The photon can then radiate in any direction. On average, the atom will emit the photon in the opposite direction resulting in a momentum transfer that slows the atom down, as indicated by the magnitude of the red arrows.

used to preferentially select only the atoms that radiated parallel to the micro tubes. The atoms that pass though the micro tubes make up the atomic beam with a Maxwell-Boltzmann temperature distribution peaked at 500 C and 430 C for Ca and Yb respectively.

A counter propagating laser beam 250 MHz detuned from resonance is used to slow down the atoms in the atomic beam. Laser cooling takes advantage of the Doppler effect and the fringing fields of the anti-Helmholtz magnetic field.

When an atom is in motion, then the observed frequency of a photon by the atom is Doppler shifted. For this reason the slowing laser beam is detuned from resonance by 250 MHz so that higher velocity atoms are in resonance with the laser beam. When these atoms absorb a photon from the counter propagating laser beam, the spontaneously emitted photon is randomly radiated,

resulting in a slowing of the atom's velocity proportional to the photon's momentum, as seen in Fig. 4.6B). This can be quantified using conservation of momentum. In the best case scenario, where the absorbed photon and emitted photon are exactly opposite in direction then,

$$\frac{h}{\lambda} + mv_i = mv_f - \frac{h}{\lambda} \tag{4.7}$$

$$\Delta v = 2\frac{h}{m\lambda}, \tag{4.8}$$

where h is Planck's constant, m is the mass of the atom and λ is the laser wavelength.

The Doppler cooling only works until the atoms are Doppler shifted out of resonance with the laser beam. This is where the fringing magnetic field from the MOT helps to further cool the atoms. As the atoms approach the MOT, the magnetic field varies. This change is the magnetic field allows for the atoms to be Zeeman shifted into resonance with the slowing laser beam to even further cool the atoms. For more information on how Zeeman splitting works, see section 4.8. By cooling the atoms, we are able to trap upwards of 10 million atoms in the MOT at a density of 1×10^{10} cm^{-3}.

4.5 Absorption Imaging and Plasma Size

Absorption imaging uses laser induced fluorescence, as described in Section 4.2, to measure the trapped neutral atom cloud size and density. Unlike laser induced fluorescence imaging, absorption imaging measures the loss of laser light due to absorption though a medium. The absorption of light provides information about the density and size of the neutral atom cloud.

A weak laser beam on resonance illuminates the neutral atoms within the MOT. The atoms absorb the photons and emit them in a dipole radiation pattern, resulting in a reduction in the laser power in the area of the laser profile that is incident with the neutral atoms. A camera is used to observe the laser profile and quantify the size and density of the plasma. Four images are taken, the first is a background image with no neutral atom cloud or laser beam , F_{dark}. The second is an image of neutral atom cloud, F_{MOT}. Third, is the laser profile, F_{laser}m and the last image is of the

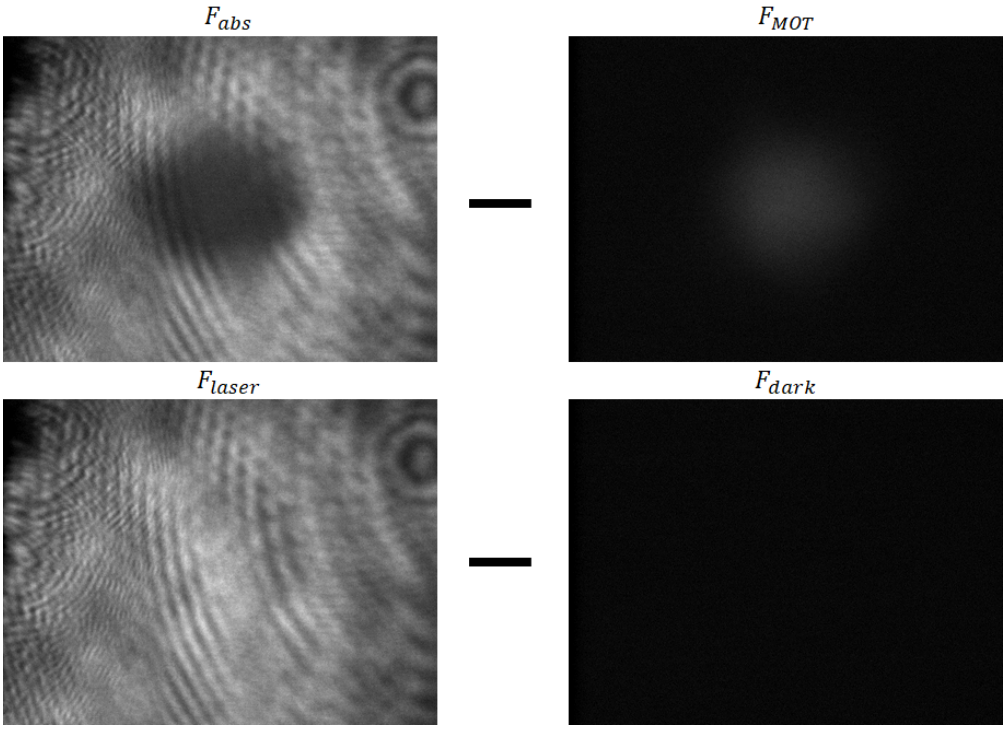

Figure 4.7 Demonstrates pictorially how the absorption measurement is taken, analogous to Eq. 4.9. Image F_{abs}: absorption of the MOT. Image F_{MOT}: fluorescence of the MOT. Image F_{laser}: laser beam profile. Image F_{dark}: background.

laser profile in the presence of the neutral atom cloud, F_{abs}. The images are then used to find the percentage of photons absorbed,

$$100\left(1-\frac{F_{abs}-F_{MOT}}{F_{laser}-F_{dark}}\right)=\text{Absorption }\%, \tag{4.9}$$

this is visualized in Fig. 4.7.

Using Beer's Law, we determine the peak density,

$$\frac{dI}{dz}=-I\sigma n \tag{4.10}$$

where I is the intensity of the laser beam, n is the density profile of the neutral atom cloud and the absorption cross-section for resonant light is $\sigma=3\lambda^2/2\pi$. Assuming a Gaussian density profile

with an rms width of r_0 and peak density n_0, we can write,

$$\ln\left(\frac{I_f}{I_0}\right) = \int -\sigma n_0 \exp\left(-z^2/2r_0^2\right) dz. \tag{4.11}$$

In this equation I_0 is the intensity of the laser beam prior to interacting with the neutral atoms and I_f is the intensity of the laser beam after interacting with the neutral atom. Solving for the peak density, n_0, we get

$$n_0 = \frac{1}{\sigma r_0 \sqrt{2\pi}} \ln\left(\frac{I_0}{I_f}\right). \tag{4.12}$$

Using r_0 as a fit parameter of the absorption image to a two-dimensional Gaussian, we find the size and density of the neutral atom cloud. A typical size and density for our trapped neutral atoms are 300 μm and 1×10^{10} cm^{-3} respectively.

If the density and/or size of the neutral atom cloud is large enough, then all photons that pass through the neutral atom cloud are absorbed. Under these circumstances, the density cannot be found using resonant absorption imaging. When this occurs, off resonance absorption imaging is required. The laser beam frequency is detuned until there is observable transmission of the laser beam through the center of the neutral atom cloud. The density is then determined using the same process as described above, but by taking into account the laser frequency detuning of the laser beam in the absorption cross-section. The absorption cross-section is then given by,

$$\sigma = \frac{3\lambda^2}{2\pi} \frac{1}{1 + (2\Delta/\Gamma)^2}, \tag{4.13}$$

where Δ is the detuning from resonance, λ is the wavelength and Γ is the natural line width, for Ca $\Gamma = 35$ MHz, and for Yb $\Gamma = 28$ MHz.

Depending upon the experiment, the initial size of the neutral atom cloud and plasma may not be the same size. In both works presented, the atomic clouds are allowed to expand for some time prior to ionization, as shown in Fig. 2.7 3.1c. At ionization, upwards of 100% of Ca and 70% of Yb atoms are ionized. Because of this, the density determined by absorption imaging is not the same as the plasma density.

The plasma density is found by measuring the ionization fraction of the neutral atom cloud. An optically filtered PMT and is used to measure the fluorescence from the neutral atom cloud through the ionization process. The ionization fraction, IF, is given by

$$IF = \frac{S_f - S_{Bk}}{S_i - S_{Bk}}, \tag{4.14}$$

Where S_f is the fluorescence signal of the neutral atoms after ionization. S_i is the fluorescence signal prior to ionization, and S_{Bk} is the background signal with no neutral atoms present. In the case of no neutral atom expansion, the plasma density is found by multiplying the ionization fraction to the neutral atom cloud density, which has been previously determined through absorption imaging. When the neutral atom cloud is allowed to expand prior to ionization, then the initial plasma size is needed.

The plasma size is determined by imaging the plasma onto the optically filtered ICCD camera. The fluorescence is fit to a Gaussian to determine the rms size. The ratio between the neutral atom cloud size and the plasma size is then used to find the plasma density,

$$n_p = n_{MOT} IF \left(\frac{\sigma_p}{\sigma_{MOT}} \right)^3. \tag{4.15}$$

Where spherical symmetry is assumed. n_{MOT} is the density of the neutral atom cloud from absorption imaging, σ_{MOT} and σ_p are the neutral atom cloud size and plasma size, respectively.

4.6 Photo-Ionization and Electron Temperature

A two stage photo ionization process is used to ionize the neutral atom clouds of both Ca and Yb atoms. The pulses are generated from two high-powered Nd:YAG pulse lasers. In both the Ca and Yb case, the second harmonic is used for pulse amplification of the excited state laser, while the third harmonic is used to pump the ionization pulse dye laser cavity.

The neutral atom energy level structures for Ca and Yb are nearly identical, as seen in Fig. 2.6a and Fig. 2.6b. In the case of Ca, 423 nm and 390 nm pulses are used to excite the atoms from

the $4s^2\ ^1S_0 \rightarrow 4s^2\ ^1P_1$ and ionize from the $4s^2\ ^1P_1$ state respectively. Likewise for Yb, 399 nm and 394 nm pulses are used to excite the atoms from the $6s^2\ ^1S_0 \rightarrow 6s6p\ ^1P_1$ and ionize from the $6s6p\ ^1P_1$ state respectively.

The energy of the ionization laser pulse determines the amount of energy that is given to the ejected electrons at the time of plasma formation, as show in Fig. 2.6a, Fig. 2.6b. In this work, we have precise control over the ionization pulse wavelength to within 1 cm^{-1}. The energy of the ejected electrons, ΔE, sets the initial electron temperature of the plasma,

$$\begin{aligned} T_e(0) &= \frac{2}{3}\frac{\Delta E}{k_B} \\ &= \frac{2}{3}\frac{hc}{k_B}\left(\frac{1}{\lambda_{Pulse}} - \frac{1}{\lambda_{IL}}\right) \end{aligned} \tag{4.16}$$

where h is Planck's constant, c is the speed of light, k_B is Boltzmann's constant and $1/\lambda_{Pulse}$ and $1/\lambda_{IL}$ are the ionization pulse laser wavenumber and ionization limit wavenumber respectively. The electron temperature drives the expansion of the plasma, for more detail see section 4.15.

One thing to consider is the effect of the magnetic field on the electron temperature. In Section 4.8, it explains the effect of a magnetic field on energy levels of both atoms and ions. In Fig. 3.1b, the energy level diagram for the two stage photo ionization process of Ca is given. When a magnetic field is applied, the energy levels of Ca are Zeeman split and can be calculated using Eq. 4.17 and 4.18. In the ground state, $4s^2\ ^1S_0$, the total angular momentum quantum number is $J = 0$, resulting in $m_j = 0$. By inspection of Eq. 4.17 there is no Zeeman splitting of the ground state.

In the excited state, $4s^2\ ^1P_1$, $J = 1$ resulting in one magnetically unperturbed state, $m_j = 0$ and two Zeeman shifted states, $m_j = \pm 1$. Using Eq. 4.18, we find that the Lande g-factor for these energy levels is $g = 0.99986$ and the change in wavenumber, $\Delta E = \pm 0.934\ B\ \text{cm}^{-1}/\text{T}$, as shown in Fig. 3.1b. Where B is the magnitude of the magnetic field. It is clear to see that by driving the $4s^2\ ^1S_0 \rightarrow 4s^2\ ^1P_1\ m_j = 0$, no states are perturbed due to the magnetic field, meaning there will be no change in the electron temperature.

It is also helpful to note that by drive the $4s^2\ ^1S_0 \rightarrow 4s^2\ ^1P_1\ m_j = \pm 1$ transition, the change in the electron temperature would only be $\Delta T_e = 0.18$ K at $B = 0.2$ T. Where $B = 0.2$ T is the highest magnetic field strength achievable, see section 4.12. In a typical experiment, we set the electron temperature in the range of 50 K to 250 K. A variance of $\Delta T_e = 0.18$ K is negligible.

4.7 Dark States

Dark states are metastable energy levels that are an alternative decay route to the ground state from an excited state. There are many examples of dark states, as can be seen in Fig. 2.6 and Fig. 3.1a. They are coined dark states because if an electron falls into one of these states, it becomes invisible to the probe laser beam, resulting in a decrease in the fluorescence signal.

We measure the expansion of the plasma using laser induced fluorescence, as described in Section 4.2. As long as the electrons fall back into the respective ground states, they can continue to be excited by the probe laser beam. In Ca^+, the ions are excited to the $^2P_{3/2}$ state. From the $^2P_{3/2}$ state the ions will fall to either the ground state, $^2S_{1/2}$, or to the $^2D_{5/2}$, $^2D_{3/2}$ dark states. The probability of the electron to fall into each of these states, also known as the branching fraction, are 93.56%, 5.87% and 0.66% respectively [111].

The ions that end up in the $^2D_{5/2}$ and $^2D_{3/2}$ dark states in Ca^+ are excited back into the $^2P_{3/2}$ state using 850 nm and 854 nm laser beams, as shown in Fig. 2.6c. This ensures that the signal does not decay throughout the measurement period of the experiment. For Yb^+, there is only one dark state, $5d\ ^2D_{3/2}$, with a branching fraction of 0.5% [112]. Similar to Ca^+, the Yb^+ dark state can be optically pumped using a laser beam at 935 nm. The relevant states and respective branching fractions for Ca^+ and Yb^+ are shown in Fig. 2.6c and Fig. 2.6d.

When an external magnetic field is present, the energy levels become Zeeman split, as described in Section 4.8. In a magnetized Ca^+ plasma, the 2 dark states split into 10, as seen in Fig. 4.3. After

taking into account selection rules, as described in Section 4.2, 5 dark states are possible decay paths, as seen in Fig. 3.1a.

There are two possible solutions to this problem. The first would be to have 5 lasers to optically pump out of each of the respective dark states. Although there are many reasons as to why this is not a feasible solution such as unnecessary complexity, it is not financially feasible at this time. The second solution is to pulse on the probe laser for a short period of time.

Pulsing of the probe laser ensures that during the observation period, optically dark states have a negligible effect on the fluorescence signal. It is shown in Fig. 3.1c that the probe laser and camera are turned on at the same time. The camera collects fluorescence for 100-200 ns and then stops the collection. This technique was used to collect the data in Chapter 3.

4.8 Zeeman Splitting

Each atomic and ionic species has a very distinct energy level structure that splits when a magnetic field is present. This energy splitting due to the magnetic field is called Zeeman splitting, given by

$$\Delta E = \mu_B g m_j B, \tag{4.17}$$

where ΔE is the energy splitting, B is the magnetic field and m_j is the magnetic angular momentum quantum number. The Bohr Magneton, $\mu_B = e\hbar/2m_e$, is given in terms of physical constant, where e and m_e are the electron charge and mass respectively and $\hbar$ is Planck's constant. Finally, g is the Lande g-factor,

$$g = g_l \frac{j(j+1) - s(s+1) + l(l+1)}{2j(j+1)} + g_s \frac{j(j+1) + s(s+1) - l(l+1)}{2j(j+1)}, \tag{4.18}$$

where s, l, j are the principal quantum numbers for the spin, orbital angular momentum and total angular momentum respectively. The spin and angular momentum g-factors are given by $g_s = 2.002319$ and, $g_l = 1 - 1/M$ respectively, where M is the ratio of the nuclear mass to the electron

mass. In the case of ^{40}Ca, $g_l = 1 - m_e/40m_p = 0.999986$, with m_p being the proton mass, for Yb we get $g_l = 0.999997$.

Zeeman splitting effects both the neutral atom and ion energy levels. When the magnetic field is strong enough this energy splitting becomes significant. In this work our magnetic field strengths are well within the linear regime for Zeeman splitting and so quadratic terms are neglected.

4.9 Probe Laser Characteristics

In the work presented in Chapter 2 we used a Gaussian profile laser beam cylindrically focused into a sheet at the point of the plasma. The motivation behind this was to reach a width of 300 μs and not be limited by diffraction as we would by illuminating a slit, where the diffraction is strongly dependent upon the slit width, d,

$$\sin(\theta) = n\lambda/d, \tag{4.19}$$

with n being the diffraction order and λ the wavelength. On the other hand, using a cylindrically focused laser beam presented its own challenges.

Considering the geometric limitations of slit and lens placement, if we approximate our wavelength to be $\lambda = 400$ nm and the distance from the slit to the plasma as 0.5 m then the first order diffraction peak is at 390 μm from the center of the laser beam. This more than triples the size of the beam at the location of the ions. By replacing the slit with a $f = 300$ mm cylindrical lens we can achieve a smaller laser beam sheet thickness and the same, if not better, angular spread.

The cylindrical focused laser beam comes with its own problems. The size of the laser beam at the location of the ions is not well known, causing uncertainty in the laser intensity. Under or over estimating the laser intensity causes an artificial increase or decrease, respectively, in the measured ion velocity and temperature, see section 4.14 for more details. Another drawback is that because it is a focused laser beam, the projected ion velocity will be in the $\hat{k}$ direction and not exactly in

the $\hat{z}$ direction, which is assumed in the analysis. Although this effect may be small, it could cause significant problems when a magnetic field is present.

We can quantify the angular contribution to the measured ion velocity as follows. A Gaussian beam incident through a cylindrical lens can be characterized in a functional form of the rms width,

$$\sigma(z) = \sigma_0(1 - z/f) \tag{4.20}$$

where f is the focal length of the lens and z is the distance from the lens. The angle of the ray is then dependent upon the size of the laser beam. We can take this a little further and calculate the angle of the ray incident with an ion in the plasma. We will start by defining the origin at the center of the plasma and the displacement of the lens as z_0. As shown in Fig.4.8, the laser beam propagates in the s coordinate, focuses in the y coordinate and remains collimated in the x coordinate. The laser profile of a cylindrically focused laser is

$$G_{laser}(x,y) = \frac{1}{\sigma_0^2(1-z/f)2\pi} e^{-\frac{y^2}{2\sigma_0^2(1-z/f)^2}} e^{-\frac{x^2}{2\sigma_0^2}} \tag{4.21}$$

where σ_0 is the rms width of the Gaussian beam before the cylindrical lens. If you follow a single ray as the laser propagates in the z direction, the argument in the exponential remains a constant. Using the z and y location of the ion, (y_{ion}, z_{ion}), we can find the starting location of the ray at the point of the lens,(y_0, z_0),

$$\frac{y_{ion}^2}{2\sigma_0^2(1-(z_0-z_{ion})/f)^2} = \frac{y_0^2}{2\sigma_0^2(1-(z_0-z_0)/f)^2}$$

$$y_0 = \frac{y_{ion}}{(1-(z_0-z_{ion})/f)}.$$

Here we have let $x = 0$, since the angle is x invariant, and shifted the distribution to account for the origin being at the center of the plasma. Since we are only interested in the angle θ we can see from Fig. 4.8 b.),

$$\tan\theta = \frac{y_0}{f}$$

$$= \frac{y_{ion}}{(f-(z_0-z_{ion}))},$$

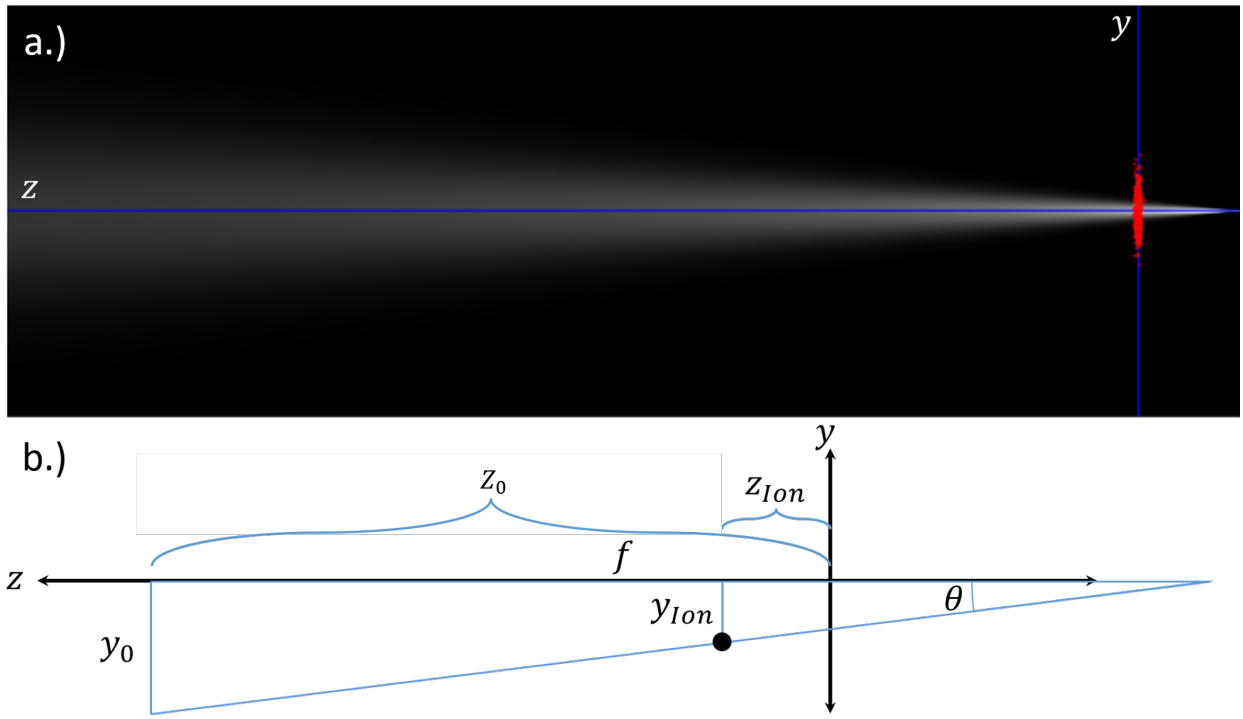

Figure 4.8 a.) Illustration of a Gaussian laser beam being cylindrically focused through the plasma, scale is 10:1 in z:y-axis. b.) Diagram for calculating the angle of a ray of light from the focused laser beam incident with an ion in the plasma. f is the focal length of the cylindrical lens, z_{Ion} and y_{Ion} is the position of the ion, z_0 is the distance from the lens to the center of the plasma. y_0 is the position of the incident photon at the lens.

which gives the incident angle of the light on the ion as,

$$\theta = \arctan\left(\frac{y_{ion}}{(f-(z_0-z_{ion}))}\right). \tag{4.22}$$

With the angle of the ray of light incident on each ion we can take the measured ion velocity and project it in the $\hat{z}$ direction. In the worst case scenario we let $y_{ion} = 1$ mm, $f = 300$ mm, $z = 0.5$ mm and $z_{ion} = 1$ mm, which gives $\theta = 0.29$ rad and a $\mathbf{v}\hat{z}$ velocity of $0.958|\mathbf{v}|$, resulting in an $\approx 5\%$ increase in the measured velocity.

The development of the new optical system, as given in Section 4.10, provides a way to eliminate the limitations and uncertainties that are present in the cylindrically focused probe laser beam method. By using the 1:1 optical system, the incident laser beam will retain the same size and divergence. This is no surprise, the magic comes when placing a slit less than the focal length away from the optical system, as seen in Fig. 4.9. The slit will be imaged after the focus a distance equal to the displacement of the slit from the focus, $a = b$ as detailed in Section 4.10. By choosing the focal length appropriately, the image of the slit can be placed at the trap center inside the chamber. The zero order beam will be collimated, and the higher order diffraction will be imaged back onto itself.

The new probe laser imaging system provides a number of advantages. First, it creates a collimated and diffraction eliminated image of a slit at the center of the plasma. Second, it allows us to know the intensity of the laser beam by measuring it outside the vacuum chamber. Third, the maximum angle of the first order diffraction is given by Eq. 4.19 which is considerably smaller than Eq. 4.22. This system can be used in many future experiments for observing a small slice of the plasma or the slit can be removed as was done in Chapter 3.

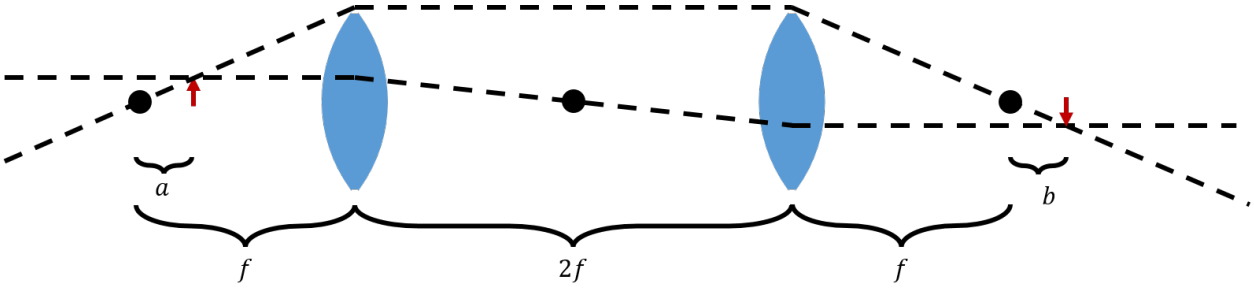

Figure 4.9 Ray trace diagram for a 1:1 telescope. The red arrow is the object being imaged, the black points are the location of the focus, f is the focal length of the identical lenses. a and b are the distances of the object and image from the focus, respectively. It is found that in the case of a 1:1 telescope $a = b$.

4.10 Imaging Optics

In this work, I developed a new optical imaging system that has been adopted in our experiment to guarantee one to one imaging. This new system is used for imaging the absorption of the neutral atom cloud, the imaging of the plasma onto the ICCD camera and the imaging of the probe laser onto the plasma. The new imaging technique has greatly improved the reproducibility of our experiments and provides consistent agreement between systems, such as MOT size between absorption imaging and ICCD Camera, as well as velocity and temperature measurements between PMT and ICCD camera. This technique was not developed until after the work in Chapter 2.

When imaging the trapped neutral atoms or plasma, it is important to know the magnification of the image onto the camera. In general, one to one magnification is desired. In the past, this was achieved by placing a lens $2f$ away from the object and placing the face of the camera $2f$ away from the lens. Where f is the focal length of the lens. This provides 1:1 imaging of the object, assuming perfect placement. In our specific case, it is very hard to know the exact position of the neutral atoms or plasma because it is inside the vacuum chamber. Although the errors are not assumed to be large, it has proven to provide a lot of uncertainty and inconstancy in determining the size and density of the neutral atoms and plasma.

For this reason, a new optical system was developed to guarantee 1:1 imaging. Two identical lenses are used and mounted at a fixed $2f$ apart, creating a 1:1 telescope, as seen in Fig. 4.9. When this is done, magic happens and the object's position does not need to be well known. Let's start by building our optical system using an ABCD matrix. We will let the object be a distance a away from the focus of the first lens. The distance between the two lenses is $2f$ and the location of the image in b away from the focus of the last lens.

$$\underbrace{\begin{pmatrix} 1 & f-b \\ 0 & 1 \end{pmatrix}}_{\text{Image location}} \underbrace{\begin{pmatrix} 1 & 0 \\ -1/f & 1 \end{pmatrix}}_{\text{Second Lens}} \overbrace{\begin{pmatrix} 1 & 2f \\ 0 & 1 \end{pmatrix}}^{\text{Distance Between Lenses}} \underbrace{\begin{pmatrix} 1 & 0 \\ -1/f & 1 \end{pmatrix}}_{\text{Fist Lens}} \underbrace{\begin{pmatrix} 1 & f-a \\ 0 & 1 \end{pmatrix}}_{\text{Object Location}} = \begin{pmatrix} -1 & b-a \\ 0 & -1 \end{pmatrix} \tag{4.23}$$

We can see from matrix position A and C, the spatial and angular magnification are -1. Which means that we have 1:1 imaging, as expected. Matrix position C tells us that there is no additional focusing of the ray bundle from the optical system. Doing a ray trace of Eq. 4.23 we find

$$\begin{pmatrix} y_i \\ \theta_i \end{pmatrix} = \begin{pmatrix} -1 & b-a \\ 0 & -1 \end{pmatrix} \begin{pmatrix} y_o \\ \theta_o \end{pmatrix} \tag{4.24}$$

$$= \begin{pmatrix} -y_o + (b-a)\theta_o \\ \theta_o \end{pmatrix}, \tag{4.25}$$

where y_o is the object height, θ_o is the object ray angle. Likewise, y_i is the image height, θ_o is the image ray angle. We already know that the spatial and angular magnification is -1, which means that $y_o = -y_i$ and $\theta_o = -\theta_i$. Consequently, $(b-a)\theta_o = 0$, and since θ_o cannot be restricted to $\theta_o = 0$, we find that $a = b$.

This is a remarkable result. This tells us that if the object is within $\pm f$ of the focal length of the lens, then exact 1:1 imaging can be achieved simply by placing the detector the distance a away from the focus on the opposing side of the optical system. This is used for imaging the neutral atom

cloud and plasma. Since the location of the atoms or ions is no longer important, we just ensure that the lenses are exactly spaced. Placing the camera such that the image is in focus guarantees 1:1 imaging without knowing exactly where the plasma or neutral atom cloud are. This also provides a clever way of achieving diffraction eliminated imaging of a slit onto the plasma, as described in Section 4.9.

4.11 Probe Laser Intensity

The intensity of the probe laser is not uniform. It is a Gaussian laser beam with an rms width of $\sigma = 1.46$ mm. We measure the power of the beam centered through a 1/8 in diameter aperture (3.175 mm). Given the rms width and the aperture size, we find that there is a 45% power difference between the peak and the edge of the distribution. The average intensity, I_{avg}, across the region is $I_{avg} = Power/Area$. The power is measured using a power meter and the area is given by the aperture size. Ultimately what we care about is the peak intensity, which is represented as the amplitude in the Gaussian laser profile,

$$I(r) = I_{peak} e^{-r^2/2\sigma^2}. \tag{4.26}$$

Integrating both sides over the area of the aperture yields the measured intensity from the power meter,

$$I_{avg} = \frac{I_{peak}}{\pi a^2} \int_0^{2\pi} \int_0^a e^{-r^2/2\sigma^2} r dr d\phi, \tag{4.27}$$

resulting in a peak intensity of,

$$I_{peak} = 1.325 I_{avg}. \tag{4.28}$$

The peak intensity along with the known Gaussian laser beam profile can then be used to more accurately model the spatial temperature of the plasma using the ICCD camera. For more details, please see section 4.14.

4.12 Magnetic Field Coils

A Helmholtz coil configuration is used to supply a strong, uniform magnetic field. The magnetic field can be calculated along the z axis using Biot-Savart's law,

$$B_z(z) = \frac{\mu I N r_0^2}{2}\left(\frac{1}{\left(r_0^2+(z-z_0)^2\right)^{3/2}}+\frac{1}{\left(r_0^2+(z+z_0)^2\right)^{3/2}}\right)\hat{z} \tag{4.29}$$

where μ_0 is the vacuum permeability, I is the electrical current, N is the number of turns in a coil, r_0 and z_0 are the radius and displacement of the coil respectively. From the above equation, we can see that the magnetic field, B_z, linearly depends on the current and number of turns.

The limitations of the magnetic field strength come from voltage and current limits, ohmic heating, and geometrical restrictions. A 15kW power supply is used to provide upwards of 250 A at a max voltage of 60 V. Whether we are voltage or current limited will be dependent upon the wire used in the Helmholtz coils. Using Ohms law,

$$V = IR, \tag{4.30}$$

where V, I, R are the voltage, current and resistance respectively, we can find an upper limit to the allowed resistance as 60 V/250 A = 0.24 Ω.

Copper wires have a resistivity of $\rho = 1.68 \times 10^{-8}$ Ωm. The resistance of a given wire is given by the following relation,

$$R = \rho l/A, \tag{4.31}$$

where l and A are the length and cross-sectional area of the wire, respectively.

We need to also consider the power dissipated by the wire. This is important for two reasons, the current needs to be able to pass without compromising the vacuum pressure or the electrical circuit. The power, P, dissipated from an Ohmic wire is

$$P = I^2 R. \tag{4.32}$$

From this and Eq. 4.31, it is clear to see the strong limitation in the size of the wire due to the current. As an example, a 22 AWG copper wire is rated for 10 A of continuous current within a vacuum chamber. The resistance is 23 Ω/km, if the wire is 1 m long then the power dissipated is 2.3 W. Pushing 250 A would exceed the rated limit by a factor of 625. This would mean that to appropriately choose a wire size for our desired current we would need a wire diameter of about 2 cm. This wire diameter is far from feasible for our vacuum application.

The way around the rated wire size is to pulse on the current for a short period of time. If the current is pulsed on for only half of a second every second, then the power dissipated would be reduced by a factor of 2, which decreases the required wire diameter by a factor of $\sqrt{2}$. This can be quantified by introducing a duty cycle for power dissipation, given by the ratio of the effective power to the rated power,

$$D = \frac{I^2}{I_{rated}^2} \nu_{rep} \Delta t, \tag{4.33}$$

where I_{rated} is the current rating of the wire and I is the applied current. Δt is the pulse width and ν_{rep} is the repetition rate. If D is less than 1 then we are within the rated specifications for the given wire.

In our experiment, achievable rep rates range from $\nu_{rep} = 1 - 10$ Hz. Likewise, the desired pulse width is $\Delta t = 500$ μs, as detailed in Section 4.13 and shown in Fig. 3.1c. It is important to note that the main source of heat dissipation is usually due to conduction with air. In a vacuum, conduction is no longer a source of heat dissipation, and the main source becomes radiation. In our case, the wires we have chosen are rated for vacuum use. Since we are coiling our wire, the amount of heat dissipated due to radiation is also decreased, resulting in approximately a 1/3 reduction in the rated current. On the other, the rated current of a wire is usually given as the minimum direct current required to raise the temperature of the wire from roughly 22 C to 30 C. In our application the only limitation from heating up the wire hotter is out gassing, which compromises the vacuum pressure. As a rule of thumb, we will take 2/3 of the rated current as the limit.

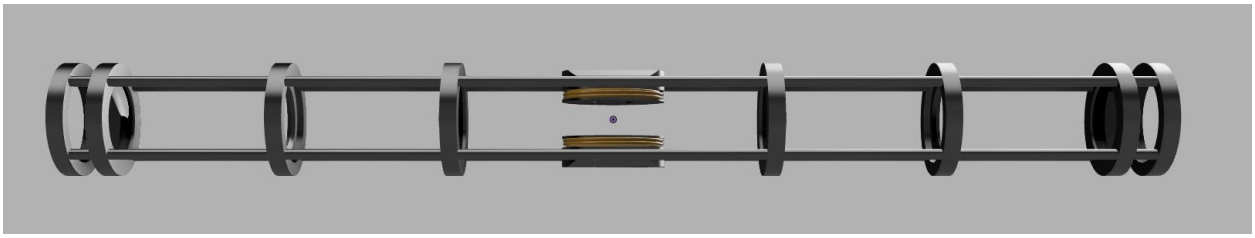

Figure 4.10 CAD drawing of the assembled coils, coil housing and optical system

Considering all this, using Eq. 4.31 and Eq. 4.32, the maximum current at 250 A becomes an effective $I = 5.6 - 17.7$ A. In return this puts lower limits on the wire diameter of $0.8 - 2.6$ mm, dependent upon the repetition rate.

The final major limitation to consider is the geometric restrictions from the vacuum chamber and the laser beams. As shown in Fig. 4.10, the Helmholtz coils attach to the 4 rods that are used to mount and place the lenses for imaging the plasma. This optical system, which is described in more detail is section 4.10, slides in through a 2.75 in conflat flange, with an inner diameter of 34 mm. As shown in Fig. 4.11, the 4 rods are symmetrically placed where the inner facing surfaces are 18.3 mm apart. This provides a geometrical ceiling for the coils of 9.15 mm from the center of the chamber. The geometric floor of the coils is found by considering the MOT laser beams, which have a rms width of $\sigma = 1.5$ mm. The geometric propagation of these beams are described in Section 4.3.

To ensure no clipping of the laser beam a 10 mm gap is required, also requiring a floor or 5 mm from the center of the chamber. This also tells us the minimum inner coil radius, or 5 mm. From the inner diameter of the conflat flange and the coil ceiling, we find that the maximum outer coil radius is 15.5 mm. After taking into account machining limitations for constructing the coil housing, we illustrate the optimal Helmholtz coils using a commercially available 18 AWG wire (1 mm diameter) in Fig. 4.11.

After considering all the limitations, a maximum magnetic field strength can be approximated. In the final build, 19 turns in each coil was achieved. Using a slightly modified version of Eq.4.29 to account for each turn's position, we find a maximum achievable magnetic field strength of 0.31 T

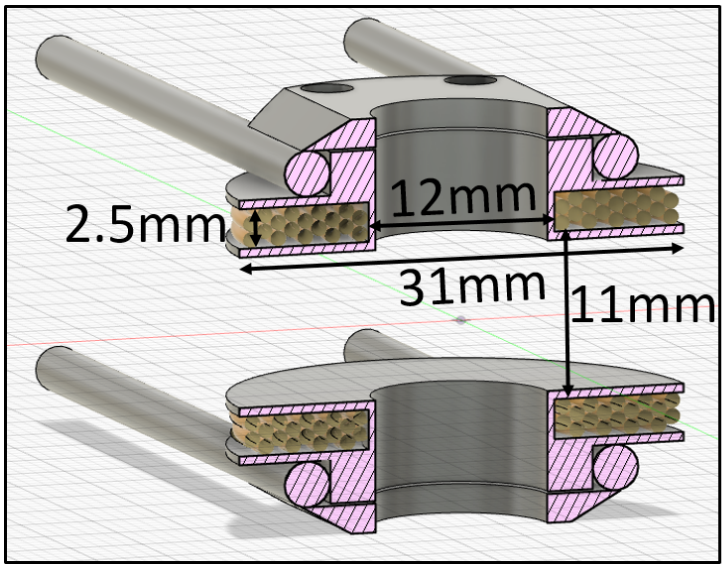

Figure 4.11 CAD drawing of the mounted coils and coil housing.

at the origin. The magnetic field along the z-axis is shown in Fig. 4.12. Due to the limitations in building the coils, a small gradient does exist in both the z and r directions. Experimentally the maximum applied current is found to be $I = 150$ A.

Using $I = 150$ A, and $z = r = 1$ mm for the worst case scenario we find,

$$\Delta B_z = 0.0013 \text{ T} \rightarrow 18 \text{ MHz} \tag{4.34}$$

$$\Delta B_r = 0.0054 \text{ T} \rightarrow 76 \text{ MHz}, \tag{4.35}$$

where the probe laser transition ${}^2S_{1/2}\, m_j = 1/2 \rightarrow {}^2P_{3/2}\, m_j = 3/2$ is used to find the frequency, as given in Section 4.2. The change in magnetic field was calculated by Dr. Ross Spencer using an integration of the Biot-Savart law based on the spiral wound wires. He found a 1.4% variation in the total magnitude of B inside a 1 mm cube at trap center.

A strong uniform magnetic field is essential in order to measure suppression or enhancement of transport properties, and it is the motivation for the work done in Chapter 3. Extra precautions are taken in order to shield any unwanted electric fields. The entire vacuum chamber is grounded to shield any electric fields originating from outside the vacuum chamber. Likewise, the coil housing

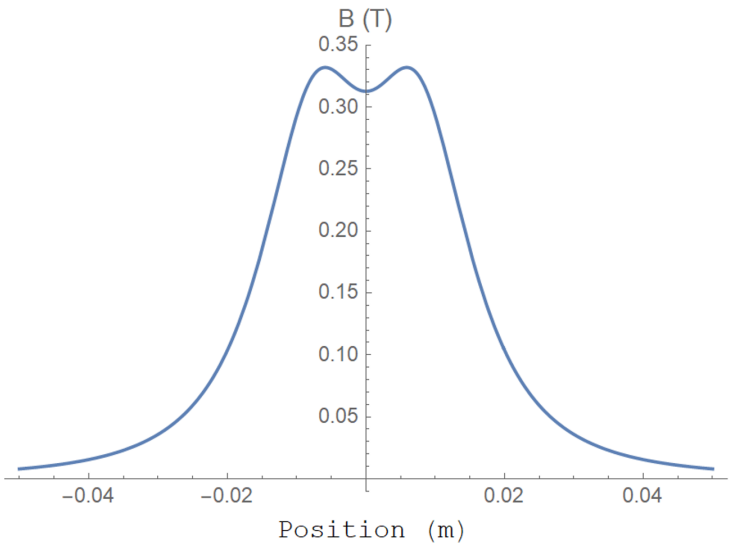

Figure 4.12 Theoretical magnetic field strength along the z axis. The measured experimental maximum is found to be 0.32 T, the actual is 0.2 T

units are grounded to the vacuum chamber to shield out any electric fields generated from the electrical potential difference between magnetic field coils.

4.13 Switch Circuit for Turning on/off B-Field

In this work we designed a switch to turn on and off the strong uniform magnetic field in under 500 μs. The magnetic field coils create a strong inductive load in the circuit. When a sudden change of current occurs the inductive load resists the change in current, causing large back EMF voltage spikes,

$$\mathscr{E} = -L\frac{dI}{dt}. \tag{4.36}$$

Where L is the inductance of the coils, given by

$$L = \frac{\mu_0 A N^2}{l} \tag{4.37}$$

where A, l are the area and length of the coils and N is the number of turns. Given the size of the coils found in Section 4.12, we find that $L_1 \approx 100$ μH, labeled in Fig. 4.13. Which gives a back

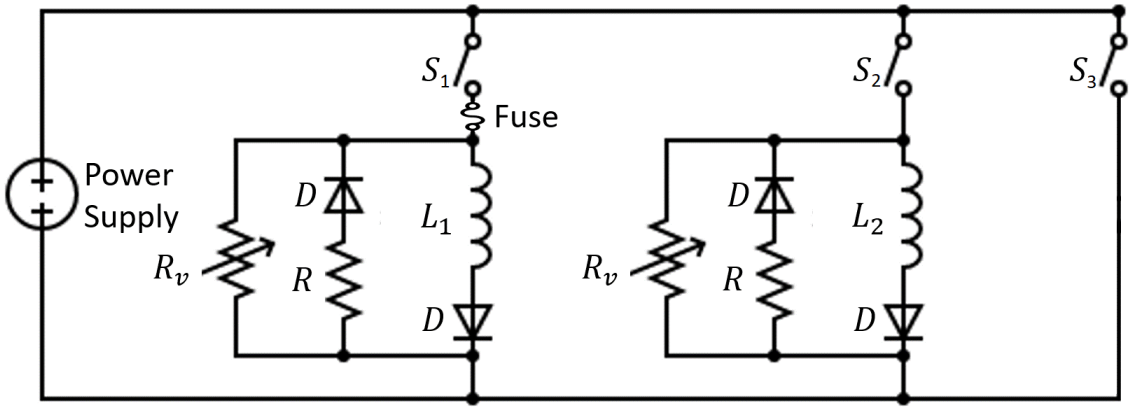

Figure 4.13 Diagram for the electrical circuit used to turn on and off the magnetic field applied to the plasma. *D*, represents electrical diode, all diodes in the system are rated for a continuous 300 A. Likewise, *R*, represents resistor and each resistor in the circuit is a 1 Ω resistor. R_v is for varistor, and S is the IGBT switch. Again, all varistors and switches are identical. The magnetic field coils are labeled as, L_1 and the inductive resistor used as an intermediate current ramping stage is L_2.

EMF of $\mathscr{E} \approx -33$ V. This voltage spike is not large enough on average to cause any damage to our switches or other components of the circuit. At early times, when the current change is the steepest, this value could much higher. A protective circuit is used to suppress the EMF voltage spike and reduce ring down time.

In an LR circuit, the ramp up and down time is given by the time constant $\tau = L/R$. The resistance in the coils is about 0.09 Ω, which means that our time constant is $\tau = 0.9$ ms. This is far too long given the requirement that the current needs to ramp from 0 to 150 A in 500 μs. This is done by building an almost identical circuit in parallel as an intermittent ramp up stage, as seen in Fig. 4.13. The difference between the L_1 and L_2 circuit is the duty cycle and inductance. The inductor, L_2, is a large solenoid made from 14 AWG wire. The diameter of the solenoid is 2 in and

contains approximately 200 turns. Using Eq. 4.37, we find that $L_2 = 300\ \mu$H. The number of turns is chosen such that the total resistance in both $L_!$ and L_2 are equal, about 0.09 Ω.

The current rating for a 14 AWG copper wire at 75 C is 20 A. The power dissipated assuming continuous current is,

$$P = I^2 R. \tag{4.38}$$

Letting $I = 150$ A and $R = 0.09\ \Omega$, we get $P = 2025$ W. The Power rating of the wire is only $P = 36$ W. This discrepancy is reconciled by only pulsing on the current for 20 ms at 10 Hz, reducing the dissipated power to 405 W. This is still a factor of 10 larger than the power rating of the wire. For this reason the L_2 inductor is water cooled, the solenoid sits inside a large sealed stainless steel cylinder that has water continuously flowing through it. Since we are unable to have current passing through the L_2 inductor continuously, an additional short circuit stage for ramping up the current is added.

In order to operate the power supply at constant current, the current must be able to flow continuously. For this reason, there are 3 stages for ramping up the current for creating a constant, uniform magnetic field across the plasma. The first stage is the short circuit. This allows us to set the desired current. In a way, this is the idle stage. When we want to ramp up the current, we open switch 2 and then 15 μs later close switch 3. This redirects the current from the short circuit to the L_2 inductor. Because of the resistance difference between the two paths, the power supply has to supply more voltage in order to reach the desired current. It takes about 20 ms to reach a steady state current. After 20 ms, switch 1 is opened and 15 μs later switch 2 is closed, redirecting the current into the magnetic field coils, L_1. If the resistance in L_2 and L_1 are the same, then the current rapidly ramps up to a constant current in 500 μs. The timing of the switches is detailed in Fig. 4.14.

The inductor L_2 is specifically designed to match the resistance in L_1. Since the resistance is the same, when the current is switched over, the power supply does not need to discharge or charge

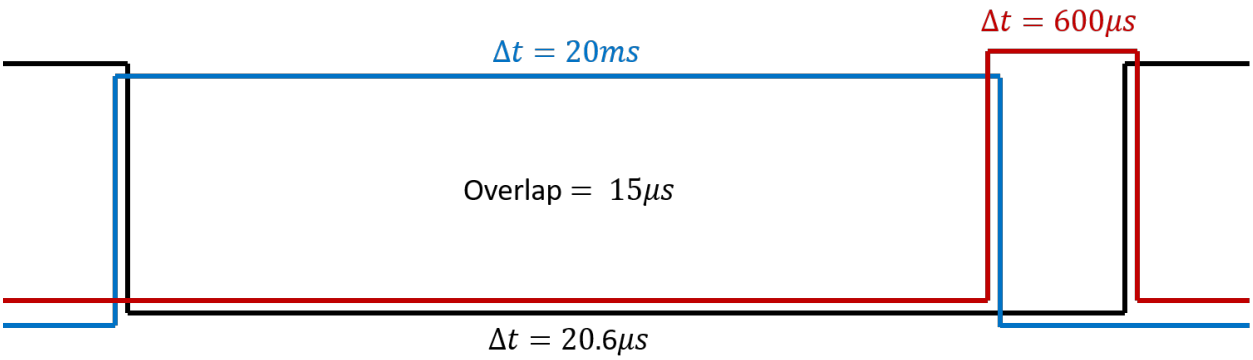

Figure 4.14 The black line indicates when the short circuit is turned off and back on. The blue line indicates when the L_2 inductor circuit is turned on and off. This circuit is only on for 20 ms. giving it enough to ramp to a maximum constant current. The red line indicates when the magnetic field coils are turned on and off. The coils take about 500 μs to ramp up to a constant current. At that time, the plasma is ionized and measured prior to the magnetic field coils turning off. The 15 μs overlap is in place to give time for the switches to respond to the electrical pulse which tells the switch to open or close. Turn on time is 5 μs and the turn-off time is 10 μs for the switches. For this reason, there is a 15 μs overlap to ensure current is always flowing.

up the capacitors to accommodate the change in resistance. The fast feedback of the power supply competes with the inductor, allowing for a turn on time of 500 μs.

In the case that the resistance in L_1 and L_2 do not match, the current would initially rapidly increase but then slowly linearly increase or decrease to the set current value. The slow increase or decrease comes from the charging or discharging of the capacitors to account for the increase or decrease in resistance, respectively. The rate of reaching a constant current when the resistances do not match is 20 ms.

4.14 General Data Analysis

Laser induced fluorescence, as described in Section 4.2, is used to fluoresce the ions in the plasma. The fluorescence is collected using optically filtered photo-multiplying tubes (PMT) and an ICCD Camera. The PMT is used to collect time resolved measurements of the plasma. The Camera is

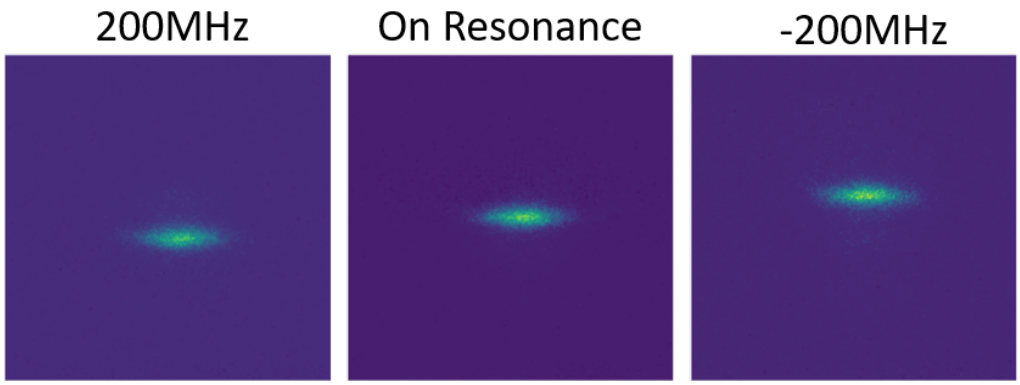

Figure 4.15 Each laser frequency detuning probes a different spatial region of the plasma. The probe laser observes the $\hat{z}$ projected velocity of the plasma. When the probe laser is detuned in the positive sense, then ions with a z velocity that are Doppler shifted into resonance and propagate in the same direction as the laser beam are fluoresced. as shown in the first figure. On resonance, we observe the ions in the center of the plasma with no z velocity. Likewise, we see the same effect if negatively detuned.

used to collect spatially resolved images of the plasma at a specific time. Both detectors are used in our analysis of UNPs.

Fluorescence from the plasma is collected at 11 laser frequency detunings, ranging from $\pm$200 MHz in 40 MHz steps. This can be seen in Fig. 2.8b and Fig. 3.2c for PMT data, and in Fig. 4.15 for camera data. The fluorescence from the PMT is compiled into a three-dimensional plot where the x-axis is laser frequency detuning, the y-axis is time and the z-axis is the fluorescence, as shown in Fig. 2.8c. A slice of the data at each time step is then fit to a Voigt profile, as shown in Fig. 4.16, where the rms frequency, ν_{rms}, is used as a fit parameter,

$$V(\nu) = \int L(\nu - \nu')G(\nu')d\nu'. \tag{4.39}$$

In this equation L and G are the Lorentzian and Gaussian profiles respectively, given by

$$L(\nu) = \frac{\frac{\gamma}{\pi}\sqrt{1+\frac{I_{probe}}{I_{sat}}}}{\nu^2 + \gamma^2\left(1+\frac{I_{probe}}{I_{sat}}\right)} \tag{4.40}$$

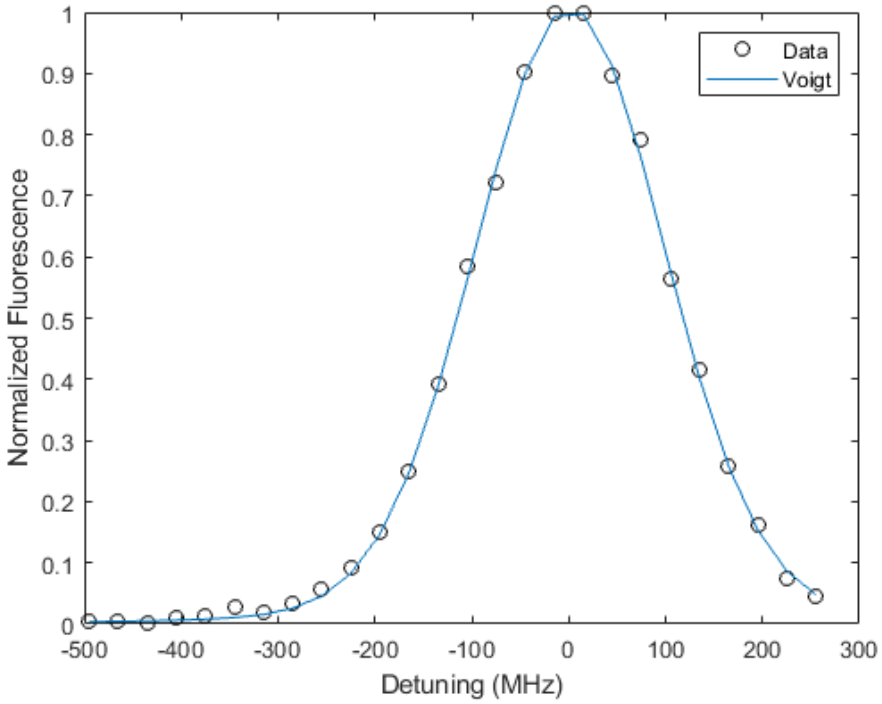

Figure 4.16 The comparison of the experimental data against a fitted Voigt profile.

and

$$G(\nu) = \frac{1}{\sqrt{2\pi}\nu_{rms}} \exp\left(\nu^2/2\nu_{rms}^2\right), \tag{4.41}$$

where ν is the laser frequency detuning from resonance, γ is the natural linewidth, I_{probe} is the probe laser intensity, I_{sat} is the saturation intensity and ν_{rms} is the rms frequency. The rms velocity of the ions is,

$$v_{rms} = \nu_{rms}\lambda, \tag{4.42}$$

where λ is the wavelength of the probe laser used to fluoresce the ions.

In this work we are interested in temperature, size and magnetic field strength. The temperature is found from the fitted rms frequency, using Eq, 4.42 to get

$$k_B T = m_i v_{rms}^2, \tag{4.43}$$

where k_B is Boltzmann's constant and m_i is the ion mass. The magnetic field strength is fond using the fitted center frequency of the Zeeman split energy level, as described in Section 3.3. The size is determined from the camera measurements.

The camera data is analyzed in a very similar way. Each pixel has fluorescence vs detuning from the 11 laser frequency detuning images. Just like in the PMT case, it is fit to a Voigt profile and the same steps are taken to find the temperature of the plasma at a specific location and time in the plasma. The size of the plasma can be determined in the vertical and horizontal direction, as described in Section 3.3.

4.15 Self Similar Expansion Model

A self similar expansion model developed by Mora [39] is an exact solution to UNP expansion in the case of no magnetic fields. We start with the equations of motion for the ions and electrons.

$$\frac{\partial \vec{v}_e}{\partial t} + (\vec{v}_e \cdot \nabla)\vec{v}_e = \frac{e}{m_e}\left(\nabla\Phi - \vec{v}_e \times \vec{B}\right) - \frac{k_B}{m_e n_e}\nabla(n_e T_e) \tag{4.44}$$

$$\frac{\partial \vec{v}_i}{\partial t} + (\vec{v}_i \cdot \nabla)\vec{v}_i = -\frac{e}{m_i}\left(\nabla\Phi - \vec{v}_i \times \vec{B}\right) - \frac{k_B}{m_i n_i}\nabla(n_i T_i) \tag{4.45}$$

Where k_B is Boltzmann's constant, n_s is the number density, m_s is the mass of the species, v_s is the velocity, B is the magnetic field, $\nabla\Phi$ is the electric field, T_s is the species temperature and e is the fundamental unit of charge.

We will start by assuming the case of no magnetic field, $B = 0$, our equations of motion then become

$$\frac{\partial \vec{v}_e}{\partial t} + (\vec{v}_e \cdot \nabla)\vec{v}_e = \frac{e}{m_e}\nabla\Phi - \frac{k_B}{m_e n_e}\nabla(n_e T_e) \tag{4.46}$$

$$\frac{\partial \vec{v}_i}{\partial t} + (\vec{v}_i \cdot \nabla)\vec{v}_i = -\frac{e}{m_i}\nabla\Phi - \frac{k_B}{m_i n_i}\nabla(n_i T_i). \tag{4.47}$$

In an UNP, the number of ions and electron are the same and their opposing charge help shield internal electric fields. This behavior is known as quasinutrality. The density profile for both the ions and electrons are the same, $n_i = n_e$. Likewise, because of the shielding that occurs in the plasma the ions and electrons are flow locked, $v_i = v_e$.

In the work by Mora, he assumes that the ion pressure term is much smaller than the electric field term. In the case of UNP expansion, the ion temperature is very low, making this a reasonable approximation. Including these assumptions into our equations of motion and subtracting the two equations give,

$$\frac{e}{m_e}\nabla\Phi - \frac{k_B}{m_e n_e}\nabla(n_e T_e) = \frac{e}{m_i}\nabla\Phi. \tag{4.48}$$

Solving for the electric field, $\nabla\Phi$, we find

$$\left(1 - \frac{m_e}{m_i}\right)\nabla\Phi = \frac{k_B}{e n_e}\nabla(n_e T_e). \tag{4.49}$$

Since $m_i \gg m_i$, this simplifies to

$$\nabla\Phi = \frac{k_B}{e n_e}\nabla(n_e T_e). \tag{4.50}$$

Plugging this into Eq. 4.47 with the pressure term neglected gives,

$$\frac{\partial \vec{v}_i}{\partial t} + (\vec{v}_i \cdot \nabla)\vec{v}_i = -\frac{k_B}{m_i n_e}\nabla(n_e T_e). \tag{4.51}$$

At this point it is appropriate to think about the initial stage of the plasma. We set the electron temperature of the plasma from the ionization pulses, this gives a spatially invariant temperature. If we assume this invariance continues for the life of the plasma, which turns out to be a good approximation, then we get

$$\frac{\partial \vec{v}_i}{\partial t} + (\vec{v}_i \cdot \nabla)\vec{v}_i = -\frac{k_B T_e}{m_i n_e}\nabla n_e. \tag{4.52}$$

The initial density profile of our plasma is given by

$$n_i(x, t = 0) = n_{i0}\exp\left(-x^2/2\sigma_0^2\right) \tag{4.53}$$

If we assume a self similar expansion then we can write the time dependent density as

$$n_i(\vec{r},t) = n_0 \frac{\sigma_0}{\sigma(t)} \exp\left[-\frac{x^2+y^2+z^2}{2\sigma^2(t)}\right] \tag{4.54}$$

plugging this into the continuity equation

$$\frac{\partial n_i}{\partial t} + \nabla \cdot (n_i \vec{v}_i) = 0 \tag{4.55}$$

and after some algebra we get

$$\begin{aligned}
&\frac{2x^2}{\sigma^2(t)}\frac{\partial\sigma(t)}{\partial t} - \frac{2xv_x}{\sigma(t)} + \frac{dv_x}{dx} \\
+&\frac{2y^2}{\sigma^2(t)}\frac{\partial\sigma(t)}{\partial t} - \frac{2yv_y}{\sigma(t)} + \frac{dv_y}{dy} \\
+&\frac{2z^2}{\sigma^2(t)}\frac{\partial\sigma(t)}{\partial t} - \frac{2zv_z}{\sigma(t)} + \frac{dv_z}{dz} \\
=&3\frac{\partial\sigma(t)}{\partial t}.
\end{aligned}$$

Suggestively this means that each axis is independent, which would be expected for a self similar expansion as we can write as

$$\begin{aligned}
\frac{\partial\sigma(t)}{\partial t} =& \frac{2x^2}{\sigma^2(t)}\frac{\partial\sigma(t)}{\partial t} - \frac{2xv_x}{\sigma(t)} + \frac{dv_x}{dx} \\
\frac{\partial\sigma(t)}{\partial t} =& \frac{2y^2}{\sigma^2(t)}\frac{\partial\sigma(t)}{\partial t} - \frac{2yv_y}{\sigma(t)} + \frac{dv_y}{dy} \\
\frac{\partial\sigma(t)}{\partial t} =& \frac{2z^2}{\sigma^2(t)}\frac{\partial\sigma(t)}{\partial t} - \frac{2zv_z}{\sigma(t)} + \frac{dv_z}{dz}
\end{aligned}$$

noticing they are the same equations, we will rewrite this for convenience as

$$\frac{\partial\sigma(t)}{\partial t} = \frac{2r^2}{\sigma^2(t)}\frac{\partial\sigma(t)}{\partial t} - \frac{2rv}{\sigma(t)} + \frac{dv}{dr},$$

solving the differential equation yields,

$$v_i = r\frac{d}{dt}\ln\sigma(t). \tag{4.56}$$

Now that we have an equation for the velocity of the ions we can plug this into the ion equation of motion to get,

$$r\frac{d^2}{dt^2}\ln\sigma(t)+r\left(\frac{d}{dt}\ln\sigma(t)\right)^2=-\frac{e}{m_i}\frac{k_BT_e}{n_i}\frac{d}{dz}n_i \tag{4.57}$$

plugging in the functional form of the density,

$$\frac{d^2}{dt^2}\ln\sigma(t)+\left(\frac{d}{dt}\ln\sigma(t)\right)^2=\frac{ek_BT_e}{m_i\sigma^2(t)}, \tag{4.58}$$

simplify the derivatives,

$$\frac{d^2}{dt^2}\sigma(t)=\frac{ek_BT_e}{m_i\sigma(t)}. \tag{4.59}$$

In order to solve this differential equation for our system we assume an adiabatic electron temperature evolution,

$$\frac{1}{T_e(t)}\frac{dT_e(t)}{dt}=-\frac{1}{\sigma(t)}\frac{d\sigma(t)}{dt} \tag{4.60}$$

Solving for $\sigma(t)$ and T_e yields,

$$\sigma^2(t)=\sigma_0^2(1+t^2/\tau^2), \tag{4.61}$$

and

$$T_e(t)=T_{e0}\frac{1}{(1+t^2/\tau^2)}, \tag{4.62}$$

where the sound speed or characteristic expansion time is given by

$$\tau^2=\frac{m_i\sigma_0^2}{k_BT_{e0}}. \tag{4.63}$$

This treatment has been shown to be an exact solution to UNP expansion. It could be that this same treatment could be used in the case with a magnetic field to accurately predict the effect of a magnetic field on UNP plasma expansion. Unfortunately, the magnetic field puts limits on the fluid treatment, which adds in collisional effects and coupling between the radial and angular velocity components. Although an analytic solution does not seem probable, a numerical solution could be developed.

4.16 Ambipolar Diffusion

Ambipolar diffusion is a collisional model that is used to describe the diffusion of a gas. In a UNP the plasma is quasineutral, meaning the density profile for the electrons and ions are equal, causing no net charge. In the past, ambipolar diffusion has been used to describe the expansion of a UNP. In this work, we model our plasma using ambipolar diffusion and find that it fails to model UNP expansion both with and without a magnetic field present.

We will start by defining the diffusion equation we wish to solve.

$$\frac{\partial n}{\partial t} = \frac{1}{r}\frac{\partial}{\partial r} r D_{\perp} \frac{\partial n}{\partial r} - F_{loss} \tag{4.64}$$

The loss term, F_{loss}, is a cosmetic term to make sure the density decays as expected from the $\hat{z}$ expansion. From the results found in Chapter 3, we know that the loss term will scale as the self similar expansion model with no magnetic field, as detailed in Section 4.15. The expansion of the plasma is given in Eq. 4.61, plugging this into Eq. 4.54 and take the time derivative we find,

$$\frac{\partial n}{\partial t} = \frac{1}{r}\frac{\partial}{\partial r} r D_{\perp} \frac{\partial n}{\partial r} - n\frac{t}{\tau^2(1+t^2/\tau^2)}, \tag{4.65}$$

where $D_{\perp}$ is the diffusion coefficient perpendicular to the magnetic field. From Bittencourt [104] the diffusion coefficient in a uniform magnetic field is,

$$D_{\perp} = D_0 \frac{\nu_{ei}^2}{\nu_{ei}^2 + \Omega_{ce}^2}, \tag{4.66}$$

where $\Omega_{ce} = eB/m_e$ is the electron cyclotron frequency and ν_{ei} is the electron-ion collision frequency as given in the plasma formulary [38]. The diffusion coefficient with no magnetic field, D_0, is given by

$$D_0 = \frac{k_B T_e}{m_e \nu_{ei}}. \tag{4.67}$$

The diffusion equation is then rewritten to be unitless for computational purposes. We do this by letting $\tilde{n} = \frac{n}{n_0}$, $\tilde{r} = \frac{r}{\sigma_0}$, $\tilde{t} = \frac{t}{\tau}$, plugging these in we get

$$\frac{n_0}{\tau}\frac{\partial \tilde{n}}{\partial \tilde{t}} = \frac{n_0}{\sigma_0^2}\frac{1}{\tilde{r}}\frac{\partial}{\partial \tilde{r}} \tilde{r} D_{\perp} \frac{\partial \tilde{n}}{\partial \tilde{r}} - n_0 \tilde{n}\frac{\tilde{t}}{\tau(1+\tilde{t}^2)}. \tag{4.68}$$

From here we can simplify by multiply both side by τ/n_0, this allows us to write the diffusion equation as follows,

$$\frac{\partial \tilde{n}}{\partial \tilde{t}} = \frac{1}{\tilde{r}}\frac{\partial}{\partial \tilde{r}}\tilde{r}\tilde{D}_{\perp}\frac{\partial \tilde{n}}{\partial \tilde{r}} - n\frac{\tilde{t}}{(1+\tilde{t}^2)}, \tag{4.69}$$

where the unitless diffusion coefficient is found to be $\tilde{D}_{\perp} = D_{\perp}\tau/\sigma_0^2$.

We solve the diffusion equation using a time implicit Radua method along with a numerical technique called the method of lines. [105]. This is done by rewriting our PDE as a system of ODE's discretized in space. We will do this one step at a time, first by writing this in terms of first and second order derivatives,

$$\frac{\partial \tilde{n}}{\partial \tilde{t}} = \tilde{D}_{\perp}\frac{\partial^2 \tilde{n}}{\partial \tilde{r}^2} + \left(\frac{\partial \tilde{D}_{\perp}}{\partial \tilde{r}}\right)\left(\frac{\partial \tilde{n}}{\partial \tilde{r}}\right) + \tilde{D}_{\perp}\frac{1}{\tilde{r}}\frac{\partial \tilde{n}}{\partial \tilde{r}} - n\frac{\tilde{t}}{(1+\tilde{t}^2)} \tag{4.70}$$

We then discretize the above solution in space using a second order centered finite difference method,

$$\begin{aligned}\frac{\partial \tilde{n}_j}{\partial \tilde{t}} =& \tilde{D}_j\left(\frac{\tilde{n}_{j+1} - 2\tilde{n}_j + \tilde{n}_{j-1}}{\Delta r^2}\right) + \left(\frac{\tilde{D}_{j+1} - \tilde{D}_{j-1}}{2\Delta r}\right)\left(\frac{\tilde{n}_{j+1} - \tilde{n}_{j-1}}{2\Delta r}\right) \\ &+ \tilde{D}_j\frac{1}{r_j}\left(\frac{\tilde{n}_{j+1} - \tilde{n}_{j-1}}{2\Delta r}\right) - n_j\frac{\tilde{t}}{(1+\tilde{t}^2)},\end{aligned} \tag{4.71}$$

where the perpendicular subscripts have been removed from the diffusion coefficient. Equation 4.71 is the time integrated ODE at each grip point in the method of lines, see code in Appendix A. The results of this model can be found in Chapter 3.

Chapter 5

Conclusion

In this work, we developed two new experiments for measuring transport properties in strongly coupled UNPs. In the first, we developed the first dual species UNP and studied ion-ion thermal relaxation between a Ca^+ and Yb^+ plasma's. Second, we developed an experiment capable of achieving a 0.2 T uniform magnetic field across our plasma. In this work, we studied plasma expansion as a function of magnetic field strength.

We demonstrate that dual-species UNPs provide a new platform for studying ion transport properties in a two-temperature system. We present the first measurement of ion-ion temperature relaxation rates in a strongly coupled binary ionic mixture. We directly measure the ion temperatures and show that our MD simulations of temperature relaxation agree with experimental measurements. This reinforces the fact that the Yukawa potential, Eq. (2.5), accurately describes ion-ion interaction in dual-species UNP mixtures. This further confirms the ability of our MD simulations to capture a very complex relaxation process.

We compare the simulated relaxation rates with three popular temperature relaxation theories of varying fidelity. The closest theory is based on solving the Boltzmann equation using an effective potential. The variance between this theory and the MD simulations is likely caused by coupled modes, an effect that is omitted from the theory by design. Future work could explore the influence

of coupled modes on ion transport. Incorporating coupled modes into the Boltzmann solutions could also prove fruitful for ion transport in the regime of relatively small mass ratios.

We have developed a new method for measuring UNP expansion in a strong, uniform magnetic field. High precision laser spectroscopy and optically filtered fluorescent imaging allow for direct measurements of UNP size, temperature and magnetic field strength.

The plasma expansion parallel to the magnetic field is found to be unaffected by the strong uniform magnetic field and follows the self similar plasma expansion model exactly. Perpendicular to the magnetic field, we can control the expansion velocity by varying the magnetic field strength.

We compare our data with an ambipolar diffusion model [33] and find that it fails to describe the expansion evolution of the plasma even when an exact solution is known. We therefore considered an alternate model that predicts an exponential relation between expansion velocity and magnetic field strength. We note that the exponential decay scale is very closely given by B_0, defined in Eq. 3.5; thus, we find that

$$\frac{d\sigma_\perp}{dt} = \frac{\sigma_0}{\tau} e^{-2\frac{B}{B_0}}. \tag{5.1}$$

Because of the limitations of our data set, this relationship could be a coincidence: future experiments should verify the result for different plasma densities. The experimental methods used in this work allow for measuring magnetized transport properties within an UNP, such as thermal conductivity, diffusion, disorder induced heating suppression and temperature relaxation.

Appendix A

Ambipolar Diffusion Code

Listing A.1 Python Code for Ambipolar Diffusion

```
from IPython import get_ipython
get_ipython().magic('reset -sf')
import numpy as np
import matplotlib.pyplot as plt
from scipy.integrate import solve_ivp
import scipy.optimize as optimization
import scipy.io as sio
from scipy.io import loadmat
plt.close('all');

##############################################################################
###------------------------------Diffusion------------------------------###
##############################################################################
BB = np.linspace(1,1250,1250)*1e-4


Te0             = 96
```

```
sigma0          = 400e-6
kb              = 1.380649e-23
mp              = 1.67262158e-27
Wavelength      = 393*1e-9
c               = 299792458
e               = 1.602e-19
e0              = 8.854e-12
me              = 9.109e-31
mi              = 40*mp
n0              = 3e15

tau             = np.sqrt(mi*sigma0**2/kb/Te0)

tmax    = 20e-6/tau
xmax    = 10
dx      = 0.1
x       = (np.linspace(-xmax,xmax,int(2*xmax/dx+1))+dx/2)[:-1]
n       = np.exp(-x**2/2)
dndt    = np.zeros([len(x)])
Te0     = 96

tmax    = 20e-6/tau
time = [0, tmax]
fine_time = np.linspace(0,tmax,100)


NN = np.zeros([len(fine_time)])
Sigma = np.zeros([len(fine_time),len(BB)])
dSigmadt = np.zeros([len(fine_time)-1,len(BB)])
for q in range(len(BB)):
```

```
B                = BB[q]
omega            = B*e/me

def Diffusion(t,n):

    kL           = -(n[1]-n[2])*2/(dx*(n[1]+n[2]))
    kR           = -(n[-2]-n[-3])*2/(dx*(n[-2]+n[-3]))
    n[0]         = n[1]*np.exp(-kL*dx)
    n[-1]        = n[-2]*np.exp(-kR*dx)
    Te           = Te0/(1+t**2)
    CLambda      = 23-np.log((np.abs(n)*n0/1e6)**(1/2)*
                     (Te*8.6173281e-5)**(-3/2))
    nue          = 2.91e-6*(Te * 8.6173281e-5)**(-3/2)*np.abs(n)*
                     n0*CLambda/1e6
    D            = kb*Te/me/nue*(1/(1+omega**2/nue**2))*tau/sigma0**2
    # print(t)
    for j in range(1, int(2*xmax/dx-1)):
        dDdr = (D[j+1]-D[j-1])/2/dx
        dndr = (n[j+1]-n[j-1])/2/dx
        d2ndr2 = (n[j+1] - 2*n[j] + n[j-1])/dx**2
        zloss = n[j]*t/(1+t**2)
        dndt[j] = D[j]*d2ndr2 + dDdr*dndr + D[j]*dndr/(x[j]) -  zloss
    return dndt



time = [0, tmax]
fine_time = np.linspace(0,tmax,100)
sol = solve_ivp(Diffusion, time, n,method = 'Radau', t_eval = fine_time)
```

```
def Gaussian(x, x0, wx, a0):
    return a0 * np.exp(-(x-x0)**2/2/wx**2)

for i in range(len(sol.y[0,:])):
        popt, pcov = optimization.curve_fit(Gaussian,x,sol.y[:,i],
                                maxfev = 10000)
        Sigma[i,q] = popt[1]
dSigmadt[:,q] = (Sigma[1:,q]-Sigma[:-1,q])/(fine_time[1]-fine_time[0])
plt.figure(3)
plt.plot(fine_time,Sigma)
plt.title('my work')

plt.figure()
plt.plot(fine_time,NN)

plt.figure()
plt.plot(fine_time[:-1],dSigmadt[:,q])




plt.figure()
plt.plot(x,sol.y[:,0])
plt.plot(x,n,'k--')
plt.plot(x,sol.y[:,10])
plt.plot(x,sol.y[:,20])
plt.plot(x,sol.y[:,50])
plt.plot(x,sol.y[:,99])
```

Bibliography

[1] S. D. Bergeson, S. D. Baalrud, C. L. Ellison, E. Grant, F. R. Graziani, T. C. Killian, M. S. Murillo, J. L. Roberts, and L. G. Stanton, "Exploring the crossover between high-energy-density plasma and ultracold neutral plasma physics," Physics of Plasmas **26,** 100501 (2019).

[2] R. T. Farouki and S. Hamaguchi, "Thermodynamics of strongly-coupled Yukawa systems near the one-component-plasma limit. II. Molecular dynamics simulations," The Journal of Chemical Physics **101,** 9885–9893 (1994).

[3] M. Baus and J.-P. Hansen, "Statistical mechanics of simple coulomb systems," Physics Reports **59,** 1–94 (1980).

[4] L. B. Fletcher *et al.*, "Observations of Continuum Depression in Warm Dense Matter with X-Ray Thomson Scattering," Phys. Rev. Lett. **112,** 145004 (2014).

[5] Y. Zhou, "Rayleigh–Taylor and Richtmyer–Meshkov instability induced flow, turbulence, and mixing. II," Physics Reports **723-725,** 1–160 (2017).

[6] Y. Zhou, T. T. Clark, D. S. Clark, S. G. Glendinning, M. A. Skinner, C. M. Huntington, O. A. Hurricane, A. M. Dimits, and B. A. Remington, "Turbulent mixing and transition criteria of flows induced by hydrodynamic instabilities," Physics of Plasmas **26,** 080901 (2019).

[7] J. Clérouin, P. Arnault, B.-J. Gréa, S. Guisset, M. Vandenboomgaerde, A. J. White, L. A. Collins, J. D. Kress, and C. Ticknor, "Static and dynamic properties of multi-ionic plasma mixtures," Phys. Rev. E **101,** 033207 (2020).

[8] J. B. Taylor, "Plasma Diffusion in Two Dimensions," Physics of Fluids **14,** 1492 (1971).

[9] P. Arnold, G. D. Moore, and L. G. Yaffe, "Transport coefficients in high temperature gauge theories (I): leading-log results," Journal of High Energy Physics **2000,** 001–001 (2000).

[10] Z. Donkó and P. Hartmann, "Shear viscosity of strongly coupled Yukawa liquids," Phys. Rev. E **78,** 026408 (2008).

[11] N. V. Kabadi *et al.*, "Thermal decoupling of deuterium and tritium during the inertial confinement fusion shock-convergence phase," Phys. Rev. E **104,** L013201 (2021).

[12] C. Ticknor, J. D. Kress, L. A. Collins, J. Clérouin, P. Arnault, and A. Decoster, "Transport properties of an asymmetric mixture in the dense plasma regime," Phys. Rev. E **93,** 063208 (2016).

[13] T. C. Killian, "Ultracold Neutral Plasmas," Science **316,** 705–708 (2007).

[14] L. G. Stanton, J. N. Glosli, and M. S. Murillo, "Multiscale Molecular Dynamics Model for Heterogeneous Charged Systems," Phys. Rev. X **8,** 021044 (2018).

[15] L. G. Stanton and M. S. Murillo, "Ionic transport in high-energy-density matter," Phys. Rev. E **93,** 043203 (2016).

[16] S. D. Baalrud and J. Daligault, "Effective Potential Theory for Transport Coefficients across Coupling Regimes," Phys. Rev. Lett. **110,** 235001 (2013).

[17] R. Sprenkle, L. Silvestri, M. S. Murillo, and S. Bergeson, "Temperature relaxation in strongly-coupled binary ionic mixtures," Research Square (2021).

[18] L. G. Silvestri, R. T. Sprenkle, S. D. Bergeson, and M. M. Murillo, "Relaxation of strongly coupled binary ionic mixtures in the coupled mode regime," Physics of Plasmas **28,** 062302 (2021).

[19] T. Sprenkle, A. Dodson, Q. McKnight, R. Spencer, S. Bergeson, A. Diaw, and M. S. Murillo, "Ion friction at small values of the Coulomb logarithm," Phys. Rev. E **99,** 053206 (2019).

[20] T. Ott, H. Löwen, and M. Bonitz, "Dynamics of two-dimensional one-component and binary Yukawa systems in a magnetic field," Phys. Rev. E **89,** 013105 (2014).

[21] T. Ott and M. Bonitz, "Diffusion in a Strongly Coupled Magnetized Plasma," Phys. Rev. Lett. **107,** 135003 (2011).

[22] T. Ott, H. Kählert, A. Reynolds, and M. Bonitz, "Oscillation Spectrum of a Magnetized Strongly Coupled One-Component Plasma," Phys. Rev. Lett. **108,** 255002 (2012).

[23] M. R. Gomez *et al.*, "Experimental Demonstration of Fusion-Relevant Conditions in Magnetized Liner Inertial Fusion," Phys. Rev. Lett. **113,** 155003 (2014).

[24] S. D. Baalrud and J. Daligault, "Transport regimes spanning magnetization-coupling phase space," Phys. Rev. E **96,** 043202 (2017).

[25] F. Boeschoten, "Review of experiments on the diffusion of plasma across a magnetic field," Journal of Nuclear Energy. Part C, Plasma Physics, Accelerators, Thermonuclear Research **6,** 339–388 (1964).

[26] F. C. Hoh, "Low-Temperature Plasma Diffusion in a Magnetic Field," Rev. Mod. Phys. **34,** 267–286 (1962).

[27] S. S. Harilal, M. S. Tillack, B. O'Shay, C. V. Bindhu, and F. Najmabadi, "Confinement and dynamics of laser-produced plasma expanding across a transverse magnetic field," Phys. Rev. E **69,** 026413 (2004).

[28] G. Serianni *et al.*, "Coherent structures and transport properties in magnetized plasmas," Plasma Physics and Controlled Fusion **49,** B267–B280 (2007).

[29] J. M. Guthrie and J. L. Roberts, "Finite-amplitude RF heating rates for magnetized electrons in neutral plasma," Physics of Plasmas **28,** 052101 (2021).

[30] K. Matsuo *et al.*, "Magnetohydrodynamics of laser-produced high-energy-density plasma in a strong external magnetic field," Phys. Rev. E **95,** 053204 (2017).

[31] S. V. Lebedev *et al.*, "The formation of reverse shocks in magnetized high energy density supersonic plasma flows," Physics of Plasmas **21,** 056305 (2014).

[32] T. Ott, M. Bonitz, and Z. Donkó, "Effect of correlations on heat transport in a magnetized strongly coupled plasma," Phys. Rev. E **92,** 063105 (2015).

[33] X. L. Zhang, R. S. Fletcher, S. L. Rolston, P. N. Guzdar, and M. Swisdak, "Ultracold Plasma Expansion in a Magnetic Field," Phys. Rev. Lett. **100,** 235002 (2008).

[34] S. K. Tiwari and S. D. Baalrud, "Reduction of electron heating by magnetizing ultracold neutral plasma," Physics of Plasmas **25,** 013511 (2018).

[35] B. Scheiner and S. D. Baalrud, "Viscosity of the magnetized strongly coupled one-component plasma," Phys. Rev. E **102,** 063202 (2020).

[36] T. Lafleur and S. Baalrud, "Friction in a strongly magnetized neutral plasma," Plasma Physics and Controlled Fusion 62 (2020).

[37] S. D. Baalrud and J. Daligault, "Temperature anisotropy relaxation of the one-component plasma," Contributions to Plasma Physics **57,** 238–251 (2017).

[38] A. S. Richardson, "2019 NRL Plasma Formulary," Technical report, US Naval Research Laboratory (2019) .

[39] P. Mora, "Collisionless expansion of a Gaussian plasma into a vacuum," Physics of Plasmas **12,** 112102 (2005).

[40] S. Laha, P. Gupta, C. E. Simien, H. Gao, J. Castro, T. Pohl, and T. C. Killian, "Experimental Realization of an Exact Solution to the Vlasov Equations for an Expanding Plasma," Phys. Rev. Lett. **99,** 155001 (2007).

[41] O. A. Hurricane *et al.*, "Fuel gain exceeding unity in an inertially confined fusion implosion," Nature **506,** 343–348 (2014).

[42] B. Paxton *et al.*, "Modules for Experiments in Stellar Astrophysics (MESA): Convective Boundaries, Element Diffusion, and Massive Star Explosions," The Astrophysical Journal Supplement Series **234,** 34 (2018).

[43] R. A. Heinonen, D. Saumon, J. Daligault, C. E. Starrett, S. D. Baalrud, and G. Fontaine, "Diffusion Coefficients in the Envelopes of White Dwarfs," The Astrophysical Journal **896,** 2 (2020).

[44] L. G. Stanton and M. S. Murillo, "Ionic transport in high-energy-density matter," Phys. Rev. E **93,** 043203 (2016).

[45] L. X. Benedict *et al.*, "Molecular dynamics simulations and generalized Lenard-Balescu calculations of electron-ion temperature equilibration in plasmas," Physical Review E **86,** 046406 (2012).

[46] L. X. Benedict, J. N. Glosli, D. F. Richards, F. H. Streitz, S. P. Hau-Riege, R. A. London, F. R. Graziani, M. S. Murillo, and J. F. Benage, "Molecular dynamics simulations of electron-ion temperature equilibration in an SF_6 plasma," Physical review letters **102,** 205004 (2009).

[47] H. A. Gould and H. E. DeWitt, "Convergent Kinetic Equation for a Classical Plasma," Phys. Rev. **155,** 68–74 (1967).

[48] P. E. Grabowski, M. P. Surh, D. F. Richards, F. R. Graziani, and M. S. Murillo, "Molecular Dynamics Simulations of Classical Stopping Power," Phys. Rev. Lett. **111,** 215002 (2013).

[49] S. D. Baalrud and J. Daligault, "Mean force kinetic theory: A convergent kinetic theory for weakly and strongly coupled plasmas," Physics of Plasmas **26,** 082106 (2019).

[50] B. I. Cho, T. Ogitsu, K. Engelhorn, A. A. Correa, Y. Ping, J. W. Lee, L. J. Bae, D. Prendergast, R. W. Falcone, and P. A. Heimann, "Measurement of Electron-Ion Relaxation in Warm Dense Copper," Scientific Reports 6 (2016).

[51] J. Daligault and J. Simoni, "Theory of the electron-ion temperature relaxation rate spanning the hot solid metals and plasma phases," Phys. Rev. E **100,** 043201 (2019).

[52] J. Simoni and J. Daligault, "First-Principles Determination of Electron-Ion Couplings in the Warm Dense Matter Regime," Phys. Rev. Lett. **122,** 205001 (2019).

[53] J. Vorberger, D. O. Gericke, T. Bornath, and M. Schlanges, "Energy relaxation in dense, strongly coupled two-temperature plasmas," Phys. Rev. E **81,** 046404 (2010).

[54] A. J. Kemp, Y. Sentoku, V. Sotnikov, and S. C. Wilks, "Collisional Relaxation of Superthermal Electrons Generated by Relativistic Laser Pulses in Dense Plasma," Phys. Rev. Lett. **97,** 235001 (2006).

[55] G. Hazak, Z. Zinamon, Y. Rosenfeld, and M. W. C. Dharma-wardana, "Temperature relaxation in two-temperature states of dense electron-ion systems," Phys. Rev. E **64,** 066411 (2001).

[56] D. Gericke, M. Murillo, and M. Schlanges, "Dense plasma temperature equilibration in the binary collision approximation," Physical Review E **65,** 036418 (2002).

[57] F. R. Graziani *et al.*, "Large-scale molecular dynamics simulations of dense plasmas: The Cimarron Project," High Energy Density Physics **8,** 105–131 (2012).

[58] J. Vorberger and D. Gericke, "Comparison of electron–ion energy transfer in dense plasmas obtained from numerical simulations and quantum kinetic theory," High Energy Density Physics **10,** 1–8 (2014).

[59] G. Dimonte and J. Daligault, "Molecular-Dynamics Simulations of Electron-Ion Temperature Relaxation in a Classical Coulomb Plasma," Phys. Rev. Lett. **101,** 135001 (2008).

[60] G. Hazak, Z. Zinamon, Y. Rosenfeld, and M. W. C. Dharma-wardana, "Temperature relaxation in two-temperature states of dense electron-ion systems," Phys. Rev. E **64,** 066411 (2001).

[61] M. W. C. Dharma-wardana and F. Perrot, "Energy relaxation and the quasiequation of state of a dense two-temperature nonequilibrium plasma," Phys. Rev. E **58,** 3705–3718 (1998).

[62] M. W. C. Dharma-wardana and F. Perrot, "Erratum: Energy relaxation and the quasiequation of state of a dense two-temperature nonequilibrium plasma [Phys. Rev. E 58, 3705 (1998)]," Phys. Rev. E **63,** 069901 (2001).

[63] J. Glosli, F. Graziani, R. More, M. Murillo, F. Streitz, M. Surh, L. Benedict, S. Hau-Riege, A. Langdon, and R. London, "Molecular dynamics simulations of temperature equilibration in dense hydrogen," Physical Review E **78,** 025401 (2008).

[64] C. S. Jones and M. S. Murillo, "Analysis of semi-classical potentials for molecular dynamics and Monte Carlo simulations of warm dense matter," High Energy Density Physics **3,** 379–394 (2007).

[65] M. S. Murillo and M. W. C. Dharma-wardana, "Temperature Relaxation in Hot Dense Hydrogen," Phys. Rev. Lett. **100,** 205005 (2008).

[66] Z. Fan, Y. Liu, B. Liu, C. Yu, K. Lan, and J. Liu, "Non-equilibrium between ions and electrons inside hot spots from National Ignition Facility experiments," Matter and Radiation at Extremes **2,** 3–8 (2017).

[67] J. R. Rygg, J. A. Frenje, C. K. Li, F. H. Séguin, R. D. Petrasso, D. D. Meyerhofer, and C. Stoeckl, "Electron-ion thermal equilibration after spherical shock collapse," Phys. Rev. E **80,** 026403 (2009).

[68] J. R. Senna and S. Das Sarma, "Giant many-body enhancement of low temperature thermal-electron–acoustic-phonon coupling in semiconductor quantum wires," Phys. Rev. Lett. **70,** 2593–2596 (1993).

[69] A. J. Nozik, "Spectroscopy and hot electron relaxation dynamics in semiconductor quantum wells and quantum dots," Annual Review of Physical Chemistry **52,** 193–231 (2001).

[70] H. Ye, G. W. Wicks, and P. M. Fauchet, "Hot electron relaxation time in GaN," Applied Physics Letters **74,** 711–713 (1999).

[71] E. V. Crockett, R. C. Newell, F. Robicheaux, and D. A. Tate, "Heating and cooling of electrons in an ultracold neutral plasma using Rydberg atoms," Phys. Rev. A **98,** 043431 (2018).

[72] T. K. Langin, G. M. Gorman, and T. C. Killian, "Laser cooling of ions in a neutral plasma," Science **363,** 61–64 (2019).

[73] M. A. Viray, S. A. Miller, and G. Raithel, "Coulomb expansion of a cold non-neutral rubidium plasma," Phys. Rev. A **102,** 033303 (2020).

[74] T. Kroker, M. Großmann, K. Sengstock, M. Drescher, P. Wessels-Staarmann, and J. Simonet, "Ultrafast electron cooling in an expanding ultracold plasma," Nature Communications 12 (2021).

[75] P. McQuillen, T. Strickler, T. Langin, and T. C. Killian, "Ion temperature evolution in an ultracold neutral plasma," Physics of Plasmas **22,** 033513 (2015).

[76] G. Bannasch, J. Castro, P. McQuillen, T. Pohl, and T. C. Killian, "Velocity Relaxation in a Strongly Coupled Plasma," Phys. Rev. Lett. **109,** 185008 (2012).

[77] T. S. Strickler, T. K. Langin, P. McQuillen, J. Daligault, and T. C. Killian, "Experimental Measurement of Self-Diffusion in a Strongly Coupled Plasma," Phys. Rev. X **6,** 021021 (2016).

[78] W.-T. Chen, C. Witte, and J. L. Roberts, "Observation of a strong-coupling effect on electron-ion collisions in ultracold plasmas," Phys. Rev. E **96,** 013203 (2017).

[79] P. Jiang and J. L. Roberts, "Electric field influences on the initial electron temperature of ultracold plasmas," Physics of Plasmas **26,** 043513 (2019).

[80] M. Aghigh *et al.*, "Dissipative dynamics of atomic and molecular Rydberg gases: Avalanche to ultracold plasma states of strong coupling," Journal of Physics B: Atomic, Molecular and Optical Physics **53,** 074003 (2020).

[81] J. Sous and E. Grant, "Possible Many-Body Localization in a Long-Lived Finite-Temperature Ultracold Quasineutral Molecular Plasma," Phys. Rev. Lett. **120,** 110601 (2018).

[82] L. G. Stanton, S. D. Bergeson, and M. S. Murillo, "Transport in non-ideal, multi-species plasmas," Physics of Plasmas **28,** 050401 (2021).

[83] A. Ng, P. Celliers, G. Xu, and A. Forsman, "Electron-ion equilibration in a strongly coupled plasma," Phys. Rev. E **52,** 4299–4310 (1995).

[84] T. K. Langin, T. Strickler, N. Maksimovic, P. McQuillen, T. Pohl, D. Vrinceanu, and T. C. Killian, "Demonstrating universal scaling for dynamics of Yukawa one-component plasmas after an interaction quench," Phys. Rev. E **93,** 023201 (2016).

[85] Y. C. Chen, C. E. Simien, S. Laha, P. Gupta, Y. N. Martinez, P. G. Mickelson, S. B. Nagel, and T. C. Killian, "Electron Screening and Kinetic-Energy Oscillations in a Strongly Coupled Plasma," Phys. Rev. Lett. **93,** 265003 (2004).

[86] M. S. Murillo, "Ultrafast Dynamics of Strongly Coupled Plasmas," Phys. Rev. Lett. **96,** 165001 (2006).

[87] M. S. Murillo, "Ultrafast dynamics of neutral, ultracold plasmas," Physics of plasmas **14,** 055702 (2007).

[88] L. G. Silvestri, L. J. Stanek, G. Dharuman, Y. Choi, and M. S. Murillo, "Sarkas: A Fast Pure-Python Molecular Dynamics Suite for Plasma Physics,", 2021.

[89] R. L. Liboff, *Kinetic theory: classical, quantum, and relativistic descriptions* (Springer Science & Business Media, 2003).

[90] H. Grad, "On the kinetic theory of rarefied gases," Communications on Pure and Applied Mathematics **2,** 331–407 (1949).

[91] J. R. Haack, C. D. Hauck, and M. S. Murillo, "A conservative, entropic multispecies BGK model," Journal of Statistical Physics **168,** 826–856 (2017).

[92] D. A. Chapman, J. Vorberger, and D. O. Gericke, "Reduced coupled-mode approach to electron-ion energy relaxation," Phys. Rev. E **88,** 013102 (2013).

[93] P. Mabey, S. Richardson, T. G. White, L. B. Fletcher, S. H. Glenzer, N. J. Hartley, J. Vorberger, D. O. Gericke, and G. Gregori, "A strong diffusive ion mode in dense ionized matter predicted by Langevin dynamics," Nature Communications 8 (2017).

[94] L. J. Stanek, R. C. Clay III, M. Dharma-wardana, M. A. Wood, K. R. Beckwith, and M. S. Murillo, "Efficacy of the radial pair potential approximation for molecular dynamics simulations of dense plasmas," Physics of Plasmas **28,** 032706 (2021).

[95] R. Gerritsma, G. Kirchmair, F. Zähringer, J. Benhelm, R. Blatt, and C. F. Roos, "Precision measurement of the branching fractions of the 4p $^2P_{3/2}$ decay of Ca II," The European Physical Journal D **50,** 13–19 (2008).

[96] L. G. Stanton and M. S. Murillo, "Unified description of linear screening in dense plasmas," Phys. Rev. E **91,** 033104 (2015).

[97] G. Dharuman, L. G. Stanton, J. N. Glosli, and M. S. Murillo, "A generalized Ewald decomposition for screened Coulomb interactions," The Journal of Chemical Physics **146,** 024112 (2017).

[98] P. Gupta, S. Laha, C. E. Simien, H. Gao, J. Castro, T. C. Killian, and T. Pohl, "Electron-Temperature Evolution in Expanding Ultracold Neutral Plasmas," Phys. Rev. Lett. **99,** 075005 (2007).

[99] J. Jin and D. A. Church, "Precision lifetimes for the Ca^+ 4p ^{2}P levels: Experiment challenges theory at the 1% level," Phys. Rev. Lett. **70,** 3213–3216 (1993).

[100] G. M. Gorman, M. K. Warrens, S. J. Bradshaw, and T. C. Killian, "Magnetic Confinement of an Ultracold Neutral Plasma," Phys. Rev. Lett. **126,** 085002 (2021).

[101] G. Tommaseo, T. Pfeil, G. Revalde, G. Werth, P. Indelicato, and J. P. Desclaux, "The g_J-factor in the ground state of Ca^+," The European Physical Journal D - Atomic, Molecular and Optical Physics **25,** 113–121 (2003).

[102] M. Chwalla *et al.*, "Absolute Frequency Measurement of the $^{40}Ca^+$ $4s\,^2S_{1/2} - 3d\,^2D_{5/2}$ Clock Transition," Phys. Rev. Lett. **102,** 023002 (2009).

[103] B. K. Sahoo and P. Kumar, "Relativistic coupled-cluster-theory analysis of unusually large correlation effects in the determination of g_j factors in Ca^+," Phys. Rev. A **96,** 012511 (2017).

[104] J. A. Bittencourt, *Fundamentals of plasma physics* (Springer Science & Business Media, 2004).

[105] R. J. LeVeque, *Finite difference methods for ordinary and partial differential equations: steady-state and time-dependent problems* (SIAM, 2007).

[106] P. Mora, "Plasma Expansion into a Vacuum," Phys. Rev. Lett. **90,** 185002 (2003).

[107] W. D. Phillips, "Nobel Lecture: Laser cooling and trapping of neutral atoms," Rev. Mod. Phys. **70,** 721–741 (1998).

[108] M. Pizzocaro, P. Thoumany, B. Rauf, F. Bregolin, G. Milani, C. Clivati, G. A. Costanzo, F. Levi, and D. Calonico, "Absolute frequency measurement of the $^1S_0 - {}^3P_0$ transition of 171Yb," Metrologia **54,** 102–112 (2017).

[109] L. Anderegg, B. L. Augenbraun, Y. Bao, S. Burchesky, L. W. Cheuk, W. Ketterle, and J. M. Doyle, "Laser cooling of optically trapped molecules," Nature Physics **14,** 890–893 (2018).

[110] R. Senaratne, S. V. Rajagopal, Z. A. Geiger, K. M. Fujiwara, V. Lebedev, and D. M. Weld, "Effusive atomic oven nozzle design using an aligned microcapillary array," Review of Scientific Instruments 86 (2015).

[111] Gerritsma, R., Kirchmair, G., Zähringer, F., Benhelm, J., Blatt, R., and Roos, C. F., "Precision measurement of the branching fractions of the 4p 2P3/2 decay of Ca II," Eur. Phys. J. D **50,** 13–19 (2008).

[112] R. W. Berends, E. H. Pinnington, B. Guo, and Q. Ji, "Beam-laser lifetime measurements for four resonance levels of Yb II," Journal of Physics B: Atomic, Molecular and Optical Physics **26,** L701–L704 (1993).